

AFFIDAVIT

I declare that I have authored this thesis independently, that I have not used other than the declared sources/resources, and that I have explicitly indicated all material which has been quoted either literally or by content from the sources used. The text document uploaded to TUGRAZonline is identical to the present master's thesis.

Date

Signature

Abstract

The availability of a precise and reliable GNSS solution is essential for navigation applications in the realm of unmanned-aerial-vehicles (UAVs) or autonomous driving. In this thesis, a GNSS application is developed, which allows for improved positioning using low-cost hardware available today and applicable in a real-time environment. A combination of pseudorange and phase measurements to GPS and Glonass satellites is used. The observations are combined in a Kalman-filter using a linear motion model. A precise point positioning (PPP) algorithm is implemented, where predicted precise satellite orbits, predicted global ionosphere model and 30-day mean differential code biases are utilized to enhance positioning performance. Finally the application is tested in pedestrian scenarios. A horizontal accuracy of ± 3 meters is achieved for 95% of the test dataset.

Zusammenfassung

Die Verfügbarkeit von genauen und zuverlässigen GNSS Lösungen ist für Navigationsanwendungen im Bereich der unbemannten Fluggeräten (UAVs) oder des autonomen Fahrens ein wichtiger Faktor. Im Zuge dieser Masterarbeit wird eine GNSS Anwendung entwickelt, welche eine verbesserte Positionierung auf heutiger Low-Cost Hardware ermöglicht und den Einsatz in Echtzeitumgebungen erlaubt. Dazu wird eine Kombination von Pseudorange- und Phasenmessungen zu GPS und Glonass Satelliten benutzt. Die Beobachtungen werden in einem Kalman-Filter kombiniert, welcher einem linearen Bewegungsmodell zugrunde liegt. Ein Precise Point Positioning (PPP) Algorithmus wurde implementiert, der auf prädizierte Satellitenorbits, prädizierte globale Ionospherenmodelle und Differential Code Biases (30-Tage Mittel) beruht und die Lösung verbessert. Abschließend wurde die Anwendung in einem Fußgängerszenario getestet. Die erreichte horizontale Genauigkeit liegt im Bereich von ± 3 Meter für 95% des Testdatensatzes.

Contents

Abstract	iii
List of Figures	vii
List of Symbols	ix
1 Introduction	1
2 Fundamentals of Precise Point Positioning	4
2.1 Introduction to Satellite-based Positioning	5
2.2 GNSS Signals and Observables	6
2.2.1 Signal Structure	7
2.2.2 Time, Code-Pseudorange and Phase-Pseudorange	10
2.2.3 Requirements for GNSS Receivers	13
2.2.3.1 Satellite Acquisition	13
2.2.3.2 Code and Phase Tracking	14
2.3 Reference Systems and Reference Frames	14
2.3.1 International Reference Systems	15
2.3.1.1 Terrestrial Reference Systems and Frames	15
2.3.1.2 International Terrestrial Reference System (ITRS)	16
2.3.2 System-Specific Reference Frames	17
2.3.2.1 World Geodetic System 1984 and GPS Time	18
2.3.2.2 PZ90 and GLONASS Time	19
2.4 Atmospheric Corrections	20
2.4.1 Ionosphere and Correction of Ionospheric Delay/Advance	21

Contents

2.4.2	Troposphere and Correction of Tropospheric Delay . . .	27
2.4.2.1	Modified Hopfield Model	29
2.4.2.2	Modeling Tropospheric Delay Using Continued Fractions	31
2.5	Additional Correction Steps	34
2.5.1	Relativistic Effects	34
2.5.1.1	Relativistic Clock Corrections	34
2.5.1.2	Relativistic Range Correction	35
2.5.2	Effects of Solid Earth Tides	35
2.5.3	Antenna Phase Center Correction	37
2.5.4	Differential Code Biases	39
3	Algorithms in Single-Frequency PPP	40
3.1	The Geometry-Free Linear Combination	40
3.2	Detection of Cycle-Slips	41
3.2.1	Test Residuals of Polynomial Fit	41
3.2.2	Deviation from Arithmetic Mean	42
3.3	Pseudorange Smoothing Using Carrier Phases	44
3.4	Least Squares Estimation and Kalman Filtering	45
3.4.1	Least Squares Estimation by Parameters	45
3.4.2	Kalman Filtering	46
4	Software Development and Implementation	50
4.1	Objectives	50
4.2	Input Data Formats and Data Sources	52
4.2.1	Extended Standard Product 3 Orbit Format (SP3) . . .	53
4.2.2	The Ionosphere Map Exchange Format (IONEX) . . .	54
4.2.3	Antenna Exchange Format Version 1.4	55
4.2.4	Differential Code Bias Data (DCB)	57
4.2.5	Glomass Constellation Status - Channel Utilization . .	59

Contents

4.3	Implementation	59
4.3.1	External Libraries	59
4.3.1.1	libcurl	60
4.3.1.2	Qwt	60
4.3.1.3	Eigen	61
4.3.2	Modular Concept	61
4.3.3	Controller Module	62
4.3.4	DataStorage Module	63
4.3.5	Navigation Processor Class	64
4.3.6	Viewer Module	66
5	Practical Measurements	71
5.1	Measurement Setup	71
5.2	Measurement Scenarios	73
5.2.1	Measurement Scenario A	76
5.2.2	Measurement Scenario B	81
6	Performance Evaluation	84
6.1	Scenario A	84
6.1.1	Scenario A-1	84
6.1.2	Scenario A-2	86
6.1.3	Scenario A-3	88
6.2	Scenario B	90
6.2.1	Scenario B-1	91
6.2.2	Scenario B-2	92
7	Outlook and Resumee	95
7.1	Summary of the Results	95
7.2	Future Developments	96
	Bibliography	99

List of Figures

1.1	Signal path errors in an urban GNSS scenario	2
2.1	Simplified geometric illustration of satellite based positioning .	6
2.2	Overview of the radio spectrum and signal energy in L1 band	7
2.3	Rotation of satellite to account for Earth's rotation during signal propagation	11
2.4	Coordinate system definition and 7-parameter transform . . .	15
2.5	Schematic figure of Earth's atmosphere's vertical layers (left) and common regions of the ionosphere (right).	21
2.6	Illustration of the single-thin-layer model of the ionosphere on the right and derivation of the surface pierce point on the left	24
2.7	Graphical illustration of the mapping function $F(z)$	26
2.9	Model of the signal path in the modified Hopfield tropospheric model	30
2.10	Defintion of antenna phase center offsets and phase center variations for satelltite (left) and receiver station (right)	37
3.1	Overview of the Kalman filtering process	48
4.1	Overview of system components	51
4.2	Controller interfaces to submodules	62
4.3	Overview of the navigation processor module	65
4.4	Viewer module overview.	67
4.5	Main Window	68
4.6	Observation data inspector	69

List of Figures

5.1	Overview of measurement equipment	72
5.2	Location overview of the measurement scenarios with respect to a local coordinate system, centered at IGS station GRAZ .	74
5.3	Detailed view of the chosen test scenarios.	75
5.4	Satellite visibility scenario A	76
5.5	Timeseries of reference coordinates (scenario A).	78
5.6	Coordinate differences to reference solution	79
5.7	Overview of different kinematic motion situations in scenario A	80
5.8	Satellite visibility scenario B	81
5.9	Timeseries of reference coordinates (scenario B).	82
5.10	Groundtrack of scenario B-1 and B-2	83
6.1	Groundtrack Comparison A1	85
6.2	Scenario A1: Coordinate difference relative to reference	86
6.3	Groundtrack Comparison A2	87
6.4	Scenario A2: Coordinate difference relative to reference	88
6.5	Groundtrack Comparison A3	89
6.6	Scenario A3: Coordinate difference relative to reference	90
6.7	Groundtrack Comparison B1	91
6.8	Scenario B1: Coordinate difference relative to reference	92
6.9	Groundtrack Comparison B2	93
6.10	Scenario B2: Coordinate difference relative to reference	94

List of Symbols

A/D	analog-digital
ANTEX	Antenna Exchange
API	application programming interface
ARP	antenna reference point
BIH	Bureau international de l'heure / International Time Bureau
BOC	Binary Offset Carrier
BOC	binary offset carrier
BPSK	binary phase-shift keying
BST	Beidou-Time
C/A	coarse-acquisition code
CBOC	Composite Binary Offset Carrier
CDMA	Code Division Multiple Access
CM	Controller-Module
CODE	Center of Orbit Determination
CoM	center of mass
cps	chips per second
CS	Central Synchronizer
CUS	channel utilization file
DCB	differential code bias
ECEF	Earth-Centered-Earth-Fixed System
ECSF	Earth-Centered-Space-Fixed System

List of Symbols

EF	earth fixed
EOF	end of file
FDMA	Frequency Division Multiple Access
FTP(S)	File Transfer Protocol (Secure)
GIM	global ionosphere models
GLONASS	Global Navigation Satellite System
GLST	GLONASS system time
GMST	Greenwich Mean Siderial Time
GNSS	Global Navigation Satellite Systems
GPL	GNU General Public License
GPS	Global Positioning System
GPST	GPS time
GRS80	World Geodetic Datum 1980
GST	Galileo System Time
GUI	graphical user interface
HMI	Human-Machine-Interface
HTTP(S)	Hypertext Transfer Protocol (Secure)
IAC	Information-Analytical Centre
IAU	International Astronomical Union
ICD	Interface Control Document
IERS	International Earth Rotation and Reference Systems Service
IGS	International GNSS Service
IONEX	Ionosphere Map Exchange
IPP	ionospheric pierce point
IRP	IERS Reference Pole
ITRF	International Terrestrial Reference Frame
ITRS	International Terrestrial Reference System
IUGG	International Union of Geodesy and Geophysics

List of Symbols

KF	Kalman Filtering
LFSR	linear-feedback-shift register
LGPL	GNU Lesser General Public License
LSQE	Least Squares Estimation
MAD	Median Absolute Deviation
MEPC	mean electromagnetic phase center
MVC	model-view-controller
NGA	National Geospatial-Intelligence Agency
NP	Navigation Processor
OCS	Operational Control Station
PCO	phase center offset
PPP	Precise Point Positioning
PRN	pseudo random noise
PZ90	Parametry Zemli 1990
QPSK	quadrature phase-shift keying
Qwt	Qt Widgets for Technical Applications
RMS	root mean square
SA	Sample Mean
SBAS	Satellite Based Augmentation System
SF	space fixed
SGS85	Soviet Geodetic System 1985
SP3	Extended Standard Product 3 Orbit Format
SPP	Single Point Positioning
SPP	sub-ionospheric pierce point
SSD	Sample Standard Deviation
STEC	slant total electron content
STT	signal travel time
TCG	Geocentric Coordinate Time

List of Symbols

TEC	total electron content
TECU	total electron content unit
TMBOC	time-multiplexed Binary Offset Carrier
TRF	Terrestrial Reference Frame
TRS	Terrestrial Reference System
UI	user interface
USNO	United States Naval Observatory
UT	universal time
UTC	Coordinated Universal Time
VTEC	vertical total electron content
WGS84	World Geodetic System 1984

1 Introduction

With the launch of *Navstar 1* on February 22, 1978¹, being the very first of a series of satellites within the *Navstar Global Positioning System* or in short GPS, the era of global navigation began. Although controlled by the US military, due to the systems design, a civilian usage was possible. An ever growing community of navigation professionals were developing methods to determine a user position accurately, for example using differential techniques to mitigate intentionally degraded satellite signals (e.g. Selective Availability).

Today the term GPS is synonymously used by end users to describe satellite-based positioning systems in general. However professionals prefer the term GNSS or *Global Navigation Satellite Systems* to point out that there are several satellite systems in orbit, which might be used by multi-system equipment to determine a user position or time.

With the growing number of satellites in space, the availability of multi-system receiver design, and the popularity of GNSS-capable smartphones and mobile devices, global satellite navigation applications have become not only accessible and affordable, but have even become essential to a modern civilization.

A typical GNSS use-case in navigation applications requires a stand-alone solution, where an application has to be able to determine its position without any communication link to other base stations.

Such systems are constrained to possible errors and signal degradation effects. Figure 1.1 depicts common errors that challenge positioning applications in

¹cf. <http://nssdc.gsfc.nasa.gov/nmc/spacecraftDisplay.do?id=1978-020A>

the stand-alone scenario in an urban environment.

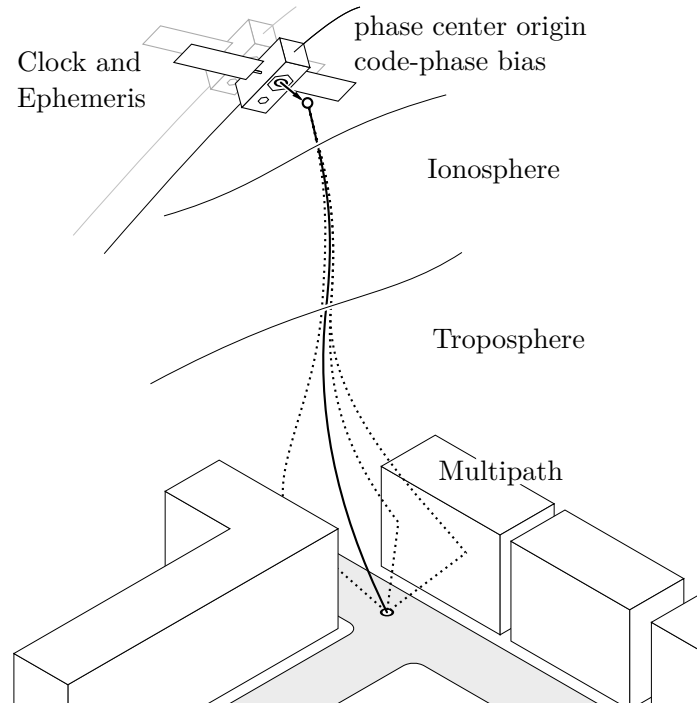


Figure 1.1: Signal path errors in an urban GNSS scenario

These errors include satellite- or segment-specific errors at signal generation, atmospheric effects, as well as multi-path effects right next to a possible receiver.

While differential positioning techniques are able to compensate for certain errors – for instance reducing atmospheric influences due to the similar signal path between station, rover and satellite, single point solutions require to make use of proper error modeling.

Precise Point Positioning or PPP is a single point positioning technique where these errors are modeled. Additionally the term PPP implies that phase measurements are utilized to further increase the positioning accuracy. This is favorably in urban environments, where multi-path effects may cause gross position errors.

The overall goal of PPP applications is to increase the accuracy of a user position on the one hand and to reduce the dependency on auxiliary measurement devices or base stations on the other hand.

While multi-frequency receiver types are standard in precise geodetic applications, single frequency receivers are predominantly available in mobile devices, such as smartphones.

Generally speaking, this thesis discusses single frequency PPP techniques and studies the usability of low-cost receiver hardware in urban environments, analyzing static and kinematic scenarios.

A cross-platform GNSS application is developed, which is capable of data acquisition, raw data preprocessing and position computation.

In chapter 2 the principles of PPP are discussed, starting with an overview of GNSS signals and observables, reference systems and different atmospheric correction models.

Chapter 3 presents algorithms used in single-frequency PPP, whereas in chapter 4 the underlying software development and implementation are shown.

The test scenarios, the hardware and measurement equipment are discussed in chapter 5, whereas an evaluation of the software package is given in chapter 6, where the processed practical measurements are presented.

Finally chapter 7 gives an outlook of further development of PPP software and discusses strategies to resolve current issues.

2 Fundamentals of Precise Point Positioning

While in relative positioning high precision is achieved by taking advantage of error cancellation due to the differential principle¹, there is no such elegant way to circumvent effects degrading the positions' accuracy in PPP, where only one receiver is available.

This chapter recapitulates fundamentals of satellite-based positioning. Starting out with a brief introduction of the principle of satellite-based positioning, it is continued by outlining a GNSS signal's structure and defining observables. Thereafter spatial and time reference systems are discussed and the need for a common reference frame is outlined. Furthermore, the focus is put on corrections models that aim to minimize atmospheric influences, impacting the positioning accuracy.

The introduction of algorithms and mathematical models to derive positioning are presented in the next chapter (3), alongside with an outline of the software architecture and computational steps needed to achieve near-realtime, high-quality, kinematic position fixes.

¹When observables share a common bias, e.g. a satellite clock error, the bias vanishes, if the observations are subtracted.

2.1 Introduction to Satellite-based Positioning

A simple definition of the principle of satellite-based positioning may be given as: the determination of the position of an arbitrary object, by measuring the time difference between the emission of the signal at the satellite and the time when the signal is received.

The object's position may be described by a 3-dimensional vector

$$\mathbf{x}(t) = (x_1(t), x_2(t), x_3(t))^T \quad (2.1)$$

where every coordinate is a function of time. Additionally let \mathbf{O} be the origin of an orthonormal 3-dimensional coordinate system, e.g. located at the Earth's center of mass (geocenter). The difference vector

$$\boldsymbol{\rho}_i(t) = \mathbf{x}(t) - \mathbf{O}(t) \text{ or simplified } \boldsymbol{\rho}_i(t) = \mathbf{x}(t) - \mathbf{O} \quad (2.2)$$

may now be denoted as the position vector of the receiving object i , indicated by a subscript letter, yielding the position relative to the reference system's origin.

Consider another object, denoted as sender or satellite with index j , indicated by a superscript letter and form the difference

$$\boldsymbol{\rho}^j(t) - \boldsymbol{\rho}_i(t) = \boldsymbol{\rho}_i^j(t) = \|\boldsymbol{\rho}_i^j(t)\|_2 \mathbf{e}_i^j = \rho_i^j(t) \mathbf{e}_i^j \quad (2.3)$$

where $\|\cdot\|_2$ is the canonical ℓ^2 -Norm² and therefore a representation for the geometric range of the difference vector, while \mathbf{e}_i^j represents the unit vector pointing from the receiver i to the satellite j . Figure 2.1 visualizes the geometrical concept.

If the satellite position $\boldsymbol{\rho}^j(t)$ was known and the geometric distance was measured, there would be three remaining unknowns left in equation 2.3. But the actual range measurement between satellite and receiver relies on measuring the time difference of the emitted and the received signal, the one-way signal

² $\|\Delta\mathbf{x}\|_2 = \sqrt{\Delta x_1^2 + \Delta x_2^2 + \Delta x_3^2}$

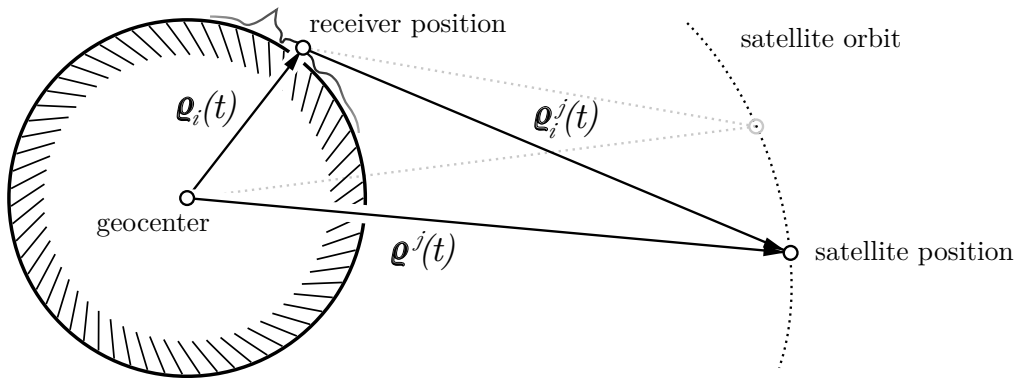


Figure 2.1: Simplified geometric illustration of satellite based positioning

travel time. For a time difference measurement, the time frames of receiver and satellites have to share the same time reference. Perfect synchronization of receiver and satellite clocks are unfeasible, as a consequence, a further unknown parameter, connecting the receiver and satellite time, has to be introduced, the receiver clock error.

2.2 GNSS Signals and Observables

Global Navigation Satellite Systems aim at providing an accurate positioning (and timing) service for users on a global scale. For that purpose radio signals with special characteristics are generated at the satellite and emitted via the satellite's antenna at frequencies in the radio navigation frequency band.

The GNSS composite radio signal of each satellite is a combination of

- a carrier wave or carrier of frequency f_i ,
- a ranging code or pseudorandom noise code and at least in some cases
- a data stream or navigation message, providing additional information.

A certain knowledge of the signal structure is essential for the assessment of GNSS measurements. The following sections recapitulate basic signal fundamentals and introduce GNSS observables.

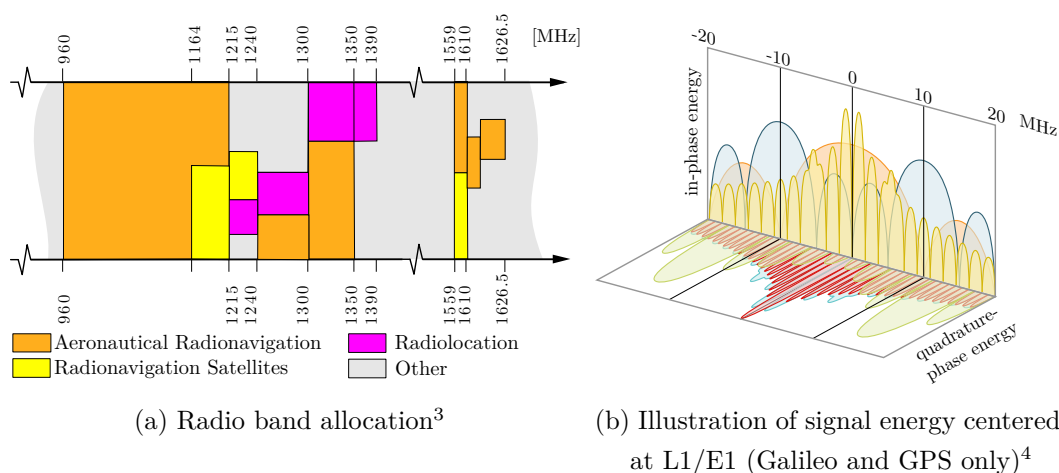


Figure 2.2: Overview of the radio spectrum and signal energy in L1 band

2.2.1 Signal Structure

Today’s GNSS are situated in the lower L2 and L5 as well as in the upper L1 bands of the radio spectrum, which are reserved to radio navigation satellite systems (for example see Galileo OS SIS ICD, 2010). Figure 2.2a shows an extract of the radio spectrum’s allocation and 2.2b gives an overview of the signal power solely based on GPS and Galileo satellites.

Different ranging codes and auxiliary data are modulated onto the maiden carrier wave. Consider ranging code and data as a binary sequence of zeros and ones. Each element of the sequence is referred to as chip. Ranging codes may be given as memory codes (e.g. Galileo’s E1B/E1C, cf. Galileo OS SIS ICD, 2010, annex C), meaning the complete sequence is given as it is, in terms of a linear-feedback-shift register (LFSR) with predefined start values (e.g. GPS’ C/A-code Gold sequences, cf. GPS-ICD-200H, 2013, section 3.2.1.3), or as a generator polynomial with initial values, yielding again a LFSR, which is the case for the GLONASS C/A code sequence (cf. GLONASS ICD, 2008,

³based on http://www.ntia.doc.gov/files/ntia/publications/spectrum_wall_chart_aug2011.pdf, (U.S. radio allocation chart 2011, U.S. Department of Commerce)

⁴based on http://navipedia.net/index.php/File:Galileo_Signal_Plan_Fig_3.png (by Carlos Lopez)

Table 2.1: GNSS Signals - frequency bands

GPS ⁸	GLONASS ⁹	GALILEO ¹⁰
Carrier Frequencies [MHz]		
L1 1575.420	G1 ⁰ 1602.000	E1 1575.420
L2 1227.600	G1 ⁱ =G1 ⁰ +K _i ·0.5625	E6 1278.750
L5 1176.450	G2 ⁰ 1246.000	E5 1191.795
	G2 ⁱ =G2 ⁰ +K _i ·0.4375	E5a 1176.450
	K _i =(-7,-6,...,5,6)	E6b 1207.140

section 3.3.2.1). By introduction of a chipping rate⁵ denoted by f_c for the code and f_d for the data respectively, both code and data message may now be considered as a function of time. In other words, the chipping rate assigns a certain time interval to each chip.

Code and data functions are used to modulate the phase of the carrier wave, in the sense of changing the phase by π , reflecting the binary state change. This type of modulation is called *binary phase-shift keying* (BPSK). To achieve even more information modulated on the same carrier, *quadrature phase-shift keying* (QPSK) is implemented (cf. Galileo OS SIS ICD, 2010, section 2.3.1.2), where the signal splits into an in-phase and a quadrature-phase component, each with own code and data messages. With growing number of satellite systems, the density within the dedicated radio bands grew and the more sophisticated modulation technique *binary offset carrier* (BOC) was developed (cf. Galileo OS SIS ICD, 2010, section 2.3.3). The use of an additional rectangular sub-carrier minimizes the signal's power at the center frequency of the carrier, where the main lobe of BPSK modulated signals is situated, shifting the signal

⁵defined as chips per second [cps]

⁸taken from GPS-ICD-200H, 2013

⁹the L1/L2 frequency bands specified in GLONASS ICD, 2008 , are here denoted as G1/G2 respectively

¹⁰see Galileo OS SIS ICD, 2010

energy in the side-bands, symmetrical to the center frequency.

A list of carrier frequencies is given in table 2.1. Code lengths, chipping rates and modulations for civilian signals in the L1 band are listed in table 2.2.

Access Strategies

On the user's side, a receiver has to be able to distinguish every satellite to access the information modulated onto the respective carrier. Two access methods are implemented in current satellite systems, namely:

- **Code Division Multiple Access (CDMA):**
For each satellite a unique pseudo random code sequence, which might also be referred to as pseudo random noise code (PRN) is defined. These sequences are selected to be orthogonal and therefore meet cross-correlation demands of the receiver, yielding maximum correlation for identical PRNs at zero lag and minimum cross-correlation for signals modulated by dissimilar pseudo sequences (cf. Hofmann-Wellenhof, 2008, p. 77). Hence, satellites may emit at the same carrier frequencies simultaneously. GNSS receivers exploit the correlation properties of the PRN code and are therefore able to distinguish different satellites. GPS, Beidou/Compass and Galileo are examples for CDMA systems.
- **Frequency Division Multiple Access (FDMA):**
Satellites are distinguished by the use of slightly shifted carrier frequencies (channels) instead of an identifying code pattern. The GLONASS system makes use of this approach, assigning unique frequencies to satellites, although antipodal satellites within the same orbital plane may transmit on equal frequencies (cf. GLONASS ICD, 2008). The current channel assignment table is transmitted by the satellites within the non-immediate information part of the navigation message (cf. GLONASS ICD, 2008, paragraph 4.5), or available on-line at the federal space agency's

Table 2.2: GNSS Signals - Civil Ranging Codes in the L1/G1/E1 frequency bands, defined in the respective signals in space or interface control documents.

Frequency band	Code	Code Length [chips]	Ranging Code Chip-Rate [Mcps]	Modulation
L1	C/A	1 023	1.023	BPSK(1)
	P(Y)	~ 7 days ^(a)	10.230	BPSK(10)
	L1C _D	10 230	1.023	BOC(1,1)
	L1C _P	10 230	1.023	TMBOC(6,1) ^(b)
G1	C/A	511	0.511	BPSK(0.511)
E1	E1b	4 092	1.023	CBOC(6,1,1/11) ^(c)
	E1c	4 092	1.023	CBOC(6,1,1/11) ^(c)

^(a) according to Hofmann-Wellenhof, 2008, p. 331

^(b) TMBOC refers to a time-multiplexed BOC (BOC(1,1) and BOC(6,1))

^(c) CBOC refers to a composite BOC (BOC(1,1) and BOC(6,1))

Information-Analytical Centre (IAC). The GLONASS-K generation satellites will provide CDMA signals in addition (e.g. presented by Revnivkykh, 2012).

2.2.2 Time, Code-Pseudorange and Phase-Pseudorange

Let T^{Ref} be a time-point on a reference time scale, meaning a strictly continuous, error-free time base. The emitted satellite signal propagates through space until it reaches a receiver. Figure 2.3 gives an illustration of the relation between signal propagation and time.

The time of emission in the satellites own time frame T_E is given by the relation

$$T_E = T_E^{\text{Ref}} + \delta t^{\text{Sat}} \quad (2.4)$$

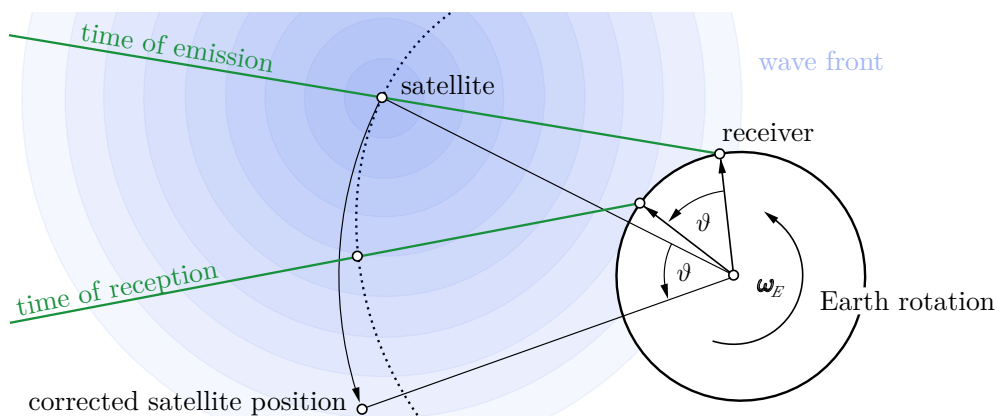


Figure 2.3: Rotation of satellite to account for Earth's rotation during signal propagation

where T_E^{Ref} is the emission time in the reference time base and δt^{Sat} is the current error or offset of the satellite's clock. When the signal is received at the receiver side, the reception time T_R in the receiver's time frame can be described as

$$T_R = T_R^{\text{Ref}} + \delta t_{\text{Rec}} = T_E^{\text{Ref}} + T_{\text{STT}} + \delta t_{\text{Rec}} \quad (2.5)$$

where T_R^{Ref} stands for the instant moment of reception in the reference time base, δt_{Rec} accounts for the receiver clock error, and T_{STT} represents the time the signal takes to propagate through space from the satellite to the receiver – known as *signal travel time*.

The receiver measures the time difference ΔT_R^E , which is given by

$$\begin{aligned} \Delta T_R^E &= T_R - T_E = \cancel{T_E^{\text{Ref}}} + T_{\text{STT}} + \delta t_{\text{Rec}} - \left(\cancel{T_E^{\text{Ref}}} + \delta t^{\text{Sat}} \right) \\ &= T_{\text{STT}} + \delta t_{\text{Rec}} - \delta t_{\text{Sat}} = T_{\text{STT}} + \Delta \delta_{\text{Rec}}^{\text{Sat}}, \end{aligned} \quad (2.6)$$

with $\Delta \delta_{\text{Rec}}^{\text{Sat}}$ being a combined satellite and receiver clock error.

The *signal travel time* is solely based on the reference time base. It is related to the geometric range $\varrho_{\text{Rec}}^{\text{Sat}}$ and may therefore be expressed using the speed of light

$$\varrho_{\text{Rec}}^{\text{Sat}} = c T_{\text{STT}} + \Delta_{\text{error}} \quad c \dots \text{speed of light} \quad (2.7)$$

where the term Δ_{error} includes the relative movement of the receiver while the signal travels through space and accounts for additional biases induced during propagation⁶. On the other hand, the measured time difference $\Delta T_{\text{R}}^{\text{E}}$, using the same relation, returns a so-called *pseudorange*

$$R_{\text{Rec}}^{\text{Sat}} = c \Delta T_{\text{R}}^{\text{E}} + \Delta_{\text{code}} \quad (2.8)$$

where Δ_{code} describes code specific propagation errors. Substituting equation 2.7 and 2.8 in equation 2.6, transforming it into an equation of ranges, yields the (code)-pseudorange observation equation

$$R_{\text{Rec}}^{\text{Sat}}(t) = \varrho_{\text{Rec}}^{\text{Sat}}(t) + c \Delta \delta_{\text{Rec}}^{\text{Sat}}(t) + \Delta_{\text{code}}(t) + \varepsilon_{\text{code}} \quad (2.9)$$

as a function of the corrected reception time (reference time scale) and $\varepsilon_{\text{code}}$ is added as a code random noise variable.

Aside from pseudoranges, GNSS receivers may provide another GNSS measurement denoted as phase observable. Consider the carrier signal generated at the satellite to be $\varphi^{\text{Sat}}(t)$ and a replicated carrier at the receiver with phase $\varphi_{\text{Rec}}(t)$. When the emitted signal is received at the receiver, the signal phase is compared to the replicated carrier. The receiver output is a time series of the measured phase difference of the two signals. Finally, consider the carrier wave is interpreted as a range, counting the integer number of full wavelengths between satellite and receiver, denoted as ambiguity N , scaling it with the carrier wavelength λ and multiplying the observed fractional phase difference again with a scale factor. The phase-pseudorange then yields

$$\lambda \Phi_{\text{Rec}}^{\text{Sat}}(t) = \varrho_{\text{Rec}}^{\text{Sat}}(t) + \lambda N + c \Delta \delta_{\text{Rec}}^{\text{Sat}}(t) + \Delta_{\text{phase}}(t) + \varepsilon_{\text{phase}} \quad (2.10)$$

where λ identifies the carrier wavelength, and $\Phi_{\text{Rec}}^{\text{Sat}}$ is referred to as fractional part of the phase difference, and may be derived in a manner, similar to the code-pseudorange equation 2.9.

⁶consider for instance the change of the speed of light in media.

2.2.3 Requirements for GNSS Receivers

Previous sections introduced signal structure and common GNSS observables. This section provides a brief insight in receiver signal processing to understand which problems might occur during regular measurements at the receiver side.

Envision a receiver able to capture signals in the radio frequency spectrum. Only the previously mentioned sections of the radio spectrum are relevant, hence in a first stage, the receiver may apply a band-pass filter to select the GNSS specific frequency bands. In a subsequent process, further signal refinement, which might comprise additional filtering and down-conversion of the signal, is carried out before feeding the signal into an analog-digital (A/D) conversion.

2.2.3.1 Satellite Acquisition

At the acquisition stage, the receiver has to determine if satellite signals are present in the frequency band. Therefore, code replicas have to be generated for every satellite and correlated with the input signal, shifting it in time and frequency domain respectively. If a satellite is present and the signal to noise ratio is above the receiver's sensitivity, the receiver is able to resolve the time offset as well as the Doppler-induced frequency shift, by searching for the cross-correlation maximum.

The search space is reduced, taking advantage of satellite almanac data and an approximation of the receiver position, where the Doppler-frequency shift and time estimates are predicted beforehand. This is often referred to as a receiver warm-start. In contrast to this a cold-start implies having no knowledge of orbits or receiver position in advance.

The satellite acquisition is lost obviously, if the satellite signal drops below the noise level.

2.2.3.2 Code and Phase Tracking

When satellites have been identified, the receiver's task is to keep track of the code-shift and the carrier phase difference. This is needed to derive pseudoranges and phase observations as well as to decode the information on the data stream, i.e. the navigation bits of the navigation message.

It might occur that the receiver loses the lock of a specific satellite, either due to a weak satellite signal, a total loss of the satellite's visibility or a receiver specific failure. In such a situation, a re-acquisition process is initiated and the integer number relation between consecutive phase observations is lost. This is referred to as cycle slip and has to be detected in applications where phase-pseudoranges are used and therefore ambiguities need to be estimated.

2.3 Reference Systems and Reference Frames

For the purpose of satellite based positioning it is inevitable to define a common global reference system. It is apparent that such a system has to consist of a definition of its origin and its orientation in 3-dimensional space. Moreover, beside the definition of physical constants, especially where timing is essential to the application, a time reference system has to be selected.

In addition, a spatial reference system may be classified as

- Earth-Centered-Space-Fixed Systems (ECSF), describing a reference system originating at Earth's center with an orientation fixed in space
- Earth-Centered-Earth-Fixed Systems (ECEF), which are not only Earth-centered but additionally co-rotate with Earth.

The relation between ECSF and ECEF is fixed by the introduction of a time dependent angle between the two systems. If the Greenwich meridian, co-rotating with Earth, defines the reference for the ECEF system, this angle is referred to

as *Greenwich Hour Angle*. Figure 2.4 shows the relation of a space fixed (SF) and an earth fixed (EF) reference system located at the geocenter.

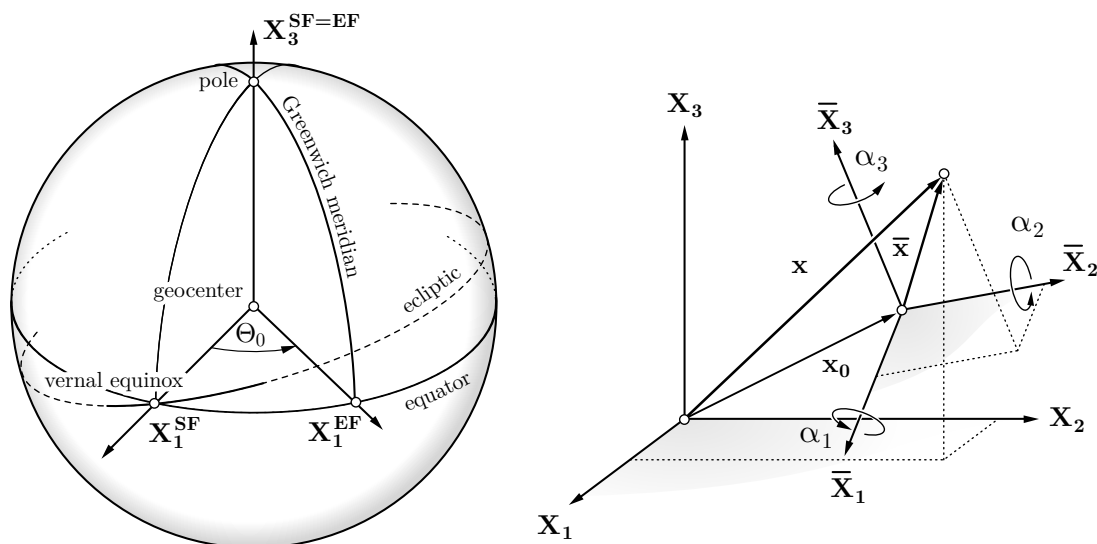


Figure 2.4: Coordinate system definition and 7-parameter transform

2.3.1 International Reference Systems

In 1987, the *International Union of Geodesy and Geophysics* (IUGG) and the *International Astronomical Union* (IAU), formed an international organization, to provide definitions and realizations of celestial and terrestrial reference systems and frames, as well as transformation parameters between current and former reference frames to support the scientific community – the *International Earth Rotation and Reference Systems Service* (IERS), according to Mueller, 2000.

2.3.1.1 Terrestrial Reference Systems and Frames

Consider a trihedron, originating at a certain point $\mathbf{O} = (o_1, o_2, o_3)^T$ and represented by a 3-dimensional basis \mathbf{E} , consisting of 3 orthogonal vectors of the

same scale λ : $(\boldsymbol{\varepsilon}_1, \boldsymbol{\varepsilon}_2, \boldsymbol{\varepsilon}_3) = \lambda(\mathbf{e}_1, \mathbf{e}_2, \mathbf{e}_3)$, that forms an Euclidean affine space. Let this system be attached to the Earth's center⁷ and co-rotating with the Earth's rotation. Such a system is then referred to as *Terrestrial Reference System* (TRS).

A *Terrestrial Reference Frame* (TRF) is the physical materialization of a TRS, meaning that origin, orientation, scale, and the change in time of these parameters are fixed (e.g. by the introduction of physical points, for which the coordinates are determined).

2.3.1.2 International Terrestrial Reference System (ITRS)

The IERS defined the *International Terrestrial Reference System* (ITRS) to be a TRS in accordance with the following conditions (cf. Petit et al., 2010):

- **Origin:** Its origin is Earth's center of mass (geocenter), including oceans and the atmosphere.
- **Orientation:** Its orientation is given by the BIH⁸ orientation at 1984.0
- **Scale:** The scale is consistent with the *Geocentric Coordinate Time* (TCG) for a geocentric local frame.
- **Time Evolution:** Using the condition of a no-net-rotation⁹ with regards to horizontal tectonic motions over the whole Earth.

The *International Terrestrial Reference Frame* (ITRF) is the realization of the ITRS, in its origin, orientation and scale by means of a selection of physical points on Earth. It is subject to changes, and therefore has to be monitored using the IERS base station network.

⁷where Earth's center might be defined geometrically, e.g. center of the Earth's figure, or by the center of mass.

⁸Bureau international de l'heure / International Time Bureau.

⁹Defined according to Gordon, 1991 as: "The no-net-rotation frame is defined as the reference frame that yields zero for the integral of $\mathbf{v} \times \mathbf{r}$ over Earth's surface, where \mathbf{v} is the plate velocity at position \mathbf{r} "

The transition between two TRF is achieved by a 7 parameter transformation (cf. figure 2.4):

$$\mathbf{X} = \mathbf{X}_0 + \mu \mathbf{R} \bar{\mathbf{X}} \quad (2.11)$$

with 3 translation parameters (\mathbf{X}_0), 3 rotation parameters (contained in the rotation matrix \mathbf{R}) and a scale factor μ . Due to the fact that two realizations of TRS are very close in terms of the defining parameters, IERS formulates the transformation in linearized form

$$\mathbf{X} = \mathbf{X}_0 + \bar{\mathbf{X}} + \delta\lambda \bar{\mathbf{X}} + \delta\mathbf{R} \bar{\mathbf{X}} \quad (2.12)$$

with

$$\mu = 1 + \delta\lambda \quad \mathbf{R} = (\mathbf{I} + \delta\mathbf{R}) = \begin{bmatrix} 1 & -R_3 & R_2 \\ R_3 & 1 & -R_1 \\ -R_2 & R_1 & 1 \end{bmatrix} \quad (2.13)$$

The transformation parameters ($X_0^1, X_0^2, X_0^3, \delta\lambda, R_1, R_2, R_3$) between two reference frames are provided by the IERS.

2.3.2 System-Specific Reference Frames

GNSS users have been in the challenging situation that every satellite navigation system deployed its own reference framework, considering the choice of the coordinate reference system and the time scales definition. It has to be pointed out that the term reference system refers solely to the theoretical definition of a system, whereas reference frames are the physical representation of such a system in reality. In some cases the discrimination between the system and the frame is not striking.

Table 2.3: Comparison of reference ellipsoids of the GPS and GLONASS system.

WGS84 ¹⁰	PZ90.02 ¹¹
$a = 6\,378\,137\text{ m}$	$a = 6\,378\,136\text{ m}$
$f = 1/298.257223563$	$f = 1/298.25784$
$GM = 3\,986\,005 \cdot 10^8\text{ m}^3\text{s}^{-2}$	$GM = 3\,986\,004.418 \cdot 10^8\text{ m}^3\text{s}^{-2}$
$\omega = 7.292115 \cdot 10^{-5}\text{ rad/s}$	$\omega = 7.292115 \cdot 10^{-5}\text{ rad/s}$

2.3.2.1 World Geodetic System 1984 and GPS Time

The reference system of GPS is known as the *World Geodetic System 1984* (WGS84). According to Decker, 1986, the defining parameters, the reference frame orientation and its ellipsoidal gravity formula were defined in concordance with the *Geodetic Reference System 1980* (GRS80) at the time of its definition. Following the *National Geospatial-Intelligence Agency's Standardization Document* (cf. NGA, 2014), the WGS84 system is a right-handed coordinate system and orthogonal basis with its

- **origin**, being located at Earth's center of mass (geocenter), the
- **X_3 -axis**, pointing to the IERS Reference Pole (IRP), the
- **X_1 -axis**, being the intersection of the IERS Reference Meridian and normal plane on X_3 fixed to the geocenter, and finally the
- **X_2 -axis** completing the right-handed trihedron.

Along with this definition, a reference ellipsoid of revolution is introduced, with its geometrical center coinciding with the system's origin and its axis of rotational symmetry being identical to the X_3 -axis. The parameters of the ellipsoid are displayed in table 2.3.

In the case of GPS both the reference system and its realization (reference frame) are usually denoted by WGS84, although, strictly speaking, the realization can be distinguished by an accompanying declaration of the GPS-

¹⁰Definition of World Geodetic System 1984 see Decker, 1986

¹¹PZ90.02 according to GLONASS ICD, 2008

week¹², e.g. WGS84 (G1762). New realizations are generated by the *National Geospatial-Intelligence Agency* (NGA) if necessary (cf. NGA, 2014, p. 85).

The GPS Interface Control Document (cf. GPS-ICD-200H, 2013) states that the GPS time (GPST) is defined as continuous time scale, originating at midnight (12 pm) of January 5th, 1980 UTC(USNO)¹³. It is given in units of seconds and weeks¹⁴ and the *Operational Control Station* (OCS) "shall control it to be within one microsecond of UTC (modulo one second)" (cf. GPS-ICD-200H, 2013).

2.3.2.2 PZ90 and GLONASS Time

Originally the GLONASS coordinate reference system was based on *Soviet Geodetic System 1985* (SGS85), but in the mid 1990s the Parametry Zemli 1990 (PZ90)¹⁵ was adopted. The GLONASS Interface Control Document (ICD) (cf. GLONASS ICD, 2008) specifies its definition as follows:

- The **origin** is located at the center of the Earth's body, the
- **X_3 -axis** is directed to the Conventional Terrestrial Pole as recommended by the IERS, the
- **X_1 -axis** is directed to the point of intersection of the Earth's equatorial plane and the zero meridian established by BIH and finally the
- **X_2 -axis** completes the right-handed coordinate system.

The document additionally gives the parameters of the PZ90.02 ellipsoid itself. They are listed in table 2.3.

While GPST is designed to be continuous, and therefore differs from current Coordinated Universal Time UTC(USNO) by an integer number of leap seconds, GLONASS system time (GLST) is generated on basis of the GLONASS

¹²The GPS time is usually given in weeks and seconds of the week.

¹³UTC(USNO) reads UTC as maintained by the U.S. Naval Observatory

¹⁴1 week = 604,800 seconds

¹⁵Параметры Земли 1990 года (ПЗ-90) transliterates to "Parameters of the Earth 1990 (year)"

Central Synchronizer (CS) continuous time scale as well, but due to the permanent synchronization to the national UTC reference UTC(SU)¹⁶, the system accounts for leap seconds. In addition there is a constant 3 hours offset between GLST and UTC(SU)

$$\text{GLST} = \text{UTC(SU)} + 3 \text{ h} \quad (2.14)$$

that has to be considered.

Likewise other GNSS systems incorporate their own reference frameworks, with Beidou relying on Beidou-Time (BST) and the *Chinese Geodetic Coordinate System 2000* (cf. Han et al., 2011), as well as Galileo with Galileo System Time (GST) and the Galileo Terrestrial Reference Frame (cf Galileo OS SIS ICD, 2010).

2.4 Atmospheric Corrections

On the way from the GNSS satellite to the receiver, the signal propagates through the atmosphere of Earth. A common atmospheric stratification of the atmosphere yields five principle layers, namely *troposphere*, *stratosphere*, *mesosphere*, *thermosphere* and *exosphere*, characterized by different physical properties with respect to particle composition, density, temperature and ionization. Figure 2.5 illustrates the different atmospheric layers. For GNSS users the wave propagation properties are of particular importance, hence the atmosphere is typically divided into two layers, namely an electrically neutral *troposphere* and an ionized layer denoted as *ionosphere*.

¹⁶UTC(SU) reads UTC as maintained by the state time reference of Russia, formerly part of the Soviet Union therefore the abbreviation SU.

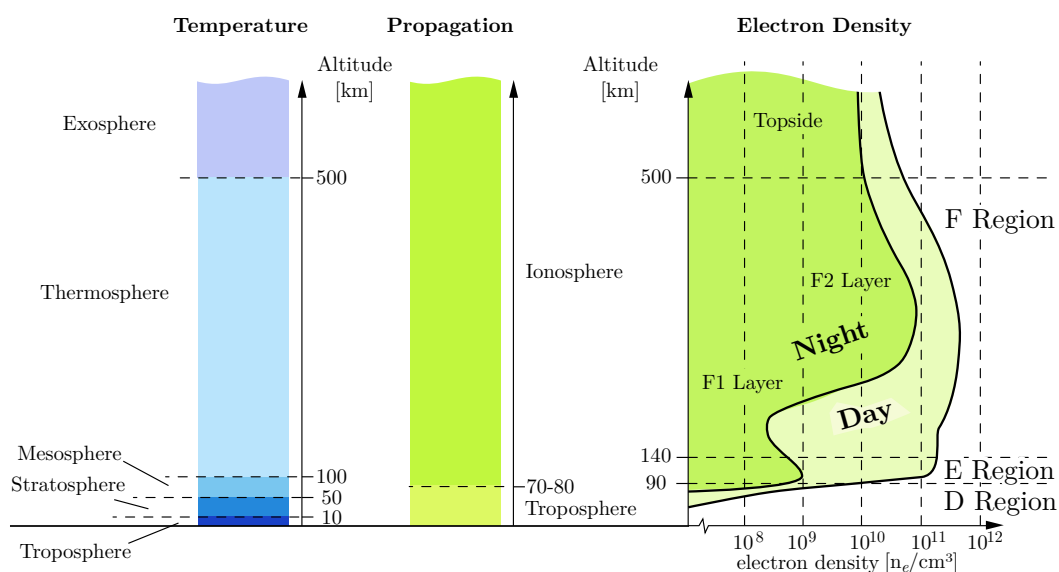


Figure 2.5: Stratification approaches of the Earth's atmosphere (left) and electron density in the ionosphere during day and night (right), based on Figure 2.4 in Elzei, 2013, p. 16

2.4.1 Ionosphere and Correction of Ionospheric Delay and Advance

The ionosphere is Earth's atmospheric layer where the number of ionized particles and free electrons per volume is larger than in other atmospheric layers¹⁷. The reason for this ionization is primarily due to solar radiation, secondary ionization processes, as well as cosmic rays (cf. Dominici, 1998). The ionosphere is a dispersive medium in the spectrum of GNSS radio signals (cf. Seeber, 2003), changing signal properties depending on the signal frequency, as a result of a wavelength dependent refractive index $n = n(\lambda)$.

Given an electromagnetic wave of frequency f and wavelength λ , the phase

¹⁷Although the overlying magnetosphere consists of charged particles only, the overall particle density decreases exponentially with altitude, whereas lower atmospheric layers are dominated by neutral particles and therefore considered as uncharged

velocity, being the velocity of in-phase wave patterns, is defined as

$$v_{\text{ph}} = \lambda f \quad (2.15)$$

According to Demtröder, 2013, p. 356, the group velocity, which is defined as the velocity of maximum amplitude of a wave packet, may be expressed as

$$v_{\text{gr}} = v_{\text{ph}} - \lambda \frac{dv_{\text{ph}}}{d\lambda} \quad (2.16)$$

using the relation $v = c/n$ as well as $c = \lambda f$ and applying approximations discussed in Hofmann-Wellenhof, 2008, p. 117, results in

$$n_{\text{gr}} = n_{\text{ph}} + f \frac{dn_{\text{ph}}}{df}. \quad (2.17)$$

This gives a relation for the refractive indices of both the wave group and the carrier phase in dependence of the frequency of the electromagnetic wave. According to Seeber, 2003, p. 54, the phase refractive index can be expressed in a power series

$$n_{\text{ph}} = 1 + \frac{c_2}{f^2} + \frac{c_3}{f^3} + \dots \quad (2.18)$$

and neglecting terms of order $1/f^3$ and higher yields

$$n_{\text{ph}} \approx 1 + \frac{c_2}{f^2} \quad (2.19)$$

The refractive index of the wave packet may then be expressed as

$$n_{\text{gr}} = 1 - \frac{c_2}{f^2} \quad (2.20)$$

Utilizing *Fermat's Principle*, which states that light travels along the shortest optical path, the optical path length s is given as

$$s(n) = \int n \, ds \quad , \quad (2.21)$$

where the refractive index n , dependent on the signal wavelength and electron density, is integrated along the true path of the signal. For GNSS applications it is desirable to separate the optical path into two parts, s_0 matching the fictive

straight path at a constant refractive index $n_0 = 1$ (equal to the geometric range) and a correction term Δ^{iono} so that equation 2.21 translates to

$$s = \int 1 \, ds_0 + \Delta^{\text{iono}} = s_0 + \Delta^{\text{iono}} \quad \text{with} \quad \Delta^{\text{iono}} = \int n \, ds - s_0 \quad (2.22)$$

If this equation is applied for the wave packet and the wave phase, substituting the relation found in equations 2.19 and 2.20 respectively, the ionospheric correction yields

$$\Delta_{\text{ph}}^{\text{iono}} = \int n_{\text{ph}} \, ds - s_0 \approx \int \left(1 + \frac{c_2}{f^2}\right) \, ds_0 - \int 1 \, ds_0 = -\frac{40.3}{f^2} \int N_{\text{E}} \, ds_0 \quad (2.23)$$

and

$$\Delta_{\text{gr}}^{\text{iono}} = \int n_{\text{gr}} \, ds - s_0 \approx \int \left(1 - \frac{c_2}{f^2}\right) \, ds_0 - \int 1 \, ds_0 = \frac{40.3}{f^2} \int N_{\text{E}} \, ds_0 \quad (2.24)$$

where N_{E} , the electron density per square meter, is a function dependent on the number of electrons along the path. In addition, the integration is performed along the geometric path instead of the true optical path, which is a valid approximation according to Hofmann-Wellenhof, 2008, p. 119.

While the factor $40.3/f^2$ is constant for a constant frequency f , the electron density N_{E} varies over time.

The influence of the ionospheric refraction has to be estimated or modeled. It might even be minimized in a so-called ionosphere-free linear combination of homogeneous observables, provided that GNSS signals on at least two carrier frequencies are available. Even code- and phase-observations on the same carrier-frequency might be used to compensate for the ionospheric effect, due to the opposite sign in equations 2.23 and 2.24, with the drawback of a raised noise level.

For the purpose of estimation and modeling the *total electron content* (TEC) representing the integral

$$\text{TEC} = \int N_{\text{E}} \, ds_0 \quad (2.25)$$

is introduced and a *total electron content unit* (TECU)

$$1 \text{ TECU} = 10^{16} \text{ electrons} / \text{m}^2 \quad (2.26)$$

is defined. Hereafter the ionospheric correction term can be denoted

$$\Delta_{\text{ph}}^{\text{iono}} = -\frac{40.3}{f^2} \text{ TEC} \quad \text{and} \quad \Delta_{\text{gr}}^{\text{iono}} = \frac{40.3}{f^2} \text{ TEC} \quad (2.27)$$

Because the definition of the TEC implies a summation along a straight line (e.g. the geometric range from satellite to receiver) which itself is dependent on the observed satellite and the receiver's position to achieve global comparability among TEC values, the TEC is usually given in zenith direction. Those TEC values are commonly referred to as *vertical total electron content* (VTEC) and are the output of global ionosphere models (GIM).

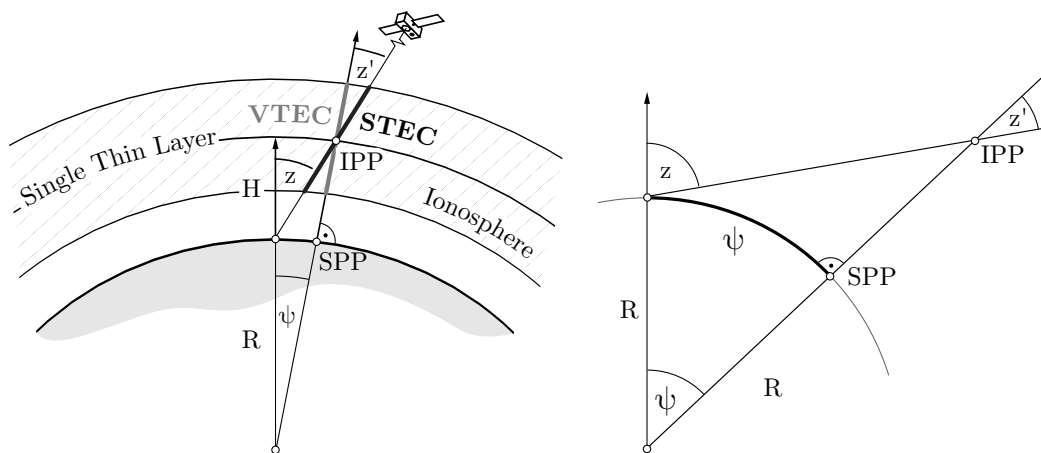


Figure 2.6: Illustration of the single-thin-layer model of the ionosphere on the right and derivation of the surface pierce point on the left

While the correct derivation of VTEC values is essential to global ionosphere models, for an observer receiving satellite signals there is a need to retrieve a line-of-sight specific TEC or *slant total electron content* (STEC) to account for the ionospheric refraction from a GNSS user's perspective with an arbitrary elevation angle. One method is using a so-called *single-thin-layer* approach, where the free electrons are assumed to be concentrated in an infinitesimally

thin layer. The VTEC values of a GIM are projected onto a spheroid surface of constant radius $R+H$ originating at the geocenter, with R being a mean earth radius and H the altitude of the thin layer above ground. Figure 2.6 depicts

Table 2.4: Impact of the ionospheric refraction on range measurements for different values of TEC (left) and change of the values for the mapping function subject to a change in the zenith angle (right)

TEC	Range Delay		z	z'	$F(z)$
$\Delta_{\text{gr}}^{\text{iono}} [\text{m}] = c_0 \cdot \Delta_{\text{gr}}^{\text{iono}} [\text{s}]$	R=6371 km and H=450 km				
[TECU]	[m]	[ns]	[deg]	[deg]	[]
10	1.6	5.4	0	0	1.00
25	4.1	13.5	10	9.3	1.01
50	8.1	27.1	20	18.6	1.06
75	12.2	40.6	50	45.7	1.43
100	16.2	54.1	80	66.9	2.55
200	32.4	108.3	90	69.1	2.80

the situation of an earth-bound receiver observing a satellite. The straight line pierces the ionospheric layer at the IPP - the ionospheric pierce point. At that point, the given vertical electron content has to be translated to the slant total electron content. This is accomplished by the introduction of a mapping function

$$F(z) = \frac{\text{STEC}}{\text{VTEC}} \Rightarrow \text{STEC} = F(z) \cdot \text{VTEC}, \quad (2.28)$$

which depends on the zenith angle z at the observation site. As shown in figure 2.6, in a first step the STEC at the IPP may be derived as

$$\text{STEC}_{\text{IPP}} = \frac{1}{\cos(z')} \text{VTEC}_{\text{IPP}}. \quad (2.29)$$

A transition from $z' \rightarrow z$ is accomplished following the *law of sines*

$$\frac{\sin(z')}{R} = \frac{\sin(z)}{R+H} \quad (2.30)$$

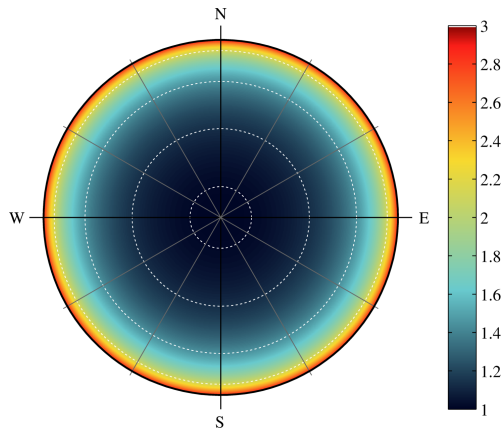


Figure 2.7: Graphical illustration of the mapping function $F(z)$.

which finally results in the relation

$$\sin(z') = \frac{R}{R+H} \sin(z) \quad (2.31)$$

Table 2.4 lists the ionospheric delay (Δ^{iono}) in terms of time and range correction as well as the mapping function values as a function of the zenith angle z .

Global ionospheric models or maps are usually given in the form of a global grid, at a specified height, modeled at various times. To extract the matching VTEC value for a specific satellite, the geographic coordinates of the ionospheric pierce point (λ_{IPP} , φ_{IPP}) have to be computed. Let the *sub-ionospheric pierce point* SPP be the projection of the IPP on earth's surface.¹⁸

The spherical distance on a unit sphere between the observation point denoted as (λ_0, φ_0) and the SPP is given as

$$\psi_{0\text{-SPP}} = z - \arcsin\left(\sin(z) \frac{R}{R+H}\right) \quad (\text{in radians}). \quad (2.32)$$

¹⁸The IONEX standard defines the latitude to be geocentric, not geodetic/geographical. If a single layer model is present, a spherical layer is assumed at a certain height, allowing for computations to take place on a sphere, not an ellipsoid. Therefore φ_{IPP} represents the geocentric latitude on the model sphere.

Utilizing the spherical *law of cosines* yields¹⁹

$$\varphi_{\text{SPP}} = \arcsin \left(\cos \psi_{0\text{-SPP}} \sin \varphi_0 + \sin \psi_{0\text{-SPP}} \cos \varphi_0 \cos(\alpha) \right) \quad (2.33)$$

for the latitude of the pierce point, an α denotes the azimuth to the observed satellite. The longitude of the SPP in radians is derived by the spherical half-angle formula following Hammer, 1897

$$\lambda_{\text{SPP}} = \lambda_0 + \text{sgn}(\sin \alpha) \Delta\lambda, \text{ where} \quad (2.34)$$

$$\Delta\lambda = 2 \arctan \left(\sqrt{\frac{\sin(s - \pi/2 + \varphi_0) \sin(s - \pi/2 + \varphi_{\text{SPP}})}{\sin s \sin(s - \psi_{0\text{-SPP}})}} \right) \quad (2.35)$$

with the auxiliary quantity s given by

$$s = \frac{\pi - (\varphi_0 + \varphi_{\text{SPP}}) + \psi_{0\text{-SPP}}}{2} \quad (\text{in radians}). \quad (2.36)$$

For static observations, it is suitable to precompute all possible pierce point coordinates for a given site, in favour of computation cost in real-time applications. This might even be preferable in case of short distance kinematic navigation purposes. A possible result of a precomputation approach is shown in figure 2.8.

The availability of global ionosphere models is essential in single-frequency PPP applications to reduce the ionospheric effects on both code and phase observables.

2.4.2 Troposphere and Correction of Tropospheric Delay

As mentioned before, it is suitable to divide the atmosphere into a neutral and an ionized layer. Following Seeber, 2003, the neutral part is referred to as troposphere and the charged part is denoted ionosphere. For radio signals up to several GHz, the troposphere is considered a non-dispersive medium and hence no wavelength dependent effects have to be taken into account.

¹⁹with $\cos(90^\circ - \beta) = \sin \beta$ and $\sin(90^\circ - \beta) = \cos \beta$

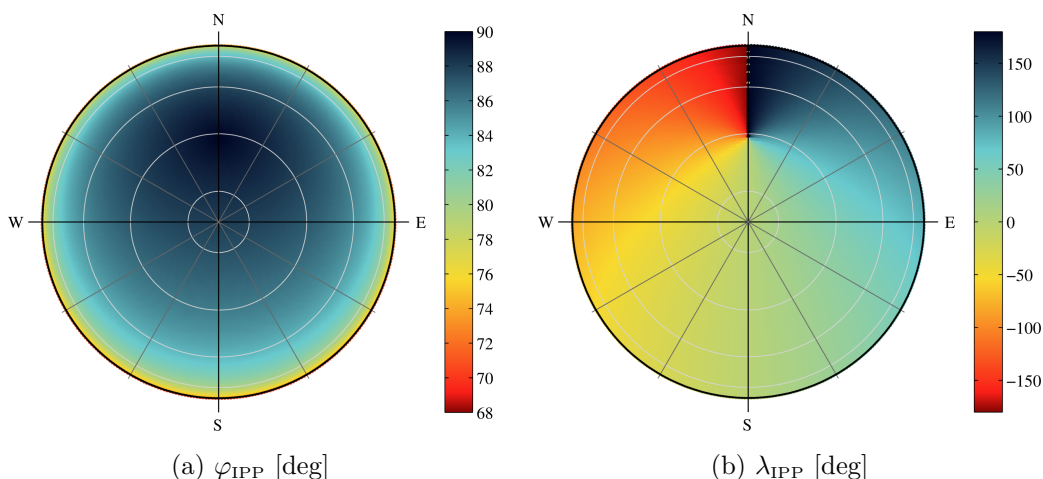


Figure 2.8: Latitudes and longitude values of all possible pierce points as a function of elevation/zenith and azimuth for an observation station at $(\varphi=88^\circ, \lambda=0^\circ)$ with mean earth radius $R=6371$ km and ionospheric thin layer at 450 km altitude.

Nonetheless the troposphere plays an active part in the propagation of radio signals, with the signal traveling through a medium of variable density, humidity and temperature. Therefore the refractive index changes, and hence leads to a refractive delay which will hereafter be denoted as tropospheric delay. Tropospheric effects like ray-bending might be familiar to geodetic users as a common correction term in electronic distance measurement units and even to general public having optical mirages in mind.

Following the deduction in Hofmann-Wellenhof, 2008, p. 128ff, using similar properties as in the deduction of the ionospheric delay Δ^{iono} , the tropospheric delay may be denoted as

$$\Delta^{\text{tropo}} = \int (n - 1) ds_0 \quad (2.37)$$

with the same geometrical path approximation $ds=ds_0$ used as in the ionospheric delay derivation. According to Hopfield, 1969, the refractive index in the troposphere may be decomposed in a *dry* and a *wet* component

$$N^{\text{tropo}} = N_{\text{dry}}^{\text{tropo}} + N_{\text{wet}}^{\text{tropo}} \quad (2.38)$$

where the refractive index n is replaced by the refractivity $N = 10^6(n - 1)$. The tropospheric delay now reads

$$\Delta^{\text{tropo}} \cdot 10^6 = \int N_{\text{dry}}^{\text{tropo}} ds_0 + \int N_{\text{wet}}^{\text{tropo}} ds_0, \quad (2.39)$$

where the tropospheric refractivity at ground level $\underline{N}^{\text{tropo}}$ is

$$\underline{N}_{\text{dry}}^{\text{tropo}} = \underline{a}_1 \frac{p}{T} \quad \text{and} \quad \underline{N}_{\text{wet}}^{\text{tropo}} = \underline{a}_2 \frac{e}{T} + \underline{a}_3 \frac{e}{T^2} \quad (2.40)$$

with T being the absolute temperature in degrees kelvin, p the atmospheric pressure and e the partial water vapor pressure in millibars respectively. The coefficients \underline{a}_1 to \underline{a}_3 represent values that have to be determined empirically.

As a result, the total tropospheric delay Δ^{Tropo} may be modeled as

$$\Delta^{\text{Tropo}}(E) = \downarrow \Delta_{\text{dry}}^{\text{Tropo}} m(E)_{\text{dry}} + \downarrow \Delta_{\text{wet}}^{\text{Tropo}} m(E)_{\text{wet}} \quad (2.41)$$

where $\downarrow \Delta^{\text{Tropo}}$ is defined as the tropospheric delay in zenith direction and the mapping functions $m(E)$ stand for elevation dependent mapping functions for wet and dry components of the troposphere respectively.

To derive an estimate for the tropospheric delay of a received radio signal, the integrals in equation 2.39 have to be evaluated along the signal path from satellite to receiver.

The most prominent models are

- the Hopfield model (cf. Hopfield, 1969) and modified Hopfield models (cf. Goad, 1974),
- Saastamoinen's model of the troposphere (cf. Saastamoinen, 1973) and
- models with mapping functions based on continued fractions (cf. Niell, 1996 or Collins, 1999)

2.4.2.1 Modified Hopfield Model

In 1969 Hopfield empirically showed that the refractivity of the dry part of

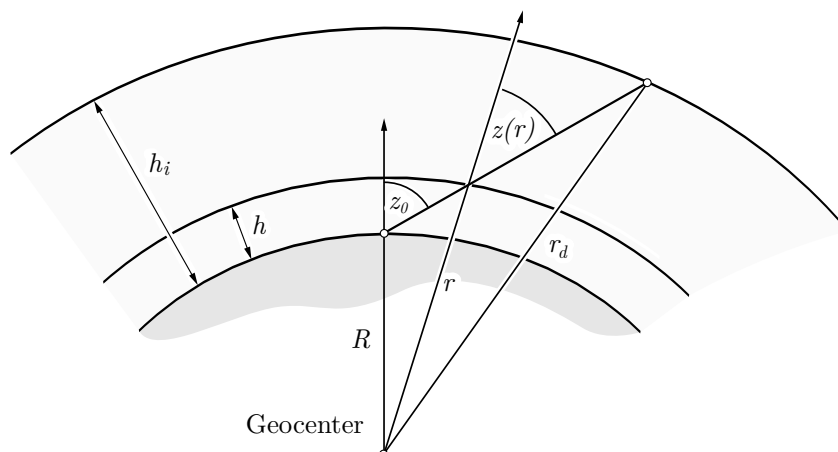


Figure 2.9: Model of the signal path in the modified Hopfield tropospheric model

the troposphere $N_{\text{dry}}^{\text{tropo}}$ might be modeled as a function of the dry refractivity on the ground and is proportional to its height with respect to the ground (cf. Hopfield, 1969). Following the deduction in Hofmann-Wellenhof, 2008, pp. 133ff, let r_d be the geocentric distance of the top of the tropospheric dry layer, R a mean Earth radius and r the geocentric distance to the evaluation point (cf. 2.9). The refractivity is given as

$$N_{\text{dry}}^{\text{tropo}}(r) = \underline{N}_{\text{dry}}^{\text{tropo}} \left(\frac{r_d - r}{r_d - R} \right)^4, \quad (2.42)$$

yielding a tropospheric delay for the dry component

$$\Delta_{\text{dry}}^{\text{tropo}} = 10^{-6} \int_R^{r_d} \underbrace{\frac{1}{\cos z(r)}}_{\text{slant mapping}} \cdot \underbrace{\underline{N}_{\text{dry}}^{\text{tropo}} \left(\frac{r_d - r}{r_d - R} \right)^4}_{\text{function of refractivity}} dr \quad (2.43)$$

where the zenith angle $z(r)$ depends on the radius r . Applying the *law of sines* gives

$$\sin z(r) = \frac{R}{r} \sin z_0 \iff \cos z(r) = \sqrt{1 - (R/r)^2 \sin^2 z_0} \quad (2.44)$$

and a substitution in 2.43 yields

$$\Delta_{\text{dry}}^{\text{tropo}} = \frac{10^{-6} \underline{N}_{\text{dry}}^{\text{tropo}}}{(r_d - R)^4} \int_R^{r_d} \frac{(r_d - r)^4}{\sqrt{1 - (R^2/r^2) \sin^2 z_0}} dr \quad (2.45)$$

for the dry part and

$$\Delta_{\text{wet}}^{\text{tropo}} = \frac{10^{-6} N_{\text{wet}}^{\text{tropo}}}{(r_w - R)^4} \int_R^{r_w} \frac{(r_w - r)^4}{\sqrt{1 - (R^2/r^2) \sin^2 z_0}} dr \quad (2.46)$$

for the wet part of the troposphere. Finally these integrals might be computed using numerical integration, or via a series expansion (cf. Remondi, 1984) leading to

$$\Delta_i^{\text{tropo}}(E) = 10^{-12} N_i^{\text{tropo}} \left(\sum_{k=1}^9 \frac{\alpha_{k,i}}{k} r_i^k \right) \quad (2.47)$$

$$\text{with } r_i = \sqrt{(R + h_i)^2 - R^2 \cos^2 E} - R \sin E \quad (2.48)$$

where the coefficients $\alpha_{k,i}$ are specified via

$$\begin{aligned} \alpha_{1,i} &= 1 & \alpha_{4,i} &= 4a_i(a_i^2 + 3b_i) & \alpha_{7,i} &= b_i^2(6a_i^2 + 4b_i) \\ \alpha_{2,i} &= 4a_i & \alpha_{5,i} &= a_i^4 + 12a_i^2b_i + 6b_i^2 & \alpha_{8,i} &= 4a_ib_i^3 \\ \alpha_{3,i} &= 6a_i^2 + 4b_i & \alpha_{6,i} &= 4a_ib_i(a_i^2 + 3b_i) & \alpha_{9,i} &= b_i^4 \end{aligned} \quad (2.49)$$

and the auxiliary quantities a_i and b_i depend on the elevation E

$$a_i = -\frac{\sin E}{h_i} \quad b_i = -\frac{\cos^2 E}{2h_i R} \quad (2.50)$$

and i identifies either the dry or wet component.

2.4.2.2 Modeling Tropospheric Delay Using Continued Fractions

As mentioned before, the total tropospheric delay might be described as

$$\Delta^{\text{Tropo}}(E) = \downarrow \Delta_{\text{dry}}^{\text{Tropo}} m(E)_{\text{dry}} + \downarrow \Delta_{\text{wet}}^{\text{Tropo}} m(E)_{\text{wet}} \quad (2.51)$$

where $\downarrow \Delta^{\text{Tropo}}$ is defined as the tropospheric delay in zenith direction.

In search for suitable corrections of satellite tracking data, Marini, 1972, approximated the tropospheric delay utilizing continued fractions. Later Herring, 1992 derived a normalized mapping function (unity at zenith) which reads

$$m_k(E) = \frac{1 + \frac{a_k}{1 + \frac{b_k}{1 + c_k}}}{\sin E + \frac{a_k}{\sin E + \frac{b_k}{\sin E + c_k}}} \quad (2.52)$$

where k is to be replaced for the dry and wet component and the respective coefficients

$$\begin{aligned} a_{\text{dry}} &= (1.2320 + 0.0139 \cos \varphi - 0.0209 h + 0.00215 (T - 283)) 10^{-3}, \\ b_{\text{dry}} &= (3.1612 + 0.1600 \cos \varphi - 0.0331 h + 0.00206 (T - 283)) 10^{-3}, \\ c_{\text{dry}} &= (71.244 - 4.293 \cos \varphi - 0.149 h + 0.0021 (T - 283)) 10^{-3} \end{aligned} \quad (2.53)$$

$$\begin{aligned} a_{\text{wet}} &= (0.583 - 0.011 \cos \varphi - 0.052 h + 0.0014 (T - 283)) 10^{-3}, \\ b_{\text{wet}} &= (1.402 + 0.102 \cos \varphi - 0.101 h + 0.0020 (T - 283)) 10^{-3}, \\ c_{\text{wet}} &= (45.85 - 1.91 \cos \varphi - 1.29 h + 0.015 (T - 283)) 10^{-3} \end{aligned} \quad (2.54)$$

where φ (latitude) and h (height) reflect the position and T the temperature in degrees kelvin at the observation site.

Niell, 1996, expands Herring's formulation adding time dependency to the hydrostatic mapping parameters via

$$\begin{pmatrix} a_k(\varphi, t) \\ b_k(\varphi, t) \\ c_k(\varphi, t) \end{pmatrix} = \begin{pmatrix} \bar{a}_k(\varphi) \\ \bar{b}_k(\varphi) \\ \bar{c}_k(\varphi) \end{pmatrix} - \begin{pmatrix} A_k(\varphi) \\ B_k(\varphi) \\ C_k(\varphi) \end{pmatrix} \cos \left(2\pi \frac{t - T_0}{365.25} \right) \quad (2.55)$$

with $\bar{[]}$ representing an average value, A_k , B_k and C_k being regarded as amplitude, t specifying the universal time (UT) days since 0.0 of January and T_0 being the *day-of-year* 28. By adding a height correction term for the dry

component giving

$$m(E)_{\text{dry}} = m(E, a_{\text{dry}}, b_{\text{dry}}, c_{\text{dry}}) + \Delta m(E, H) \quad (2.56)$$

$$= m(E, a_{\text{dry}}, b_{\text{dry}}, c_{\text{dry}}) + \left(\frac{1}{\sin E} - m(E, a_{ht}, b_{ht}, c_{ht}) \right) H \quad (2.57)$$

where E is the satellite elevation and H is the height above sea level in kilometers and a_{ht}, b_{ht}, c_{ht} represent additional height dependent coefficients. The mapping function of the wet component gives

$$m(E)_{\text{wet}} = m(E, a_{\text{wet}}, b_{\text{wet}}, c_{\text{wet}}) \quad (2.58)$$

Niell, 1996, tabulated the coefficients in his paper which are given here in tables 2.5 and 2.6 .

Table 2.5: Coefficients for the wet mapping function $m(E)_{\text{wet}}$

Coefficient	Latitude				
	15°	30°	45°	60°	75°
a_{wet}	5.8021897e-4	5.6794847e-4	5.8118019e-4	5.9727542e-4	6.1641693e-4
b_{wet}	1.4275268e-3	1.5138625e-3	1.4572752e-3	1.5007428e-3	1.7599082e-3
c_{wet}	4.3472961e-2	4.6729510e-2	4.3908931e-2	4.4626982e-2	5.4736038e-2

Table 2.6: Coefficients for the dry mapping function $m(E)_{\text{dry}}$

Coefficient	Latitude				
	15°	30°	45°	60°	75°
\bar{a}_{dry}	1.2769934e-3	1.2683230e-3	1.2465397e-3	1.2196049e-3	1.2045996e-3
\bar{b}_{dry}	2.9153695e-3	2.9152299e-3	2.9288445e-3	2.9022565e-3	2.9024912e-3
\bar{c}_{dry}	62.610505e-3	62.837393e-3	63.721774e-3	63.824265e-3	64.258455e-3
A_{dry}	0.0	1.2709626e-5	2.6523662e-5	3.4000452e-5	4.1202191e-5
B_{dry}	0.0	2.1414979e-5	3.0160779e-5	7.2562722e-5	11.723375e-5
C_{dry}	0.0	9.0128400e-5	4.3497037e-5	84.795348e-5	170.37206e-5
a_{ht}	2.53e-5				
b_{ht}	5.49e-3				
c_{ht}	1.14e-3				

2.5 Additional Correction Steps

In addition to the necessary corrections as described before, the following correction steps are to be taken:

- Relativistic effects
- Effects of solid Earth tides
- Antenna phase center corrections
- Differential code biases

2.5.1 Relativistic Effects

Due to Earth's gravity field and the fairly fast relative movement of satellite and receiver, the two clocks, even if identical and once perfectly synchronized, would start to drift apart caused by relativistic effects.

2.5.1.1 Relativistic Clock Corrections

Relativity affects the frequency of the emitted signal (frequency shift), the satellite and the receiver clock. The frequency shift is eliminated at signal generation by design at the satellite and the receiver related part is included in the receiver clock estimate.

The remaining relativistic clock correction for the satellite yields

$$\delta t^{\text{rel}}(t) = -2 \frac{\mathbf{e}^{\text{sat}}(t) \cdot \dot{\mathbf{p}}^{\text{sat}}(t)}{c^2}, \quad (2.59)$$

encompassing the position and velocity vector of the satellite. Finally adding the correction $\delta t^{\text{rel}}(t)$ to either the broadcast satellite clock correction or a precise clock estimate $\delta t_0^{\text{Sat}}(t)$ gives the corrected satellite clock error $\delta t^{\text{Sat}}(t)$:

$$\delta t^{\text{Sat}}(t) = \delta t_0^{\text{Sat}}(t) + \delta t^{\text{rel}}(t). \quad (2.60)$$

2.5.1.2 Relativistic Range Correction

For precise GNSS measurements even a relativistic range correction due to space-time curvature is calculated by

$$\Delta^{\text{rel}}(t) = 2 \frac{GM}{c^2} \ln \left(\frac{\varrho^{\text{sat}} + \varrho_{\text{rec}} + \varrho_{\text{rec}}^{\text{sat}}}{\varrho^{\text{sat}} + \varrho_{\text{rec}} - \varrho_{\text{rec}}^{\text{sat}}} \right). \quad (2.61)$$

As stated in Hofmann-Wellenhof, 2008, the maximum correction yields 18.6 mm and therefore might be neglected for non-precise applications.

2.5.2 Effects of Solid Earth Tides

Gravitational forces induced by celestial bodies lead to deformations of the figure of Earth. The displacement of a point on Earth's surface is characterized by so called Love numbers h_{nm} and Shida numbers l_{nm} , where n is denoted degree and m is referred to as order of tides' spherical harmonics representation. Strictly speaking, tides affect both the radial and tangent components of a point on the Earth's surface.

The IERS specifies an algorithm to correct tidal station displacement, which divides into two steps:

1. Computation of corrections in the time domain
2. Computation of corrections in the frequency domain

Finally the sum of both corrections has to be added to the station coordinates.

According to the IERS Conventions (cf. Petit et al., 2010), the in-phase radial deformation in time domain due to degree $n = 2$ tides accounts to

$$\begin{aligned} \Delta \mathbf{r} = \sum_{j=2}^3 \frac{GM_j R_e^4}{GM_{\oplus} R_j^3} \left\{ h_2 \hat{\mathbf{r}} \left(\frac{3(\hat{\mathbf{R}}_j \cdot \hat{\mathbf{r}})^2 - 1}{2} \right) + \right. \\ \left. + 3l_2 (\hat{\mathbf{R}}_j \cdot \hat{\mathbf{r}}) [\hat{\mathbf{R}}_j - (\hat{\mathbf{R}}_j \cdot \hat{\mathbf{r}})\hat{\mathbf{r}}] \right\} \end{aligned} \quad (2.62)$$

The variables and constants are defined as

GM_j ... gravitational parameter of the celestial body j

GM_{\oplus} ... gravitational parameter of the Earth

R_e ... equatorial radius of Earth

R_j ... length of the vector between the geocenter and the celest. body j

$\hat{\mathbf{r}}$... unit vector of the station

$\hat{\mathbf{R}}_j$... unit vector of the celestial body j

$h_2 = h_{22}^{(0)}$... Love number nominal values chosen as semidirunal tides j

$l_2 = l_{22}^{(0)}$... Shida number nominal values chosen as semidirunal tides j

Tidal potential effects of degree 3 are only relevant for the moon and range up to a radial displacement of up to 2 mm, which might be neglected for non-precise applications.

In the second step the radial displacement δr caused by the diurnal frequency band has to be computed

$$\delta r = \sin 2\phi \left(\delta R_f^{ip} \sin(\theta_f + \lambda) + \delta R_f^{op} \cos(\theta_f + \lambda) \right) \quad (2.63)$$

where R_f^{ip} are the in-phase and R_f^{op} are the out-of-phase partial radial components for the contributions of frequency f , and the tide argument θ_f for the tidal component of frequency f is derived by

$$\theta_f = m(\theta_g + \pi) - \bar{\mathbf{N}} \cdot \bar{\mathbf{F}} = m(\theta_g + \pi) - \sum_{j=1}^5 N_j F_j \quad (2.64)$$

where the auxiliary quantities relate to

$\bar{\mathbf{F}}$... vector of Delaunay fundamental arguments F_i : $\bar{\mathbf{F}} = (l, l', F, D, \Omega)^T$

$\bar{\mathbf{N}}$... vector of multipliers n_i (at frequency f) of the fundamental arguments

θ_g ... Greenwich Mean Siderial Time (GMST) in angular units

For derivations and numerical computation one is referred to the IERS 2010 Conventions (cf. Petit et al., 2010). The correction for solid Earth tides is not

implemented in the software package developed and might be applied using other software, e.g. NASA's `sotid`²⁰ software package.

Finally a position vector free of the deformation is given by

$$\mathbf{r}_{\text{free}} = \mathbf{r} - \Delta\mathbf{r} - \delta r \frac{\Delta\mathbf{r}}{\|\Delta\mathbf{r}\|} \quad (2.65)$$

2.5.3 Antenna Phase Center Correction

Wherever electromagnetic signals are generated and received, one may encounter the situation that the geometrical center of the antenna does not coincide with the electromagnetic center, or phase center, of the wave either at emission or reception.

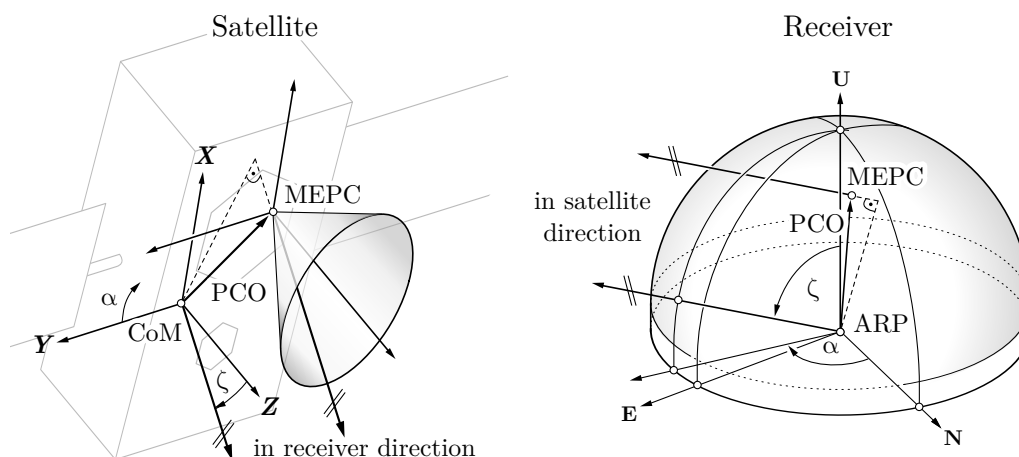


Figure 2.10: Definition of antenna phase center offsets and phase center variations for satellite (left) and receiver station (right)

For precise applications, corrections have to be derived to ensure antenna independent results. Figure 2.10 illustrates the context. The phase center offset (PCO) is defined by the difference vector between a reference point on the antenna and its mean electromagnetic phase center (MEPC). For satellites in space the reference point is specified as the satellite's center of mass (CoM),

²⁰<http://gemini.gsfc.nasa.gov/sotid/>

for receiving stations on ground the antenna reference point (ARP) is either described in the antenna manual, or for common antenna models might be found in the IGS antenna definitions²¹.

The phase center is not stable (therefore a PCO only is related to its the mean position), and varies depending on the wave's direction and its frequency. The magnitude of the variations are in the centimeter level, hence at least for high precision measurements the use of calibrated antennas is advisable.

For phase observations, the resulting correction yields

$$\Delta \text{PCC}(\alpha, \zeta, f) = \Delta \text{PCO}(f) + \Delta \text{PCV}(\alpha, \zeta, f), \quad (2.66)$$

where the phase center variation (ΔPCV) is a function of azimuth, zenith and frequency, and the phase center offset (ΔPCO) is frequency-dependent. The scalar quantity ΔPCO is derived by the dot product

$$\Delta \text{PCO} = \mathbf{PCO} \cdot \frac{\varrho_i^j}{\varrho_i^j} \quad \text{where} \quad \varrho_i^j = \|\varrho_i^j\|_2 \quad (2.67)$$

In addition when using precise orbit products, the position vector of the satellite refers to the center of mass (CoM), instead of the antenna's geometric or phase center. Following the IGS ANTEX v1.4 definition²², the PCO is given in the body-fixed system of the satellite, defined as

- **Z**-axis pointing to the geocenter

$$\mathbf{Z} = -\varrho^{\text{Sat}} / \varrho^{\text{Sat}} \quad (2.68)$$

- **Y**-axis = rotating axis of the solar panels, corresponding to

$$\mathbf{Y} = \mathbf{Z} \times \frac{\varrho_{\text{Sun}} - \varrho^{\text{Sat}}}{\|\varrho_{\text{Sun}} - \varrho^{\text{Sat}}\|} \quad (2.69)$$

- **X**-axis completing the right-handed system

$$\mathbf{X} \times \mathbf{Y} = \mathbf{Z} \quad \text{therefore} \quad \mathbf{Y} \times \mathbf{Z} = \mathbf{X} \quad (2.70)$$

²¹cf. <ftp://igsceb.jpl.nasa.gov/pub/station/general/antenna.gra>

²²cf. <ftp://igsceb.jpl.nasa.gov/pub/station/general/antex14.txt>

where $\boldsymbol{\rho}_{\text{Sun}}$ is the position of the sun in the Earth-fixed system. If PCVs are available one has to be aware that by definition the azimuth counts clockwise from the Y- towards the X-axis.

2.5.4 Differential Code Biases

Following Dach et al., 2007, pp. 279ff, the code biases represent a satellite specific error source, present whenever code- or pseudorange measurements are taken into account and affect the combination of code- and phase-pseudorange. Biases are different for each type of code generated, but are only accessible in a relative sense, therefore the term differential code bias is used. Commonly the combinations

$$B_{P1} - B_{P2} = B_{P1-P2} \quad \text{and} \quad (2.71)$$

$$B_{P1} - B_{C1} = B_{P1-C1} \quad (2.72)$$

are considered, where P represents the P-code on either L1 or L2 and C1 stands for the coarse-acquisition code (C/A). Depending on the type of the receiver in place and the linear combination to be formed, the term to apply to pseudorange measurements differ. The correction term for the C/A code on L1 yields

$$\delta_{\text{code}}^{\text{DCB}} = +1.546 \cdot B_{P1-P2} + B_{P1-C1} \quad (2.73)$$

as given in Dach et al., 2007, p. 283. The biases are varying slowly with time and estimates of 30-days means are available at certain analysis centers, including the *Center of Orbit Determination* (CODE) at the University of Bern.

3 Algorithms

in Single-Frequency PPP

As lined out in the previous chapter, the satellite signal is impaired due to various effects. It is possible to minimize effects by introducing linear combinations of the observables. While such linear combinations are common for homogeneous multi-frequency observables, in the single-frequency case, combinations can only be formed by heterogeneous observables – pseudorange and phase-pseudorange.

3.1 The Geometry-Free Linear Combination

The geometry-free linear combination combines pseudorange and phase observations, canceling the geometric term $\varrho_i^j(t)$,

$$G(t)_i^j = R_i^j(t) - \lambda \Phi_i^j(t) \quad (3.1)$$

and furthermore eliminates the tropospheric effect Δ_{Tropo} on the signal. On the other hand the impact of the ionospheric effect doubles. Taking into account formulas 2.9 and 2.10, this results in the cancellation of the geometric part as well as the elimination of the tropospheric effect and the clock errors:

$$G(t)_i^j = -\lambda N_i^j(t) + 2\Delta^{\text{Iono}}_i^j(t) + \delta\Delta(t)_i^j + \varepsilon(R_i^j, \Phi_i^j) \quad (3.2)$$

Although, due to the cancellation of the geometric term, no estimation of coordinates is possible, this combination might be suitable to monitor ambiguity changes.

According to Subirana, 2013, the assumption that the ionospheric variation is considerably small for short periods of time, allows for the ionospheric part to be considered constant. Therefore, taking differences of consecutive epochs, it enables users to observe changes in satellite ambiguities ΔN .

$$\Delta G(t_{i+1}) = G(t_{i+1}) - G(t_i) = -\lambda (N_i^j(t_{i+1}) - N_i^j(t_i)) + \varepsilon \quad (3.3)$$

$$= -\lambda \Delta N_i^j + \varepsilon \quad (3.4)$$

One should be aware that the combination of pseudorange and phase observations results in an increase of measurement noise, which is even amplified by forming differences.

3.2 Detection of Cycle-Slips

As mentioned in section 2.2.3.2, a loss of lock in the receiver introduces changes in the unknown phase ambiguity N . For precise applications, that make any use of phase observations, either directly used or used in a smoothing filter, it is necessary to detect these changes.

In the case of single frequency measurements the geometry-free linear combination is considered for cycle-slip detection.

According to Subirana, 2013, two algorithms are suitable in the single-frequency case, and are therefore used in the software package (cf. section 4.3.5)

3.2.1 Test Residuals of Polynomial Fit

The residual biases in the geometry-free linear combination due to propagation effects are still present. Ionospheric effects are considered constant, but

pseudorange variations (e.g. multipath effects) introduce time-varying noise in this combination.

To overcome the inability to detect ambiguity changes directly solely based on a single measurement, it was proposed in Subirana, 2013, to fit a polynomial of certain degree n to a moving measurement data window of size M . The residual of predicted polynomial value and the measured value is computed and a cycle slip declared, if the value is above a given threshold.

The following algorithm describes the polynomial fit approach (cf. Subirana, 2013, p.90f), for a geometry-free linear combination $G(k)$ at the current epoch k :

1. Retrieve most recent M observations $G(k - M, k - 1)$ after the last cycle-slip flag and save them in an array $A(k - M, k - 1)$
 Check if the time difference Δt_i between consecutive observations is smaller than a maximum data outage limit ΔT_{lim} – if bigger set cycle-slip flag.
2. Fit a polynomial P_n of order n to the retrieved data in A
3. Predict the polynomial values $P_n(k)$ at most recent epoch k .
4. Compute difference $\Delta(k) = |P_n(k) - G(k)|$
5. If $\Delta(k) > \Delta_{MAX}$, where Δ_{MAX} is a selected threshold, flag current epoch as a cycle-slip.

The size of the moving window $[k - M, k - 1]$ (and therefore M), as well as the threshold Δ_{MAX} might be dynamically selected – or fixed by empirical knowledge.

3.2.2 Deviation from Arithmetic Mean

The second approach (cf. Subirana, 2013, p.91f) features the computation of mean values and deviations for a given moving data window of a size up to M . For every epoch k , and each satellite:

1. Retrieve the most recent M observations $G(k - M, k - 1)$ after the last cycle-slip flag and save them in an array $A(k - M, k - 1)$
Check if the time difference Δt_i between consecutive observations is smaller than a maximum data outage limit ΔT_{lim} – if bigger set cycle-slip flag.
2. Compute the *Sample Mean* (SA)

$$\bar{G}(k - 1) = \frac{1}{M} \sum_{i=1}^M G(k - i) \quad (3.5)$$

as well as the *Sample Standard Deviation* (SSD)

$$\bar{S}(k - 1) = \sqrt{\frac{1}{M - 1} \sum_{i=1}^M (G(k - i) - \bar{G}(k - 1))^2} \quad (3.6)$$

3. Compute deviation $D(k) = |G(k) - \bar{G}(k - 1)|$
4. If $D > Q \cdot \bar{S}(k - 1)$ set cycle-slip flag at current epoch k (where Q is the confidence factor – 3 to 6 standard sigmas)

For small windows sizes M , as in the initialization process, or when a cycle slip was present during the preceding epoch, the estimate for the SSD might be unrealistic. In such cases the introduction of a smoothing filter

$$\hat{S}^2(k - 1) = \frac{M - 1}{M} S^2(k - 1) + \frac{1}{M} S_0^2 \quad , \quad (3.7)$$

where S_0 is chosen as an appropriate initial value, will help circumventing false-positive cycle-slip detection.

When replacing the SA by the *Median*, which is identical to the middle value of a sorted list of items, and the SSD by the *Median Absolute Deviation* (MAD_E), a robust estimation detection of cycle slips might be available.

Both algorithms are implemented in the developed software package and may be activated in the configuration file.

3.3 Pseudorange Smoothing Using Carrier Phases

Regarding overall precision, pseudorange measurements based on code evaluations are considered inferior to the precision of phase measurements (cf. Subirana, 2013).

A method to increase pseudorange based positioning precision is to smooth the pseudorange observations using carrier phase measurements.

This is accomplished by implementing a weighted smoothing technique:

1. If a cycle-slip is present at the current epoch, set weight $w = 1$ and initialize the algorithm, else compute the smoothing weight

$$w = 1 - \alpha K, \quad (3.8)$$

where α specifies a weight-gain per epoch and K is the number of epochs within a continuous phase observations segment (no cycle-slip occurred).

2. Extrapolate current pseudorange, using

$$R_{ex}(t_i) = R(t_0) + \lambda(\Phi(t_i) - \Phi(t_0)) = R(t_0) + \lambda \Delta\Phi(t_i, t_0), \quad (3.9)$$

where $R(t_0)$ is the initial pseudorange and $\Phi(t_0)$ is the initial phase observation at the beginning of the current continuous segment (last cycle-slip).

3. Compute the smoothed, weighted pseudorange at current epoch

$$\tilde{R}(t_i) = w R(t_i) + (1 - w) R_{ex}(t_i) \quad (3.10)$$

In order to minimize the noise of the initial pseudorange observation $R(t_0)$, it is possible to apply the arithmetic mean. Reshaping equation 3.9 gives

$$R(t_0) = R(t_i) - \lambda \Delta\Phi(t_i, t_0). \quad (3.11)$$

The arithmetic mean for M epochs yields

$$\bar{R}(t_0) = \frac{1}{M} \sum_{i=1}^M R_i(t_0) \quad (3.12)$$

3.4 Least Squares Estimation and Kalman Filtering

This section gives a brief overview of *Least Squares Estimation* (LSQE) and *Kalman Filtering* (KF), which are essential tools to derive the state of an object of interest, based on observations.

3.4.1 Least Squares Estimation by Parameters

Let \mathbf{x} be a $(n \times 1)$ vector consisting of unknown parameters, describing the state of an arbitrary object in space, e.g. its coordinates. In addition let \mathbf{z} be a $(m \times 1)$ vector of observations, e.g. observing a distance to an object, which is dependent on the behavior of the object, represented by its unknown parameters. Furthermore, real-world observations go hand-in-hand with measurement noise, therefore a noise vector \mathbf{v} (same size as the observation vector) is introduced.

The relation between observations \mathbf{z} and unknown parameters \mathbf{x} may now be modeled by

$$\mathbf{z} = \mathbf{f}(\mathbf{x}) + \mathbf{v} \quad (3.13)$$

where \mathbf{f} is the function that connects observations and parameters. In the simple case of linear equations, a matrix \mathbf{H} – design or configuration matrix – is introduced, reshaping the equation to

$$\mathbf{z} = \mathbf{H}\mathbf{x} + \mathbf{v}. \quad (3.14)$$

Non-linear functions have to be expanded in a Taylor series

$$\mathbf{f}(\mathbf{x}) = \mathbf{f}(\mathbf{x}_0) + \underbrace{\begin{pmatrix} \partial f_1/\partial x_1 & \dots & \partial f_1/\partial x_m \\ \vdots & \ddots & \vdots \\ \partial f_n/\partial x_1 & \dots & \partial f_n/\partial x_m \end{pmatrix}}_{\mathbf{H}_0} (\mathbf{x} - \mathbf{x}_0) + \dots \quad (3.15)$$

rendering equation 3.14 to

$$\delta \mathbf{z} = \mathbf{z} - \mathbf{z}_0 = \mathbf{H}_0(\mathbf{x} - \mathbf{x}_0) + \mathbf{v} = \mathbf{H}_0 \delta \mathbf{x} + \mathbf{v} \quad (3.16)$$

which will have to be solved iteratively. Following Hofmann-Wellenhof et al., 2011, for overdetermined systems ($n > m$), the best, unbiased estimate, where the sum of square residuals

$$\mathbf{v}^T \mathbf{R}^{-1} \mathbf{v} \stackrel{!}{=} \min. \quad (3.17)$$

is minimum is given by:

$$\text{Estimated Covariance Matrix} \quad \mathbf{P} = (\mathbf{H}^T \mathbf{R}^{-1} \mathbf{H})^{-1} \quad (3.18)$$

$$\text{Estimated Parameters} \quad \hat{\mathbf{x}} = (\mathbf{H}^T \mathbf{R}^{-1} \mathbf{H})^{-1} \mathbf{H}^T \mathbf{R}^{-1} \mathbf{z} \quad (3.19)$$

where \mathbf{R} is the covariance matrix of observations \mathbf{z} . For each time epoch t_i , based on m observations an estimate of the state vector \mathbf{x} and its covariance matrix \mathbf{P} may be derived in this way.

3.4.2 Kalman Filtering

In kinematic applications, the use of a dynamic model that establishes a connection between two consecutive epochs provides additional information for state vector estimation, and even enables state estimation at time epochs, where no measurements are available. The (discrete) Kalman Filter is an algorithm that makes use of both an observation model and a dynamic model:

$$\text{Observation Model:} \quad \mathbf{z}_k = \mathbf{H}_k \mathbf{x}_k + \mathbf{v}_k \quad \mathbf{v}_k \sim \mathcal{N}(0, \mathbf{R}_k) \quad (3.20)$$

$$\text{Dynamic Model:} \quad \mathbf{x}_{k+1} = \mathbf{\Phi}_k \mathbf{x}_k + \mathbf{w}_k \quad \mathbf{w}_k \sim \mathcal{N}(0, \mathbf{Q}_k) \quad (3.21)$$

The Kalman Filter, introduced by Rudolf Emil Kálmán in 1960 (cf. Kalman and Bucy, 1961) is a standard tool in common navigation toolboxes.

Consider an object moving in space, and consider furthermore that the state of the object, e.g. its position and velocity, is of interest at any given time in the future.

The observation model is identical to the one used in the LSQE technique, where $\mathcal{N}(0, \mathbf{R})$ specifies white noise, centered at zero and described by a covariance matrix \mathbf{R} , with the additional index k , which reflects a certain measurement epoch.

The dynamic model, as stated before, models the transition between two consecutive epochs k and $k + 1$, which is given by the *transition matrix* Φ_k . This transition is subject to noise, due to incomplete modeling. This noise is stochastically described by its covariance matrix \mathbf{Q}_k and centered at zero.

Following the outline given in Hofmann-Wellenhof et al., 2011, p. 53, the filter algorithm consists of 3 steps:

1. *Kalman Gain Computation*

Compute Kalman weight

$$\mathbf{K}_k = \tilde{\mathbf{P}}_k \mathbf{H}_k^T \left(\mathbf{H}_k \tilde{\mathbf{P}}_k \mathbf{H}_k^T + \mathbf{R}_k \right)^{-1}, \quad (3.22)$$

which acts as a balancing weight between new measurements and the predicted state, based on the respective covariances.

2. *Measurement Update*

Correct the predicted state vector $\tilde{\mathbf{x}}_k$ and (corrected) covariance matrix $\tilde{\mathbf{P}}_k$, utilizing

$$\hat{\mathbf{x}}_k = \tilde{\mathbf{x}}_k + \mathbf{K}_k (\mathbf{z}_k - \mathbf{H}_k \tilde{\mathbf{x}}_k) \quad (3.23)$$

$$\mathbf{P}_k = (\mathbf{I} - \mathbf{K}_k \mathbf{H}_k) \tilde{\mathbf{P}}_k, \quad (3.24)$$

and therefore gain the *corrected* state $\hat{\mathbf{x}}_k$ and the *corrected* covariance \mathbf{P}_k

3. *Time Update*

Predict state vector and covariance transition from k to $k+1$, rendering a predicted state vector $\tilde{\mathbf{x}}_{k+1}$ and a covariance matrix $\tilde{\mathbf{P}}_{k+1}$

$$\tilde{\mathbf{x}}_{k+1} = \Phi_k \hat{\mathbf{x}}_k \quad (3.25)$$

$$\tilde{\mathbf{P}}_{k+1} = \Phi_k \mathbf{P}_k \Phi_k^T + \mathbf{Q}_k \quad (3.26)$$

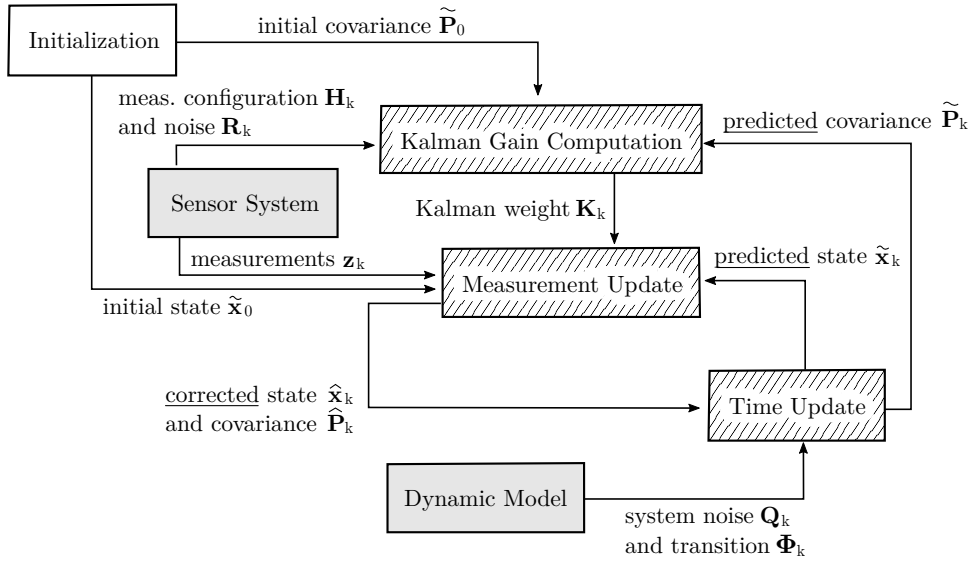


Figure 3.1: Overview of the Kalman filtering process

To model a state transition between two consecutive epochs, the kinematic properties of an object might be investigated. For convenience, assume that the object of interest is constrained to a constant acceleration

$$\ddot{\mathbf{x}}_{k+1} = \ddot{\mathbf{x}}_k = \text{const}. \quad (3.27)$$

In this case, integration over a time period Δt yields

$$\dot{\mathbf{x}}_{k+1} = \dot{\mathbf{x}}_k + \ddot{\mathbf{x}}_k \Delta t \quad (3.28)$$

for the velocity $\dot{\mathbf{x}}_{k+1}$ with an integration constant $\dot{\mathbf{x}}_k$ and an additional integration finally yields the position

$$\mathbf{x}_{k+1} = \mathbf{x}_k + \dot{\mathbf{x}}_k \Delta t + (\ddot{\mathbf{x}}_k/2) \Delta t^2, \quad (3.29)$$

where \mathbf{x}_k reflects the position of the object in the preceding epoch. Δt is referred to as the time interval between two neighboring epochs. The kinematics of an object with constant velocity may be derived in a similar manner:

$$\text{Velocity: } \dot{\mathbf{x}}_{k+1} = \dot{\mathbf{x}}_k = \text{const}, \quad (3.30)$$

$$\text{Position: } \mathbf{x}_{k+1} = \mathbf{x}_k + \dot{\mathbf{x}}_k \Delta t. \quad (3.31)$$

In the constant velocity case, this leads to a state transition matrix

$$\Phi_k = \begin{pmatrix} 1 & 0 & 0 & \Delta t & 0 & 0 \\ 0 & 1 & 0 & 0 & \Delta t & 0 \\ 0 & 0 & 1 & 0 & 0 & \Delta t \\ 0 & 0 & 0 & 1 & 0 & 0 \\ 0 & 0 & 0 & 0 & 1 & 0 \\ 0 & 0 & 0 & 0 & 0 & 1 \end{pmatrix} \quad \text{regarding a state vector} \quad \mathbf{x}_k = \begin{pmatrix} x_0 \\ x_1 \\ x_2 \\ \dot{x}_1 \\ \dot{x}_2 \\ \dot{x}_3 \end{pmatrix} \quad (3.32)$$

As a result, the omission of possibly unmodeled accelerations leads to an uncertainty, which is modeled as the dynamic system noise and is represented by the noise matrix \mathbf{Q}_k . This noise matrix is obtained utilizing covariance propagation of this disturbing acceleration, which directly influences the predicted state vector and hence the predicted covariance matrix $\tilde{\mathbf{P}}_{k+1}$ (cf. equation 3.26).

$$\mathbf{Q}_k = \mathbf{N}_k \Sigma_{k_{acc}} \mathbf{N}_k^T \quad (3.33)$$

where the the disturbing accelerations are modeled by

$$\Sigma_{k_{acc}} = \begin{pmatrix} \sigma_0^2 & 0 & 0 \\ 0 & \sigma_1^2 & 0 \\ 0 & 0 & \sigma_2^2 \end{pmatrix} \quad \text{and} \quad \mathbf{N}_k = \begin{pmatrix} \Delta t^2/2 & 0 & 0 \\ 0 & \Delta t^2/2 & 0 \\ 0 & 0 & \Delta t^2/2 \\ \Delta t & 0 & 0 \\ 0 & \Delta t & 0 \\ 0 & 0 & \Delta t \end{pmatrix} \quad (3.34)$$

represent the derivatives of equations 3.27-3.29 with respect to the disturbing acceleration and hence relate the disturbing accelerations to the state vector.

The dynamic model chosen should reflect the use-case scenario. For pedestrian applications, where a person moves at constant speed $\dot{\mathbf{x}}$, a non-accelerated model of motion may be adequate.

4 Software Development and Implementation

This chapter outlines the development of a PPP software. First objectives for a PPP application are laid out and discussed. The program structure, the frameworks, third party software, and libraries are listed and their scope of application is discussed. Finally the software structure is outlined and main capabilities of the software package are characterized.

4.1 Objectives

The purpose of GNSS based positioning applications is to observe or monitor an object, either in motion or in the stationary case. As lined out in the previous chapters, PPP is a suitable technique to fulfill the requirements of precise position determination. Hence the development of programs that implement PPP algorithms are at hand.

In this thesis a software package is developed that aims to achieve the following goals:

- real-time capable processing of GNSS data
- kinematic positioning
- running on low-cost hardware
- suitable for urban navigation

Figure 4.1 illustrates a coarse overview of the software components.

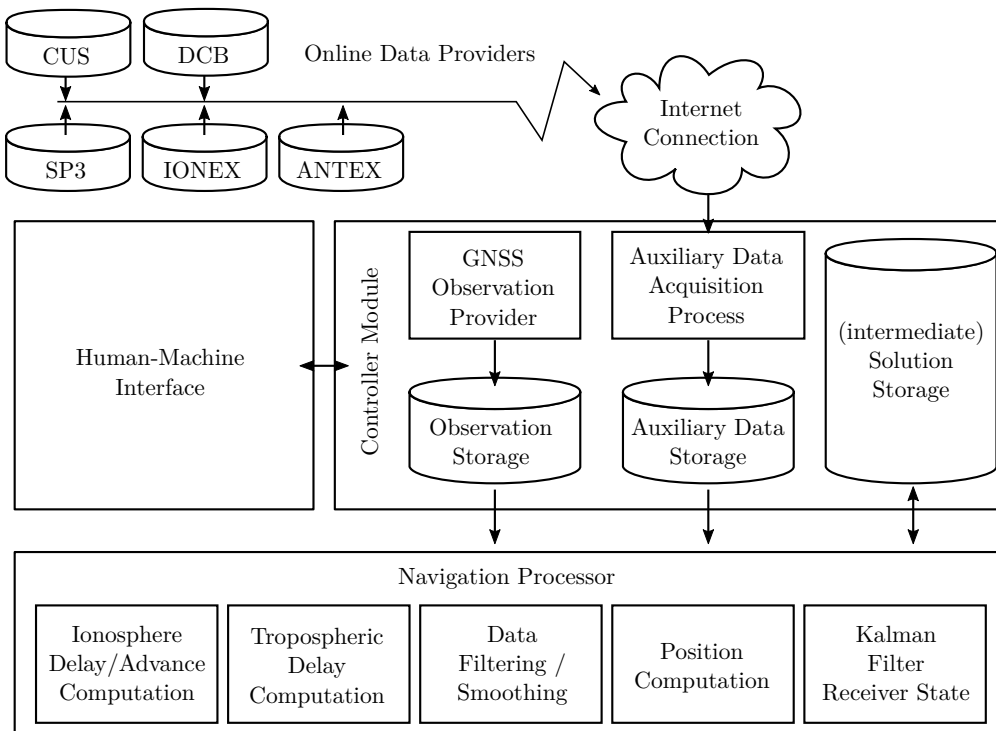


Figure 4.1: Overview of system components

The software is characterized by three main components:

1. Human-Machine-Interface (HMI):

This component allows a user to interact with the program. It allows a user to specify certain configuration properties, such as remote resources. In addition, this component provides a graphical user interface, with information in- and output, such as a graphical display of the user's position.

2. Controller Module (CM):

This module provides the central part of the application. It incorporates interfaces to invoke methods for remote file transfers (auxiliary data acquisition) and stores the data in designated data structures, for obser-

vation data retrieval as well as to control the navigation processor. An interface between controller and HMI is necessary for user interaction.

3. Navigation Processor (NP):

GNSS processing and filtering, as discussed in the previous chapters, is performed within this module. It provides methods to determine the user's position as well as data processing tools, correction algorithms, and performs modeling of atmospheric effects.

These software modules have to be able to interact hand in hand, so that a user is capable to determine it's position. In a common use-case scenario it is assumed that the user is able to download remote data – or that there is at least an internet connection available when the program is started. Following this first initialization step, the user declares the source for observation data and commences data processing by explicit interaction with the HMI. The controller module will initiate the data processing in the navigation processing module with the specified options. The navigation processor performs the computations and reports the results back to the controller, which finally presents the results to the user via the human-machine-interface. The user may now either monitor the solution or stop the process.

The software developed in this thesis should fulfill the requirements to:

1. Run the program and specify the (optional) data sources.
2. Set up options for data processing and computation.
3. Retrieve additional remote data if necessary.
4. Enable/Activate the computation, i.e. start the processing of data and perform position computation.
5. Monitor the results or Stop the program.

4.2 Input Data Formats and Data Sources

As outlined in chapter 2, in addition to the observational data – pseudo range and phase – auxiliary data is needed to correct the raw signal and account for

atmospheric effects and satellite specific errors. These models and corrections are available in different file formats and are obtainable at different remote data center locations, as shown in sections 4.2.1 to 4.2.4

4.2.1 Extended Standard Product 3 Orbit Format (SP3)

The *Extended Standard Product 3* orbit format (cf. Hilla, 2010), is a file format used to store specific satellite orbit data of different GNSS within a single ASCII file.

The file is structured in a fixed length header of 22 lines, which stores information regarding file type, time, and coordinate reference as well as the responsible agency and a part where position and clock data for each satellite at consecutive epochs are stored. Table 4.1 gives an overview of meta data stored in the file data header.

Table 4.1: SP3 file format header.

#c	P	2015	3	3	0	0	0.00000000										192	ORBIT	IGS08	BHN	ESOC	Version Symbol	
##	1834	172800.00000000					900.00000000										57084	0.00000000					Position/Velocity Flag
+	55		G32	G04	G08	G10	G14	G13	G28	G21	G11	G22	G20	G18	G16	G19	G23	G02	G31				Date(y/m/d/h/m/s)
+			G17	G12	G15	G29	G07	G05	G25	G01	G30	G24	G27	G06	G09	G03	R08	R10	R11				Number of Epochs
+			R13	R14	R15	R19	R20	R01	R06	R05	R22	R24	R23	R09	R12	R16	R04	R03	R07				Data used
+			R17	R02	R18	R21																	Coordinate System
+				0	0	0	0	0	0	0	0	0	0	0	0	0	0	0	0	0	0	0	Orbit Type
++				4	5	4	5	4	4	5	5	5	5	5	5	4	4	5	5				Agency
++				4	5	4	4	5	4	5	5	5	5	5	4	5	5	5	7				GPS Week
++				6	6	7	6	6	6	5	6	6	5	6	6	6	5	6	5				Seconds of Week
++				5	5	6	6	0	0	0	0	0	0	0	0	0	0	0	0				Epoch Interval
++				0	0	0	0	0	0	0	0	0	0	0	0	0	0	0	0				Mod. Julian Day
%c	M	cc	GPS	ccc	cccc	cccc	cccc	cccc	cccc	cccc	cccc	cccc	cccc	cccc	cccc	cccc	cccc	cccc					Fractional Day
%c	cc	cc	ccc	ccc	cccc	cccc	cccc	cccc	cccc	cccc	cccc	cccc	cccc	cccc	cccc	cccc	cccc	cccc					Number of Satellites
%f	0.00000000			0.00000000				0.00000000					0.00000000										Satellite System Indicator
%f	0.00000000			0.00000000				0.00000000					0.00000000										Satellite Number
%i		0		0		0		0		0		0		0		0		0					Accuracy
%i		0		0		0		0		0		0		0		0		0					File Type
/*	CCCCCCCCCCCC	CCCCCCCCCCCC	CCCCCCCCCCCC	CCCCCCCCCCCC	CCCCCCCCCCCC	CCCCCCCCCCCC	CCCCCCCCCCCC	CCCCCCCCCCCC	CCCCCCCCCCCC	CCCCCCCCCCCC	CCCCCCCCCCCC	CCCCCCCCCCCC	CCCCCCCCCCCC	CCCCCCCCCCCC	CCCCCCCCCCCC	CCCCCCCCCCCC	CCCCCCCCCCCC	CCCCCCCCCCCC					Time System
/*	CCCCCCCCCCCC	CCCCCCCCCCCC	CCCCCCCCCCCC	CCCCCCCCCCCC	CCCCCCCCCCCC	CCCCCCCCCCCC	CCCCCCCCCCCC	CCCCCCCCCCCC	CCCCCCCCCCCC	CCCCCCCCCCCC	CCCCCCCCCCCC	CCCCCCCCCCCC	CCCCCCCCCCCC	CCCCCCCCCCCC	CCCCCCCCCCCC	CCCCCCCCCCCC	CCCCCCCCCCCC	CCCCCCCCCCCC					Base for Pos/Vel
/*	CCCCCCCCCCCC	CCCCCCCCCCCC	CCCCCCCCCCCC	CCCCCCCCCCCC	CCCCCCCCCCCC	CCCCCCCCCCCC	CCCCCCCCCCCC	CCCCCCCCCCCC	CCCCCCCCCCCC	CCCCCCCCCCCC	CCCCCCCCCCCC	CCCCCCCCCCCC	CCCCCCCCCCCC	CCCCCCCCCCCC	CCCCCCCCCCCC	CCCCCCCCCCCC	CCCCCCCCCCCC	CCCCCCCCCCCC					Base for Clk/Rate
/*	PCV:IGS08_1832	OL/AL:FES2004	NONE															Y	N	ORB:CON	CLK:CON		

Listing 4.1: Excerpt of an example SP3c file

```

23 *201207200000.00000000
24 PG3213270.3267078074.53168421749.938085-467.043849
25 PG26-13303.841962-12970.021010-19737.816889-341.340822
...
76 PR17-13691.6250057727.058420-20071.18405832.735163
77 *20120720001500.00000000
78 ...
79 EOF

```

The actual (predicted) satellite orbit data records follow the scheme displayed in listing 4.1. Starting with an epoch header indicated by a single asterisk '*', where the date and time of the current epoch is stored, each following line entry represents a satellite data record with satellite PRN and the X,Y and Z-coordinates of the satellites center of mass (CoM).

The file continues for as many epochs as specified in the header until the end of file (EOF).

4.2.2 The Ionosphere Map Exchange Format (IONEX)

The *Ionosphere Map Exchange Format Version 1* (IONEX) (cf. Schaer et al., 1998), was proposed in 1998 to enable the *International GNSS Service* (IGS) community to exchange global TEC maps in plain ASCII files.

The IONEX format is used to store global ionospheric maps, obtained by modeling the atmosphere on the basis of purely theoretical models or direct satellite measurements.

Furthermore, the data format is capable of storing either 2- or 3-dimensional ionosphere data. It is mandatory to provide information about what satellite system or what theoretical model was used to derive the TEC values.

The file consists of a non-fixed-size header section, storing meta data, and a data section, where TEC values are recorded for each epoch in a regular manner according to the information in the header section.

The format, due to its variable length header, is capable of storing valuable additional information in comment or description lines or blocks. This is the place to lay out detailed information, such as how measurements have been obtained, what procedures have been used to derive model parameters of a global TEC distribution.

Table 4.2 lists records that are used to store map specific data records. Table 4.3 lists header data records of the IONEXv1 data specification.

Table 4.2: IONEX map data record format.

Line Indicator	Description	Format
START OF TEC MAP	Indicates start of specified TEC map	I6,54X
EPOCH OF CURRENT MAP	Mandatory first record within map Epoch of current map (UT) <ul style="list-style-type: none"> • Year • Month • Day • Hour • Minute • Second 	I6 I6 I6 I6 I6 I6,26X
LAT/LON1/LON2/DLON/H	<ul style="list-style-type: none"> • Current latitude • Start longitude • Stop longitude • Longitude interval • Current height 	2X,F6.1 F6.1 F6.1 F6.1 F6.1
END OF TEC MAP	Observation records, consisting of multiple values of data length 5 without specific line termination indicator Indicates end of specific TEC map	multiple I5 I6,54X
END OF FILE	Closing record of the file	60X

Format Description: F8.1 (float, length 8, 1 decimal); 2X (2 blank spaces); A2 (2 ASCII characters); I6 (integer, length 6)

4.2.3 Antenna Exchange Format Version 1.4

Section 2.5.3 introduces antenna phase center offset correction. To apply these corrections, the actual values have to be known. The IGS maintains a list of satellite and even receiver specific antenna corrections stored in the *Antenna Exchange* (ANTEX) format.

4 Software Development and Implementation

The ANTEX format in its current version 1.4 is designed to store phase center data and variations for satellites and receivers respectively.

Table 4.3: IONEX header data records

Line Indicator	Description	Format
IONEX VERSION / TYPE	Mandatory first line in file <ul style="list-style-type: none"> • Format Version • File Type • Satellite System 	F8.1,12X A1,19X A3,17X
PGM / RUN BY / DATE	<ul style="list-style-type: none"> • Name of creating program • Name of creating agency • Date and time of file creation 	A20 A20 A20
COMMENT	(Multi-)Line Comment record	A60
DESCRIPTION	(Multi-)Line Description record	A60
EPOCH OF FIRST MAP	<ul style="list-style-type: none"> • Year • Month • Day • Hour • Minute • Seconds in UT 	I6 I6 I6 I6 I6 I6,24X
EPOCH OF LAST MAP	See EPOCH OF FIRST MAP	6×I6, X24
INTERVAL	Time Interval between TEC map (UT)	I6, 54X
# OF MAPS IN FILE	Total number of TEC/RMS/HGT maps	I6, 54X
MAPPING FUNCTION	Mapping function adopted for TEC determination	2X,A4,54X
ELEVATION CUTOFF	Minimum elevation angle in degrees	F8.1,52X
OBSERVABLES USED	Specifications of used observables	A60
BASE RADIUS	Mean earth radius or bottom of height in km	F8.1,52X
MAP DIMENSION	Dimension of TEC/RMS maps	I6,52X
HGT1 / HGT2 / DHGT	Definition of equidistant grid (height): <ul style="list-style-type: none"> • Start Height • Stop Height • Interval 	2X,F6.1 F6.1 F6.1,40X
LAT1 / LAT2 / DLAT	Definition of equidistant grid (latitude)	2X,3×F6.1,40X
LON1 / LON2 / DLON	Definition of equidistant grid (longitude)	2X,3×F6.1,40X
EXPONENT	Defines the unit of the values	I6,54X
END OF HEADER	Specifies the end of file header	A60

Format Description: F8.1 (float, length 8, 1 decimal); 2X (2 blank spaces); A2 (2 ASCII characters); I6 (integer, length 6)

Table 4.4: ANTEX header data records

Line Indicator	Description	Format
ANTEX VERSION / SYST OF TEC MAP	<ul style="list-style-type: none"> • Format version • Satellite system 	F8.1,12X A1,39X
PCV TYPE / REFANT	<ul style="list-style-type: none"> • Phase center variation type • Reference antenna type for relative values • Serial number of the reference antenna (opt.) 	A1,19X A20 A20
COMMENT	(Multi-) Line comment	A60
END OF HEADER	Record indicates end of header	60X

Format Description: F8.1 (float, length 8, 1 decimal); 2X (2 blank spaces); A2 (2 ASCII characters); I6 (integer, length 6)

Within a single ASCII file, structured in file header (Table 4.4) and subsequent antenna data section (Table 4.5), similar to the IONEX file, antenna correction parameters are stored for each satellite/receiver and furthermore for each signal frequency.

Antenna data is only valid for a certain period of time, hence there is a need to store correction records in a way to reflect their validity.

For official IGS models, the data records follow an ordering scheme (satellites only):

1. Sort by satellite systems
GPS→GLONASS→Galileo→Compass→QZSS→SBAS
2. Sort by satellite code (G01,G02,...)
3. Sort by 'SERIAL NO'

4.2.4 Differential Code Bias Data (DCB)

The differential code bias (DCB) is essential when using precise ephemeris and clocks and is gained as a byproduct in the process of ionosphere maps estimation (cf. Schaer et al., 1998). This is the reason, why the IONEX v1 file standard is capable of storing DCB values as well. The format definition is outlined as:

- Satellite Indicator (A3, e.g. G02 for GPS PRN 2)

4 Software Development and Implementation

Table 4.5: ANTEX antenna data records (satellite antenna only)

Line Indicator	Description	Format
START OF ANTENNA	Record indicates start of antenna data section	60X
TYPE / SERIAL NO	Satellite antenna: <ul style="list-style-type: none"> • Antenna Type (e.g. BLOCK IIA) • Satellite code "sNN" • Satellite code (opt.) • COSPAR ID "YYYY-XXXX" (opt.) 	A20 A20 A10 A10
METH / BY / # / DATE	<ul style="list-style-type: none"> • Calibration method • Name of agency • Number of individual antennas calibrated • Date 	A20 A20 I6,4X A10
DAZI	Increment of the azimuth	2X,F6.1,52X
ZEN1 / ZEN2 / DZEN	Definition of the grid in nadir: <ul style="list-style-type: none"> • Start nadir (degrees) • Stop nadir (degrees) • Step interval 	2X,F6.1 F6.1 F6.1,40X
# OF FREQUENCIES	Number of frequencies available	I6,54X
VALID FROM	Start of validity period (GPS time) <ul style="list-style-type: none"> • Year • Month • Day • Hour • Minute • Second 	I6 I6 I6 I6 I6 F13.7,17X
VALID UNTIL	see VALID FROM	5×I6,F13.7,17X
SINEX CODE	Name of antenna calibration model to be used in SINEX format (for ref. purposes)	A10,50X
COMMENT*	Comments line (only allowed at this position)	A60
START OF FREQUENCY	Record indicates start of frequency section consistent with RINEX definition <ul style="list-style-type: none"> • Satellite system indicator (e.g G) • Satellite frequency (e.g. 01) (e.g. G01 for GPS L1)	3X,A1 I2,54X
NORTH / EAST / UP	Eccentricities of the mean antenna phase center relative to the center of mass (COM) <ul style="list-style-type: none"> • X [mm] • Y [mm] • Z [mm] 	F10.2 F10.2 F10.2,30X
	The flag NOAZI denotes a non-azimuth dependent pattern from ZEN 1 to ZEN 1 in DZEN steps	3X,A5,mF8.2
END OF FREQUENCY	Record indicates end of specified frequency (e.g. G01)	3X,A1,I2,54X
END OF ANTENNA	Record indicates the end of antenna data listing	60X

Format Description: F8.1 (float, length 8, 1 decimal); 2X (2 blank spaces); A2 (2 ASCII characters); I6 (integer, length 6)

- DCB Values in nanoseconds (F8.3)
- DCB Value RMS in nanoseconds (F8.3)

All these four correction data files have to be in place to derive satellite orbit and clock data, as well as necessary corrections outlined in chapter 2.

4.2.5 Glonass Constellation Status - Channel Utilization

The Glonass Information and Analysis Center provides information about the current Glonass constellation status, including information on the frequency channel utilization for each satellite on a web page ¹.

The frequency channels are listed in a tabulated way for each orbit plane and slot and are needed to compute the satellite carrier frequency (see Table 2.1).

4.3 Implementation

This section outlines how the software is designed, which software components have been developed and what software modules have been implemented.

The software is developed using the C++14 programming language. The QT 5 application framework is utilized, which provides a convenient way to develop cross-platform applications and is available for both commercial and copy-left open-source licensing (GPL 3.0, LGPL-3.0 or LGPL-2.1).

4.3.1 External Libraries

In general, software libraries are collections of software routines that may be either statically or dynamically linked to a compiled piece of software in the linking process. The inclusion of an external software library, implying that

¹<https://www.glonass-iac.ru/en/CUSGLONASS/getCUSMessage.php>

this software is only used, but has not been developed by the user, might add certain functionality to a program, while lowering the development effort on the other hand. When external libraries are included, the licensing terms have to be investigated in order to avoid unintentional copyright infringements. In this project the following external libraries and frameworks are used:

4.3.1.1 libcurl

The *cURL project*² provides a software library that is capable of transferring data over various internet protocols such as HTTP(S) or FTP(S). The library `libcurl` is implemented in the C programming language and is considered as a true Open Source/Free Software, licensed under a MIT/X derivate license³ that permits commercial use.

The libcurl API is utilized in the `usecurl` wrapper function in the class object for online resources `vonlineresources`. It is used whenever an internet connection to a remote server is established to access and download files, such as SP3 or IONEX data.

4.3.1.2 Qwt

Qwt, or *Qt Widgets for Technical Applications*⁴, is a C++ library that provides graphical user interface widgets for displaying and manipulating graphical data, such as plots. The library usage is subject to the Qwt license version 1.0⁵. In this project, Qwt is used to plot navigation data position in the viewer component of the user interface as well as to inspect the observations.

²<https://curl.haxx.se/>

³<https://curl.haxx.se/docs/copyright.html>

⁴<http://qwt.sf.net>

⁵<http://qwt.sf.net/qwtlicense.html>

4.3.1.3 Eigen

The program makes extensive use of the *Eigen*⁶ C++ template library for linear algebra (version 3.3.3) for vector and matrix computations. Eigen is a header-only library, meaning there is no binary library to link to the application. It's only dependency is the C++ standard library. It is licensed under the Mozilla Public License version 2.0 and therefore suitable to use within this application.

4.3.2 Modular Concept

The program structure is designed with respect to a model-view-controller (MVC) software architectural paradigm, which goes back to the interface paradigm in the smalltalk-80 programming language (cf. Krasner and Pope, 1988). The software is split up into three modules

- a *model* that specifies the data structure and stores data retrieved or computed (see 4.3.4),
- a *controller* that serves as an object that interacts upon user actions and data input, output, and processing (see 4.3.3) and finally
- a *viewer* that presents the state of the current data to the user (see 4.3.6)

This split up of functionality eases the manageability of software components, by a separation of data handling, processing, user interaction, and data representation. If a component needs to be refitted or new functionality is added, this can be done by an adjustment in the respective software component instead of a redevelopment of the overall program.

An example would be a redesign of the underlying data structure without changes in the data representation to the user or vice versa.

⁶<http://eigen.tuxfamily.org/>

4.3.3 Controller Module

As mentioned in the previous section, a controller component is used to manage user interactions with the program. It has to include interfaces that allow users to interact with the program, for instance the import of data or the possibility to initiate data processing and navigational computations.

Figure 4.2 illustrates the main interfaces within the controller class.

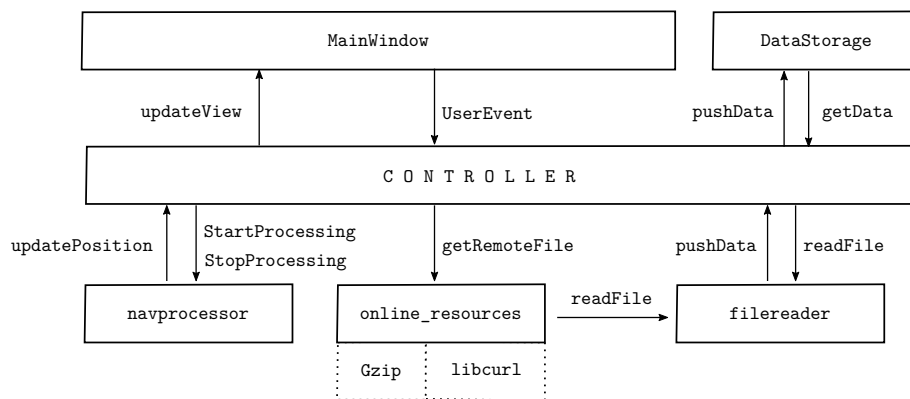


Figure 4.2: Controller interfaces to submodules

When user interaction is triggered within the (graphical) user interface (UI), a `UserEvent` signal is emitted from the *MainWindow* to the controller class. The controller categorizes the event and acts appropriately. In contrast to that, the controller prompts the *MainWindow* to react upon any changes via the `updateView` signal.

The controller provides interfaces to stored data in the *DataStorage* class. Here `pushData` is used to save the data, and `getData` is a method to access the data.

When the user prompts to read data from files, this is handled via the *filereader* class. It is able to read files that include

- precise ephemeris and clock data (SP3),
- global ionosphere maps (IONEX),

- antenna patterns (ANTEX),
- differential code bias data (DCB) and
- Glonass channel utilization files (CUS),

where a path to that file in the file system has to be passed for the reader class to read. It is invoked in the controller class via the `readFile` interface and pushes data through the `pushData` interface of the controller to the *DataStorage*.

While files may be on the file system from former observation periods already, in the case of real-time applications, the system has to be able to acquire data from remote data sources. The *online_resources* class provides interfaces to *libcurl* in order to download files from internet resources. Data downloads are invoked via the `GetRemoteFile` event. If certain files are compressed, they are uncompressed using *Gzip* and then passed to the *filereader* class via `readFile` that reads the files and stores the information in the data storage.

Finally the controller class handles user events that trigger the navigation processor class *navprocessor* to either start or stop computations and receives the `updatePosition` signal, if new position data is available.

4.3.4 DataStorage Module

The data storage module, described in the *DataStorage* class, is the part of the computer program where observation data and auxiliary data is stored. It is directly connected to the *controller* class, which reads and writes data to the data storage utilizing the `getData` and `pushData` interfaces.

The storage is organized using C++ `std::vector` standard containers for data of variable data length, such as satellite observations, and C arrays and C structures prominently used for constant length data.

4.3.5 Navigation Processor Class

The navigation processor class *navprocessor* acts as the fundamental GNSS processing module. The module includes functionality that allows

- to load GNSS observation data from data storage
- to preprocess observation data within a custom `obspreprocessor` class that
 - performs a gross outlier detection in the `detect_outlier` function
 - adds differential code biases (DCBs) to the code observations `add_dcb`
 - has ability to form the geometry-free linear combination `form_gflc`
 - performs a cycle slip detection function `detect_cycle_slip`
- to compute solutions for the user position on an epoch-by-epoch basis
 - using the `process_epoch` to process the current GNSS measurements, setup the design matrices and add atmospheric corrections if available.
- and has the ability to Kalman-filter the trajectory `apply_kalman_filter`

An overview of the process to compute user position is given in figure 4.3.

The GNSS receiver observations are fed into the *ObsdataPreprocessor* class. The preprocessor tries to identify observation outliers comparing the current epoch's observations to previous epochs, by analyzing the standard deviation of the differences. Furthermore, known DCB values are applied to the observations, finally forming the geometric free linear combination used in the cycle slip detection step. The cycle-slip detection methods implemented are described in section 3.2.

In the next step, if no information about the previous state, e.g. receiver position is available, a coarse position estimate is computed using the single point positioning approach within the `process_epoch` method. This coarse estimation is needed as an input for the atmospheric correction functions that are applied later on in the process. In addition, two classes *navdataproducer* and

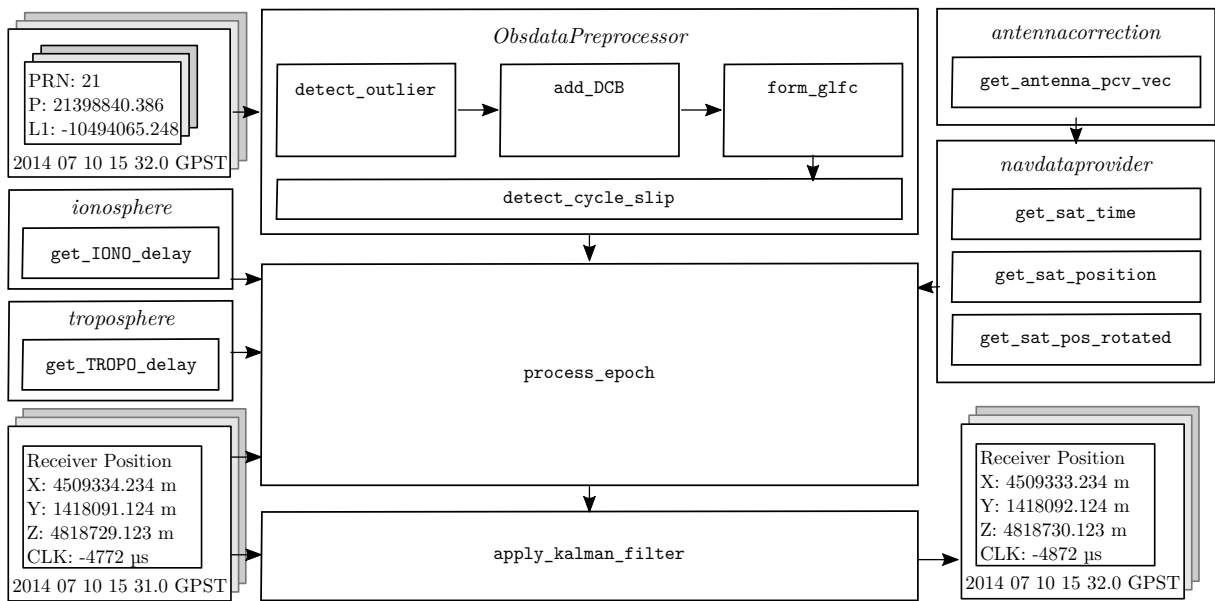


Figure 4.3: Overview of the navigation processor module

antennacorrection come in at this stage to provide the functionality to determine the satellite positions.

The next step is to apply corrections derived from the given atmospheric models. The *troposphere* class includes a method to derive the tropospheric delay. The *ionosphere* class provides an interface to compute the ionospheric delay. Both rely on the knowledge of the users position.

The observations are then passed to the `process_epoch` method, that sets up the design matrix, applies the corrections and computes a receiver state estimate. In kinematic scenarios, the solution is transformed to a local horizon system and filtered utilizing `apply_kalman_filter` using the Kalman filter technique presented in section 3.4.2.

The solutions are pushed to the *DataStorage* module using the `updatePosition` interface to the *controller* class.

4.3.6 Viewer Module

As mentioned before in section 4.3.3, any user interaction with the graphical user interface creates an event that is handed to the controller module entity, which is then obliged to take the appropriate action. One reason why the controller module is not directly integrated in the graphical user interface is that, depending on the platform which the application is meant to be run on, other graphical user interfaces might be present. Desktop applications are usually designed to be controllable via keyboard and mouse, while touch-input is the choice for mobile platforms.

The viewer module that incorporates the graphical user interface developed for this application is constructed to consider cross-platform deployment and aims to minimize the modification effort for alternate platforms.

The viewer module is illustrated in figure 4.4. The controller communicates with the viewer using built-in QT functionality, namely signals and slots. The controller emits the `updateData` signal, which is directed to the `updateData` slot of the viewer module, whereas the viewer emits the `userEvent` signal whenever a user event takes place and the controller needs to update the applications settings or processing tasks.

The viewer object itself consists of one *MainWindow* class object, which is derived from a QT *QMainWindow* class, that represents the main graphical user interface and an additional observation data viewer object of the *Obs-dataViewer* class, which is derived from the QT *QDialog* class.

At application startup, the viewer object is initialized and displaying the *Main-Window* widget. The user is able to rise the following events:

- Load Files to memory `LoadFile`
- Configure program parameters `ConfigureProcessing`
- Download auxiliary files `DownloadFile`
- Start processing of data `StartProcessing`
- Stop processing of data `StopProcessing`

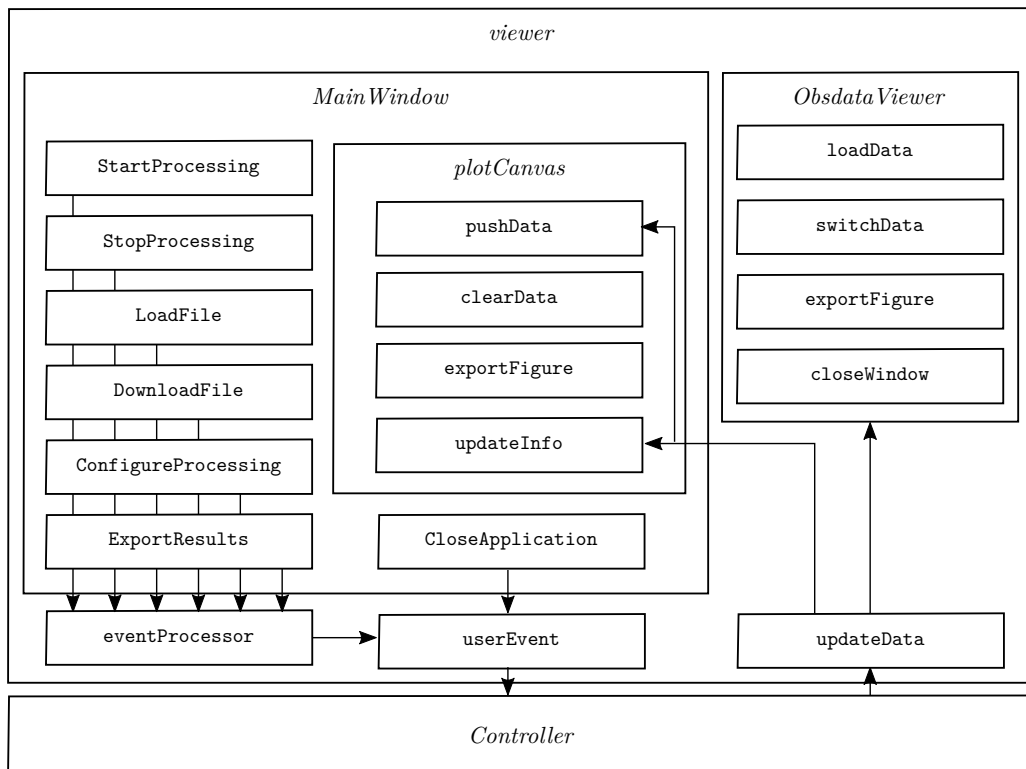


Figure 4.4: Viewer module overview.

- Export results to file `ExportResults`
- Exit the application `CloseApplication`

All these events are modeled with buttons or menu items in the graphical user interface provided by the *Main Window* object.

In addition, the user is presented with a graphical depiction of the current computed position in a *plotCanvas* instance, which is based on the QWT *Qwt-Plot* class. Depending on the `updateData` signal received at the viewer, either the `pushData` function is called to add another data point to the plot widget, or `updateInfo` is executed, resulting in a change of data representation (e.g. connected lines instead of points, or adjusting axis labels or range). Furthermore the application user is able to clear the plot data (`clearData`) or export the figure (`exportFigure`) using the application menu of the main window.

Finally, during development it turned out, that a user might value the possibility to inspect observation data graphically. With an *ObsdataViewer* dialog, which is opened using the [View] entry in the applications menu of the main window, the user is able to analyze all types of observables, from an overview of available satellites, to code and phase observations, and even Doppler data and signal to noise ratio records, depending on the data types available. At first run, observation data is loaded into the dialog using the `loadData` function. The observation type may be switched using the `switchData` function. If the user wants to export a current snapshot of the figure, the `exportFigure` button lets the user choose a destination file, supporting all file format options that QWT offers, either vector graphics (e.g. pdf) or bitmap graphics (e.g. png). Finally, the user might close the observation inspector window by clicking on the close button that executes `closeWindow`, which cleans the objects' memory and dereferences all existing memory pointers.

The main application GUI is displayed in figure 4.5.

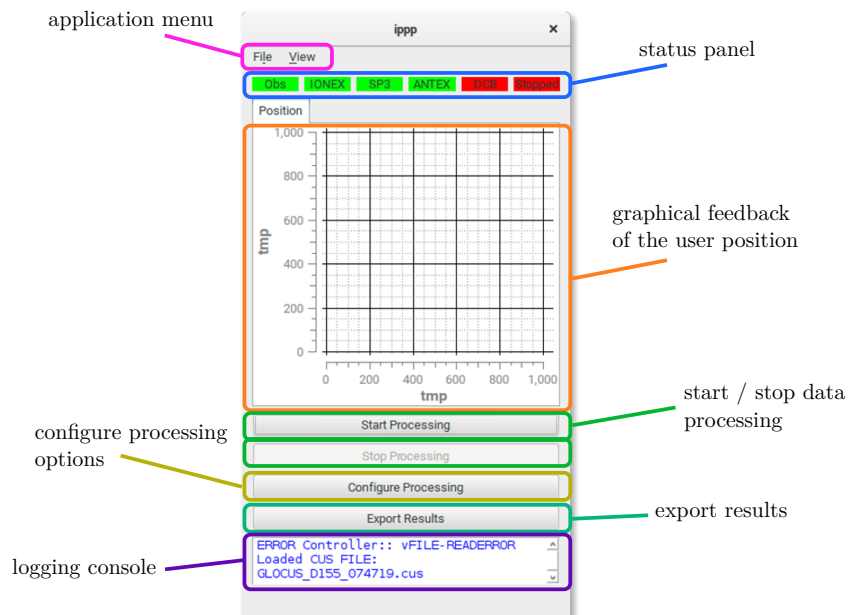


Figure 4.5: Main Window

Two important sections in the main window have not been discussed yet, the status panel and the logging console. The status panel indicates the current state of data sources. In order to start data processing and subsequently compute the user's position, all red labels have to toggle, from an alarming red colour, to green. This is accomplished within the `updateData` function of the viewer module, by keeping track of the current auxiliary data states. Whenever the user tries to start the data processing by clicking on the [Start Processing] button and the status panel indicates that not all auxiliary data is available yet, the user is informed in a popup dialog. Auxiliary data may be loaded via the application menu by choosing [File]→[Open], which opens a file chooser dialog, or downloaded via [File]→[Download]→[Filetype].

The logging console on the other hand keeps track of the application activity and is used to give the user textual feedback. Any operations are logged and error messages are printed to the log. The log is saved automatically to a file in the program's directory when closing the application.

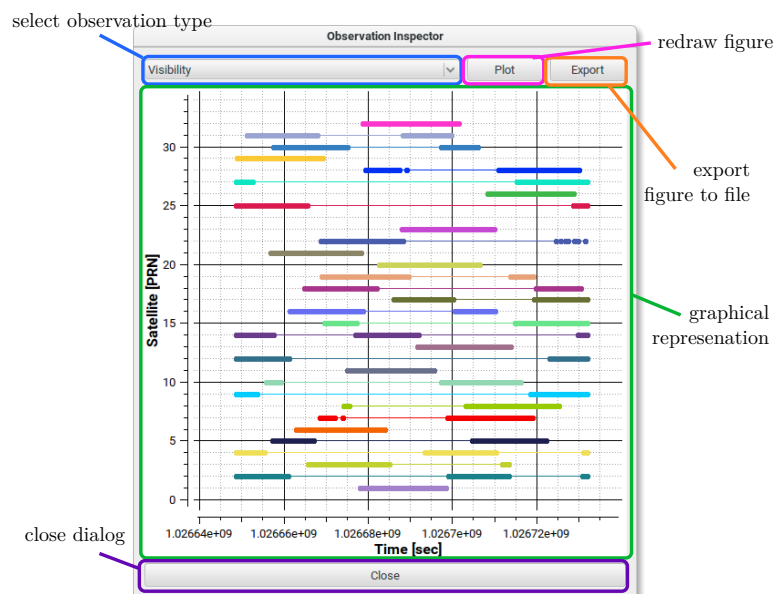


Figure 4.6: Observation data inspector

The observation inspection dialog is shown in figure 4.6. Herein beside pseudo-

range and phase observations, signal-to-noise ratio, as well as general satellite visibility can be displayed, redrawn and an image can be exported for later interpretation.

5 Practical Measurements

This chapter covers a description of the measurement setup, specifies the utilized equipment, and introduces the test environment for static and kinematic tests.

5.1 Measurement Setup

The hardware-platform chosen for both static and kinematic measurements was a combination of a low-cost single-frequency receiver and a low-cost mini computer.

The GNSS receiver system package was purchased from OptimalSystem.de and consisted of

- NVS NV08C-CSM (v3.1) GNSS receiver:
This GNSS receiver measures GPS, GLONASS, Galileo and SBAS signals and is capable of raw-data output in the BINR-format.
- Bluetooth (connectBlue SPP) and USB (FTDI FT230X) interfaces:
The interface is configurable to output either raw-data in the BINR format or NMEA data in plain text format on Bluetooth or USB
- 3600 mAh lithium-polymer battery:
The built-in battery provides an autonomous energy source.

In addition to the receiver package, a Raspberry Pi version 1 model B was used as low-cost mini computer to interface with the receiver, to record, and store the incoming data packages. The software used to interface with the

5 Practical Measurements

NVS package was the *strsvr* program of the RTKLib v2.4.2 GNSS toolkit. The *convbin* program of the same software collection was then used to convert the binary format to the RINEX format (v2.11). Finally auxiliary data was downloaded and moved to the measurement project folder.



(a) Low-cost receiver: NV08C-CSM



(b) Reference receiver: Javad Sigma



(c) Rasperi Pi (Model1-B)



(d) Reference: Javad antenna GrAnt-G3T

Figure 5.1: Overview of the measurement equipment used in testing the software package.

In order to test the system performance, in addition to the low-cost system, a geodetic quality receiver (Javad Sigma, Receiver Board: TRE_G3TH_4) was used to simultaneously capture observation data at 5 Hz data rate. Both, reference receiver and low-cost receiver were connected to a professional grade GNSS L1 antenna (Javad GrAnt-G3T). The hardware used is displayed in figure 5.1. This data was used in combination with data from the local IGS station (GRAZ) to compute a RTK-based solution using RTKLib v2.4.2. The RTK solution serves as reference solution in the evaluation of the PPP solution computed by the developed software package.

5.2 Measurement Scenarios

The measurement scenarios have been chosen to test the system performance in real life urban use-cases. For this purpose two kinematic measurement campaigns were planned. Campaign *A* was measured on April 7th 2016 on the southern rooftop of the local university building (Steyrergasse 30, Graz, Austria), while Campaign *B* was measured on April 11th 2016, including different urban scenarios, from open-field to urban canyon.

- **Scenario A:**

On top of an urban building. Trajectory was planned to include unfavorable signal degradation effects, that is multipath and shadowing.

- **Scenario B:**

B-1: Urban scenario with great satellite visibility and low multipath influence. Measurement took place at a nearby cemetery.

B-2: A mix between urban canyon and free line-of-sight to satellites. This scenario should reflect common urban and suburban positioning situations.

An overview of the locations of the measurement scenarios are given in figure 5.2.

Overview

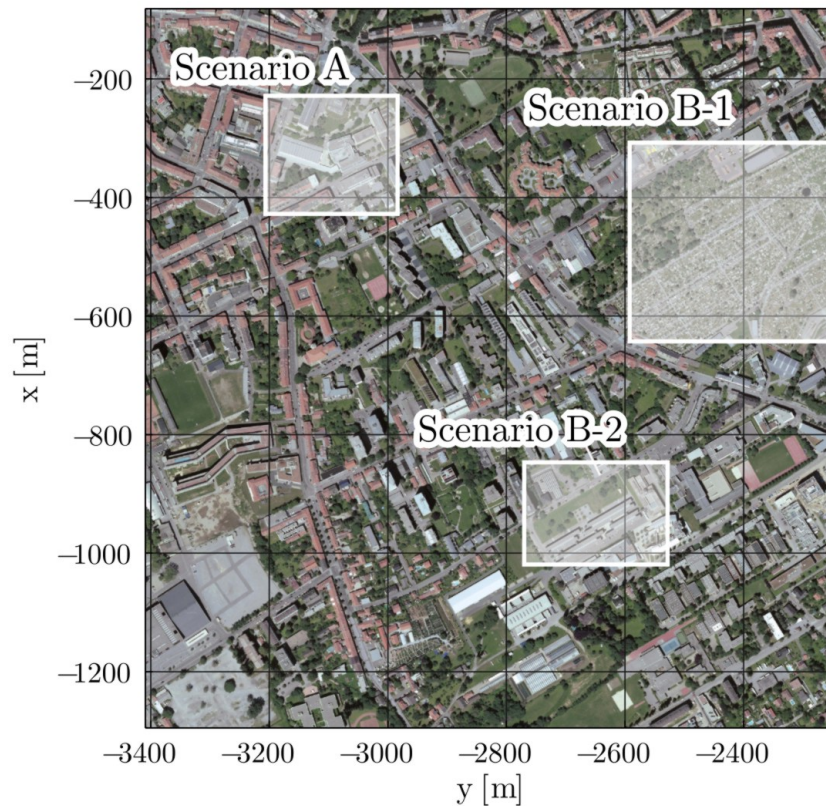


Figure 5.2: Location overview of the measurement scenarios with respect to a local coordinate system, centered at IGS station GRAZ (Source: basemap.at, CC-BY3.0AT)

Because of the common building structure of inner cities, the number of visible satellites is critical, with respect to positioning performance. In a first step, observation periods were chosen, to maximize the number of visible satellites. In addition, an elevation mask of 20° was defined. The observation planning was done using the Trimble Online GNSS Planning tool¹.

In figure 5.3, a detailed view of the test area locations are displayed. Figure 5.3b shows that the buildings south of Steyrergasse 30 may affect the satellite signal, due to obstruction and multipath effect. Figure 5.3c shows the test site

¹Trimble GNSS Planning Tool http://www.trimble.com/gnss_planning_online/

5 Practical Measurements

of scenario B-2, a low-obstruction and low-multi path environment. In figure 5.3d, a more suburban characteristic is tested.

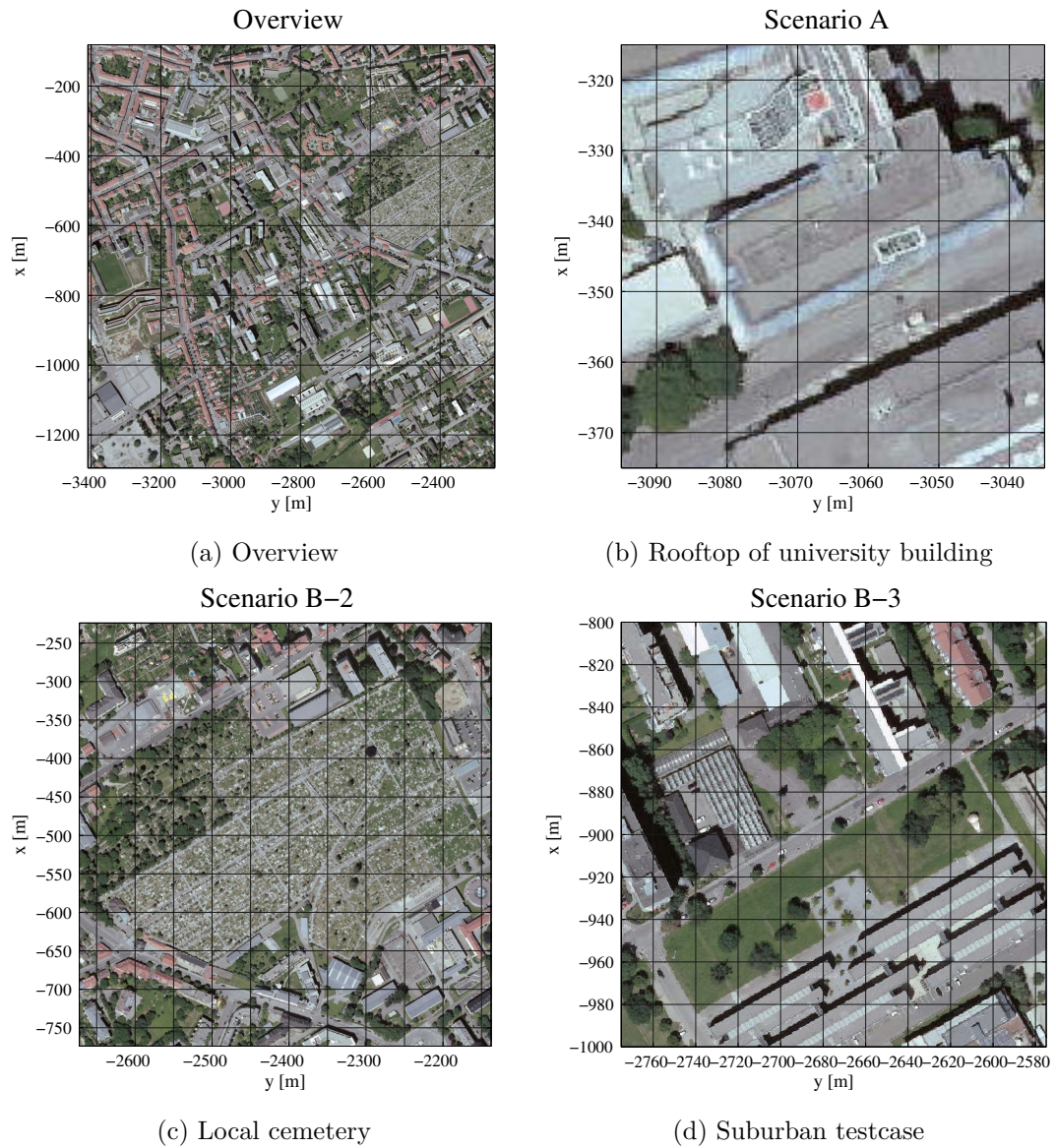


Figure 5.3: Detailed view of the chosen test scenarios. (Source: basemap.at, CC-BY3.0AT)

5.2.1 Measurement Scenario A

In a controlled environment on top of the university building at Steyrergasse 30, several kinematic test cases have been studied.

Figure 5.4a shows a sky plot of the available satellites during the observed time period. Figure 5.4a illustrates the satellite visibility per PRN based on the predicted satellite ephemerides.

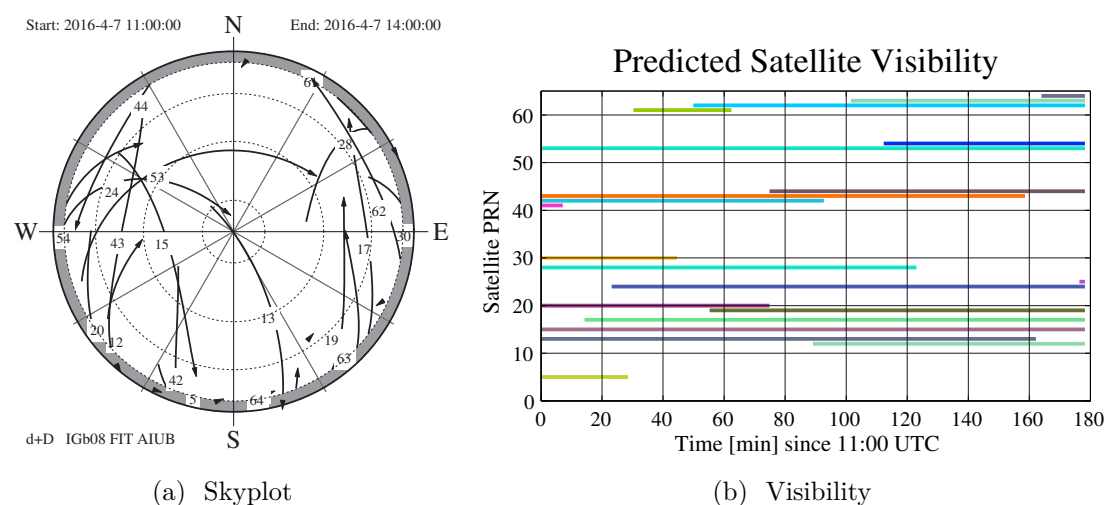


Figure 5.4: Satellite visibility scenario A

Scenario A is aimed to test the filter behavior for different motion situations. The motion scenarios consist of either linear movement, a linear movement preceded by a static period, and a circuit-like motion around a predefined track.

Each simulated motion was repeated, so that the filter behavior could be studied in recurring motion states, e.g. how does the linear-motion model filter react to non-linear motion cases. In non-simulated trajectories this might be used to adjust filter parameters, like the system noise.

The graph of the reference trajectory in figure 5.5 illustrates that:

1. The repeated motion simulation from a start-point to a given end-point (up to 3 times),
2. The stability of the simulated motion, i.e. the observer walked along the trajectory at a constant pace.

The motion types and time periods are listed in table 5.1.

Table 5.1: Motion situation Scenario A — reference time: 11:59:59 UTC

Scenario	Motiontype	Duration [s]
A1	Linear	575
A2	Static+Linear	481
A3	Circuit Motion	479

The reference trajectory, computed using the `rtkLib` software package is shown in figure 5.5. The reference trajectory was processed using three different kinds of ambiguity fixing strategies (cf. Takasu, 2013):

- The Fix-And-Hold strategy, where once the ambiguities are fixed, further processing depends on the fixes in the previous epoch,
- the Instant-Fix strategy, where for each epoch the fix is computed independently, and
- the RTKLib PPP-AR ambiguity resolution method, which is marked "experimental" and used in RTKLib's own PPP module.

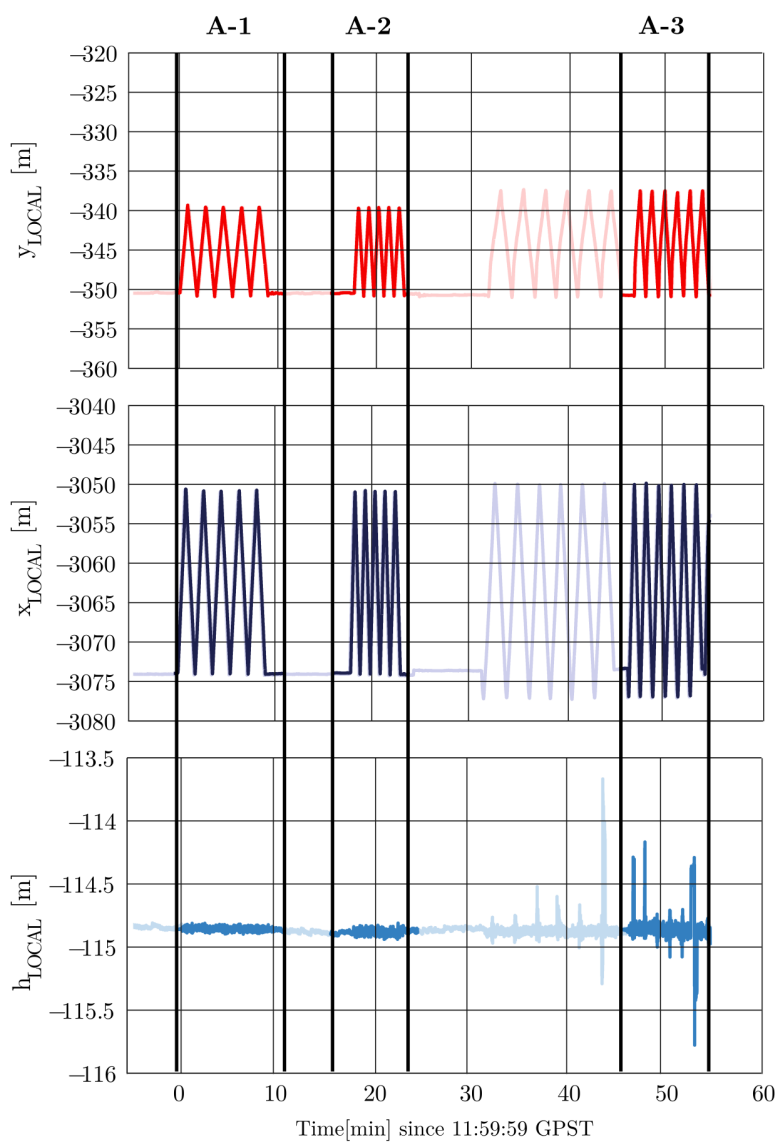


Figure 5.5: Timeseries of reference coordinates (Scenario A).

The quality of the reference trajectory is overall acceptable. The typical deviations are considerably below 50 cm, therefore it is suitable to validate the results computed by the developed PPP software. Deviations between different RTK strategies are illustrated in figure 5.6.

5 Practical Measurements

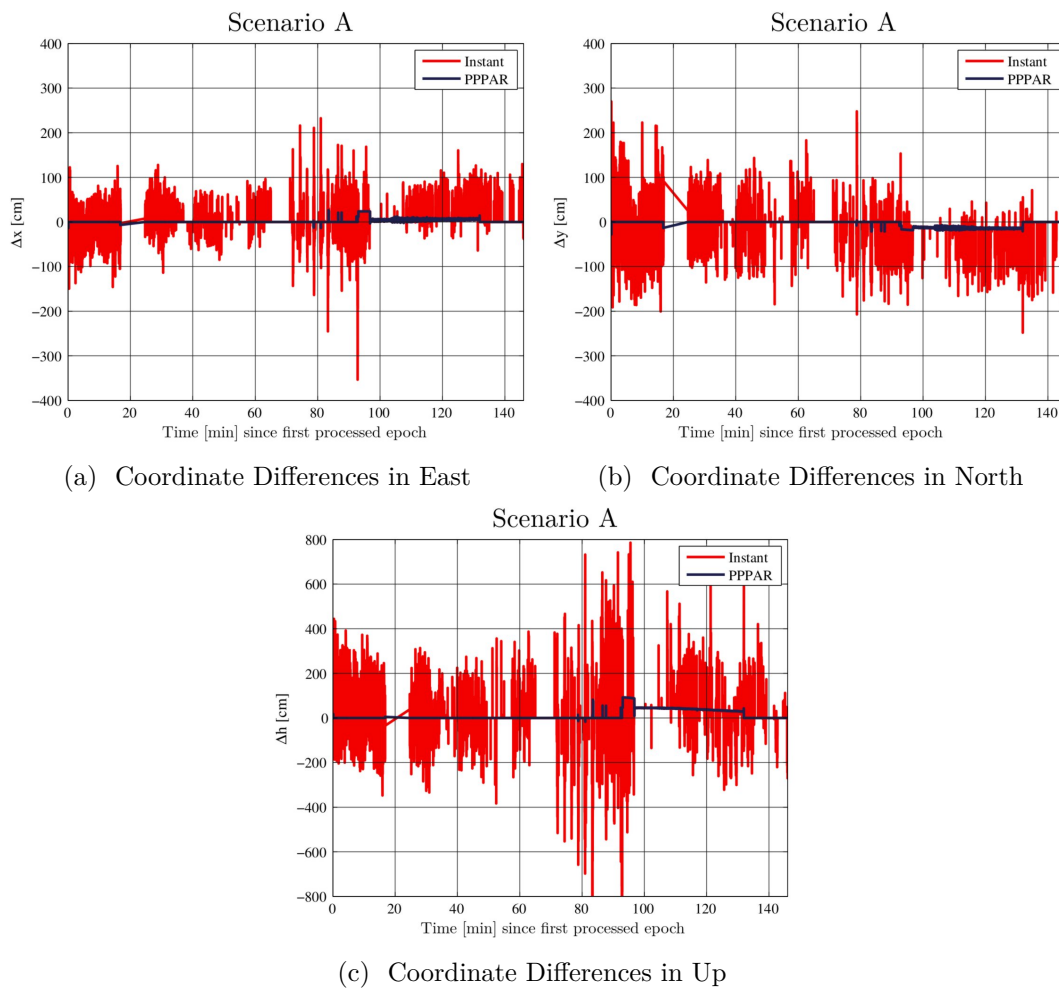
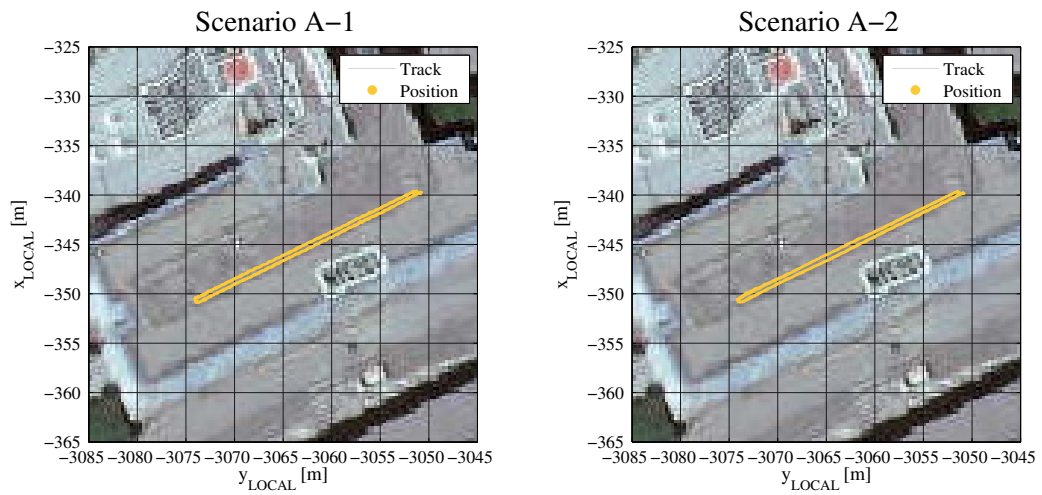


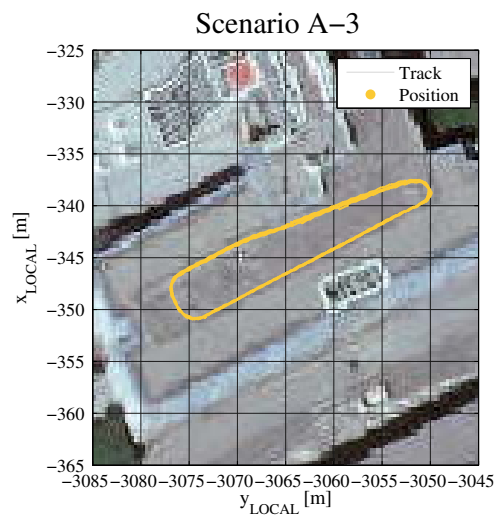
Figure 5.6: Coordinate Differences to Fix-And-Hold reference solution.

An aerial overview of the respective motion situations is given in figure 5.7. The linear motion scenarios are shown in figures 5.7a and 5.7b, while the curved motion (circuit-like shape) scenario is shown in figure 5.7c.

5 Practical Measurements



(a) Groundtrack Scenario A-1 (Reference) (b) Groundtrack Scenario A-2 (Reference)



(c) Groundtrack Scenario A-3 (Reference)

Figure 5.7: Overview of different kinematic motion situations in scenario A (Orthophoto source: basemap.at, CC-BY3.0AT)

5.2.2 Measurement Scenario B

In the second scenario, scenario B, a typical inner city motion situation is tested. For this, a route through different characteristic urban and suburban environments was chosen. The scenario encompasses both a high satellite visibility situation, where no satellite losses should occur simply by moving near taller objects, like building and trees. This scenario is named B-1. The other scenario is a typical urban situation with trees and buildings interrupting satellite reception. This scenario is identified as scenario B-2.

Figure 5.8 gives an overview of the predicted satellite visibility in this measurement scenario.

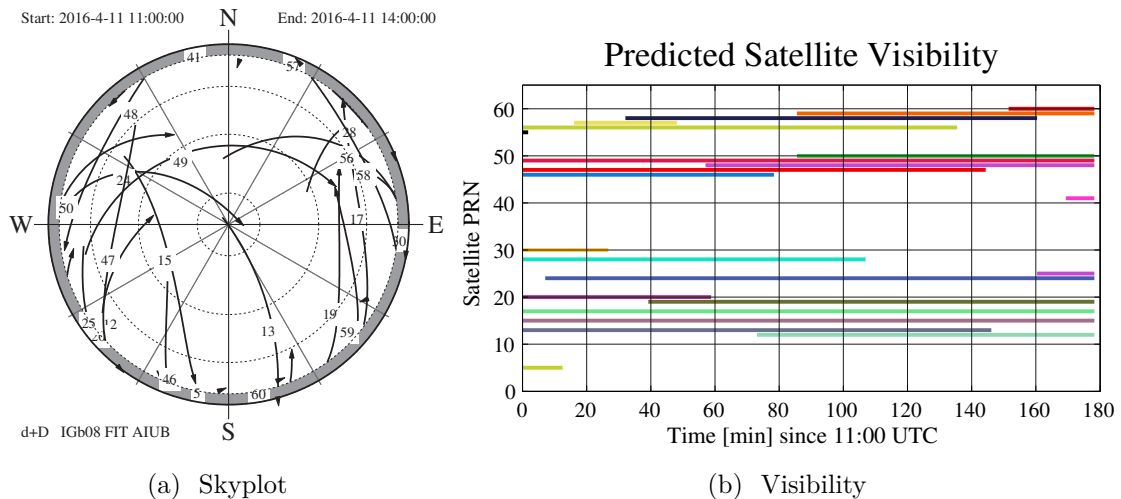


Figure 5.8: Satellite visibility scenario B

Figure 5.9 outlines the characteristics of the reference trajectory. In the first half of the observed measurement period, the reference is within acceptable limits with regards to horizontal position fixes. If the up-component estimate (ellipsoidal height) for consecutive epochs exceeds a threshold of 1 m, the position is linearly interpolated with regards to the neighboring state estimates. The quality of position fixes decreases significantly in the second half and becomes unsuitable after 120 minutes of total observation time. This is due to harsh

5 Practical Measurements

reception conditions at this particular period. The measurements are clearly affected by multi path effects and the position accuracy is lower than a typical SPP solution (i.e. 10 m). Therefore, the reference trajectory is marked invalid for this time period and no validation of the PPP solution is available. The results of the PPP solution is therefore only validated in observation periods, where a valid reference solution is available, hence only within scenario B-1 and B-2.

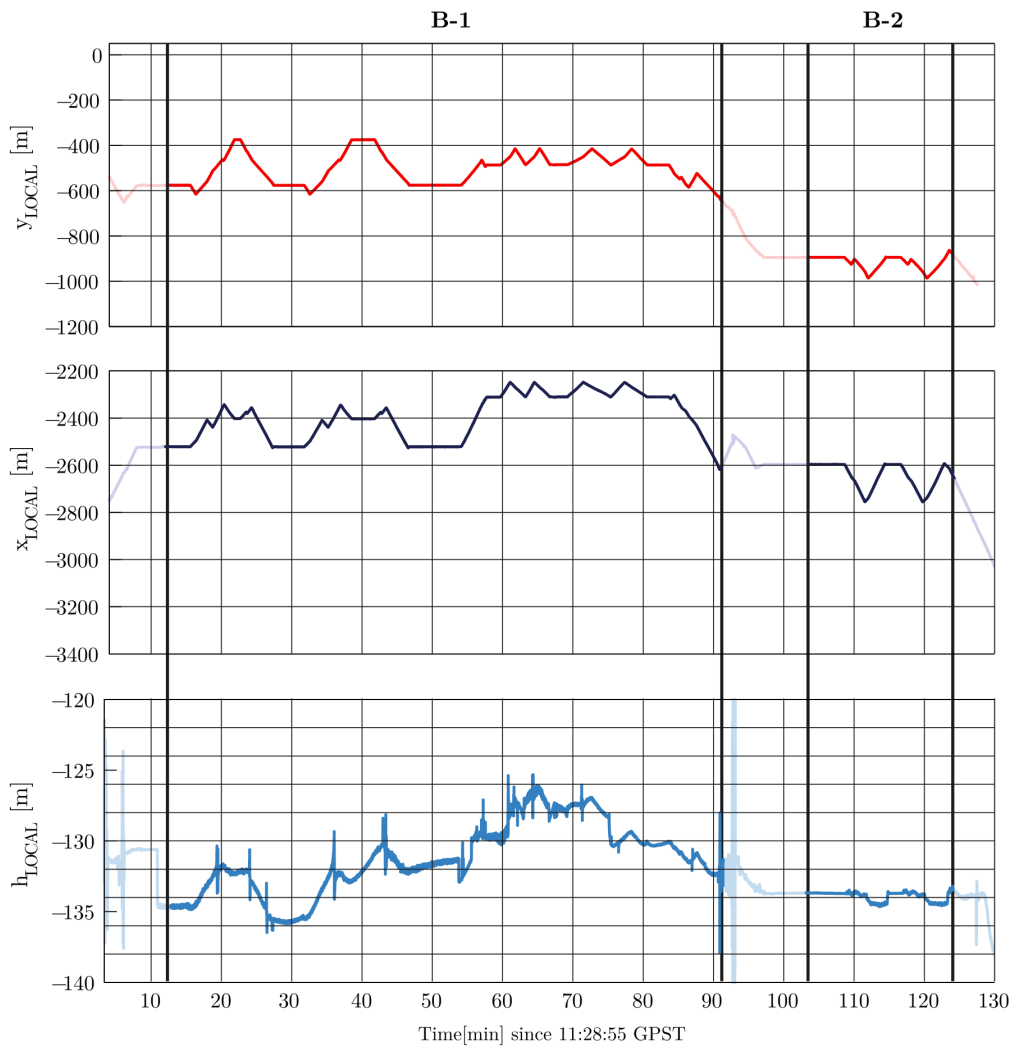


Figure 5.9: Timeseries of reference coordinates (scenario B).

In figure 5.10 the reference trajectories for the test scenarios B-1 and B-2 are displayed. Although the overall reception environment in scenario B-1 was expected to perform better than scenario B-2, yet the computed reference trajectory contains more float-only estimates than scenario B-1. The reason for this might be, that neighboring buildings degraded the received signal and therefore the software was not able to fix the ambiguities correctly. On the other hand, the position estimates in scenario B-2 are based on a Fix-and-Hold ambiguity solution only.

The expected position accuracy of the PPP solution is in the lower-meter range, therefore both reference trajectories meet the criteria to perform as validation on the computed results.

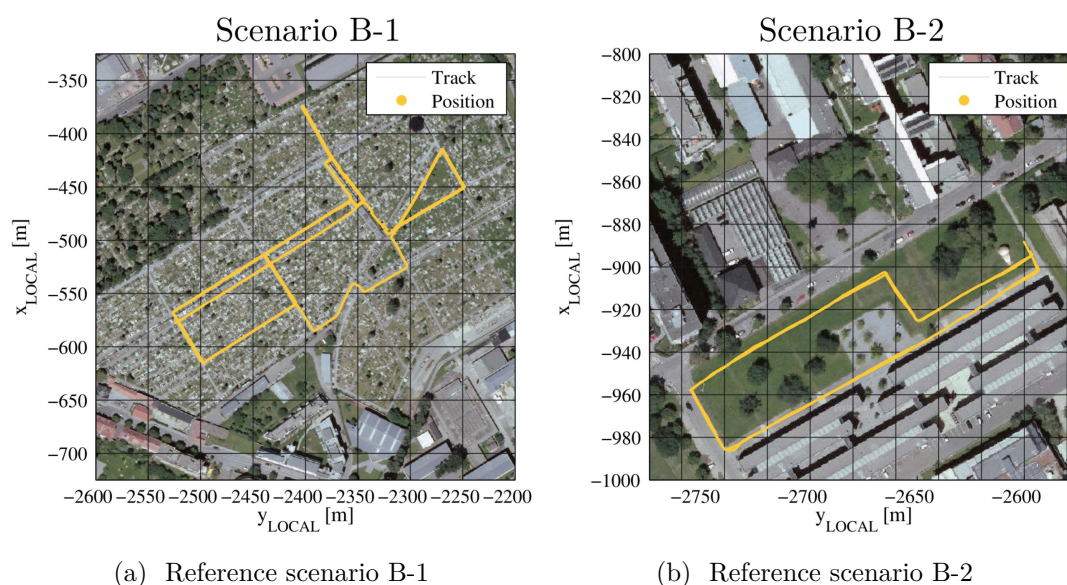


Figure 5.10: Groundtrack of scenario B-1 and B-2 (Orthophoto source: basemap.at, CC-BY3.0AT)

6 Performance Evaluation

In this chapter, the results of the processed datasets, collected in the previously discussed chapter, are presented and discussed.

6.1 Scenario A

This measurement scenario evaluates the system performance in different kinematic situation, namely a pedestrian walking either along a straight line, or moving in a circuit-like motion pattern.

6.1.1 Scenario A-1

In this scenario, the receiver is moving along a linear track at a constant speed of around 0.3 m/s from one marked position to a location on the opposite side of the roof top, then turning around and moving back again. The receiver antenna is mounted on a custom mount of a rucksack.

In this first scenario, the user's motion situation is kinematic at all time. Furthermore, the software package is configured to compute a filtered trajectory based on the PPP solution and a linear kinematic motion model. A visual comparison of the ground track for both reference data and the PPP solution is given in figure 6.1.

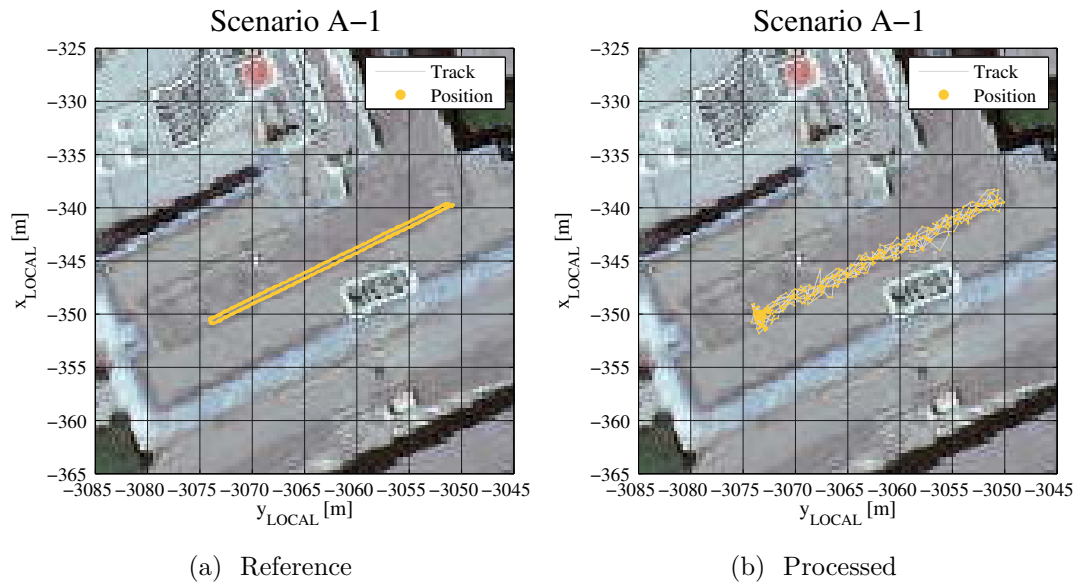


Figure 6.1: Groundtrack comparison scenario A1 (Orthophoto source: basemap.at, CC-BY3.0AT)

As expected, the PPP trajectory is noisier than the RTK solution. Therefore the two distinct tracks (back and forward) are not distinguishable. The root-mean-square (RMS) of the difference vector (3-dimensional) between the RTK and PPP solution is 3.53 m, while the RMS of the horizontal displacement is 0.93 m, and as low as 0.62 m for the east- and 0.68 m for the north-component. Hence most of the total deviation is attributed to the up-component.

A time series of coordinate differences between PPP and reference solution is shown in figure 6.2.

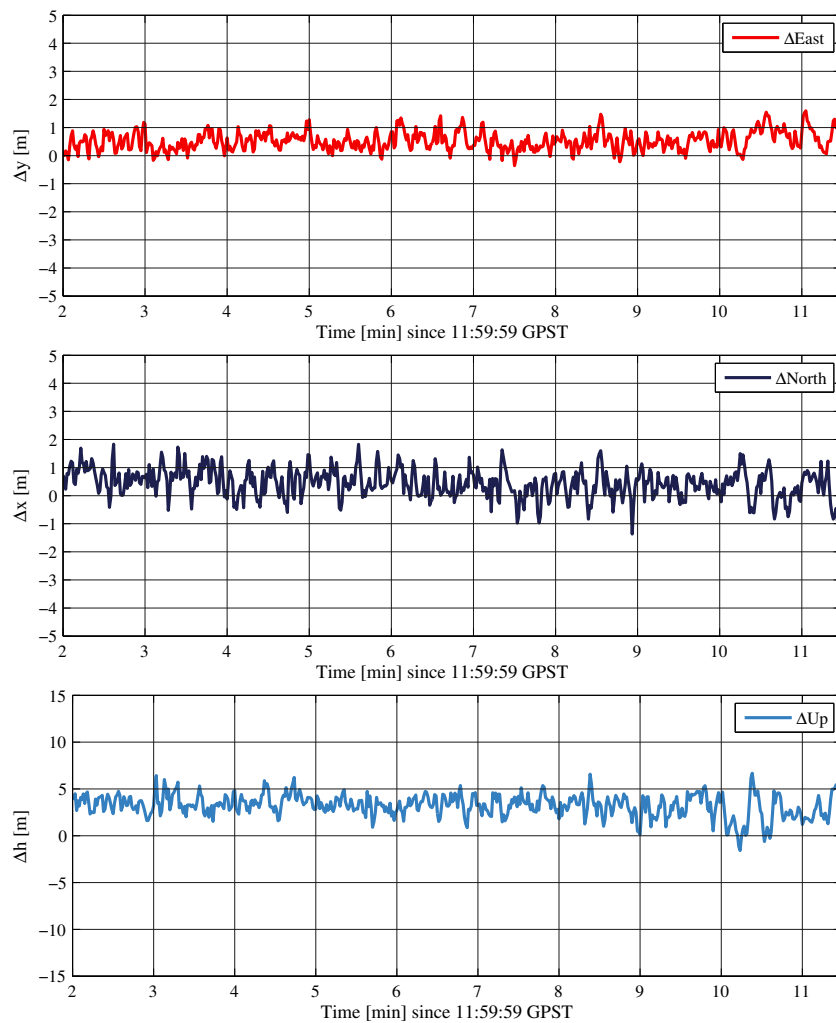


Figure 6.2: Scenario A1: Coordinate difference relative to reference trajectory

6.1.2 Scenario A-2

In scenario A-2, the receiver moves along the same trajectory as featured in the A-1 scenario. In this scenario, the user decides, whether the current motion situation is static or kinematic. While in a real-time application, the user might use the respective features in the application GUI, in a post-processing case, the user might define static and kinematic periods in the configuration file. The static period in scenario A-2 was defined from 12:16:10 to 12:18:15 (GPST).

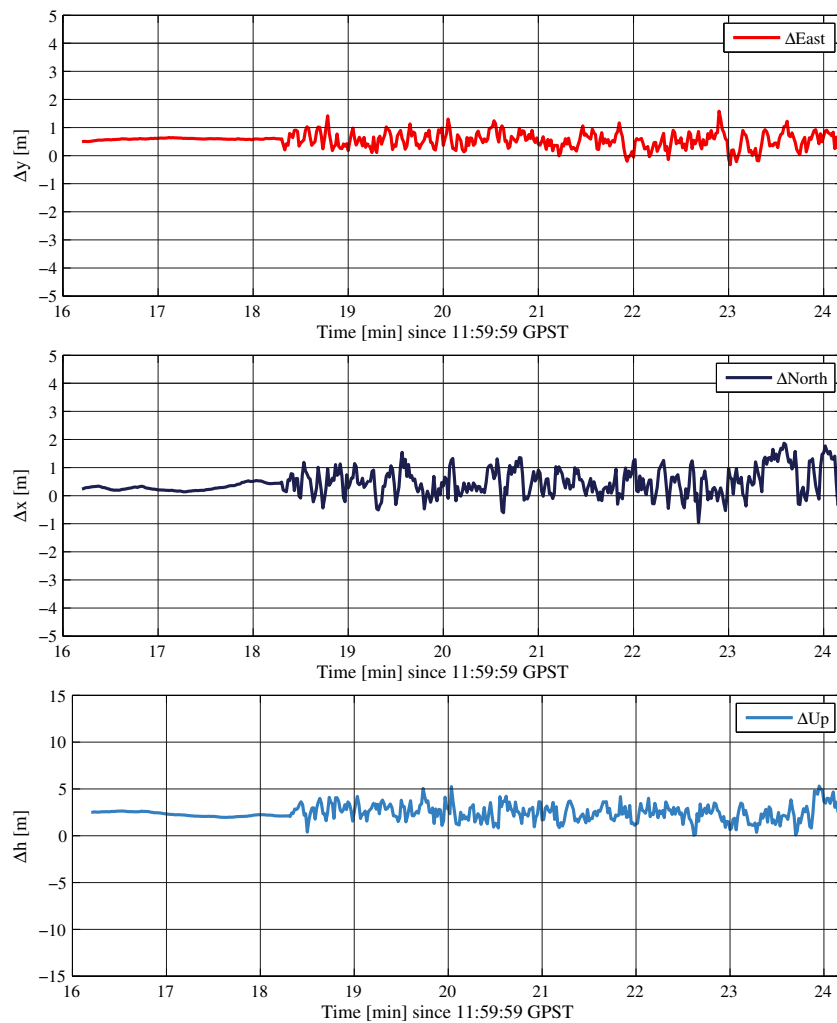


Figure 6.4: Scenario A2: Coordinate difference relative to reference

6.1.3 Scenario A-3

In the third measurement dataset, the trajectory was modified slightly to reflect a more common scenario, where a user might walk along a circuit-like path. The user is again moving in a kinematic-only motion situation (Scenario A-1).

In addition, the receiver moves very close to a wall (North=-340 m, East=-3065 m), which leads to a degradation of the estimated position, due to a loss in satellite

signals.

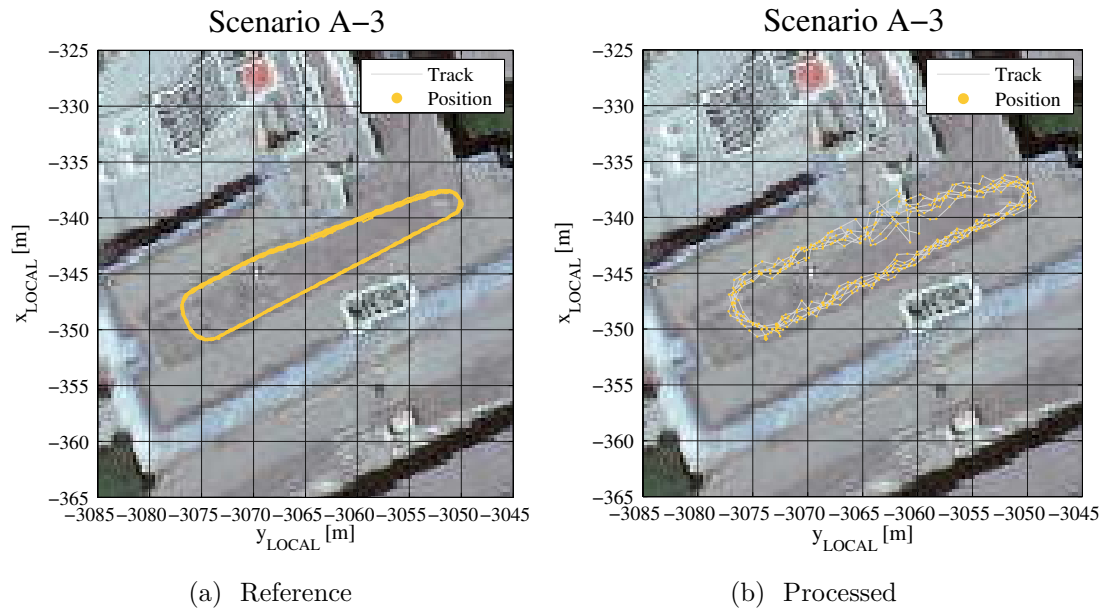


Figure 6.5: Groundtrack comparison scenario A3 (Orthophoto source: basemap.at, CC-BY3.0AT)

The kinematic position quality is comparable to the previous scenarios. Although, in contrast to the previous scenarios, the RMS in north- (0.96 m) is about twice as high as the RMS in east-direction (0.45 m). While the RMS of the 3-dimensional displacement accounts to 1.92 m. The most dominant deviations to the reference trajectory are next to the building structure, leading to prominent peaks in the time series and a decreased RMS in north-direction (cf. figure 6.6).

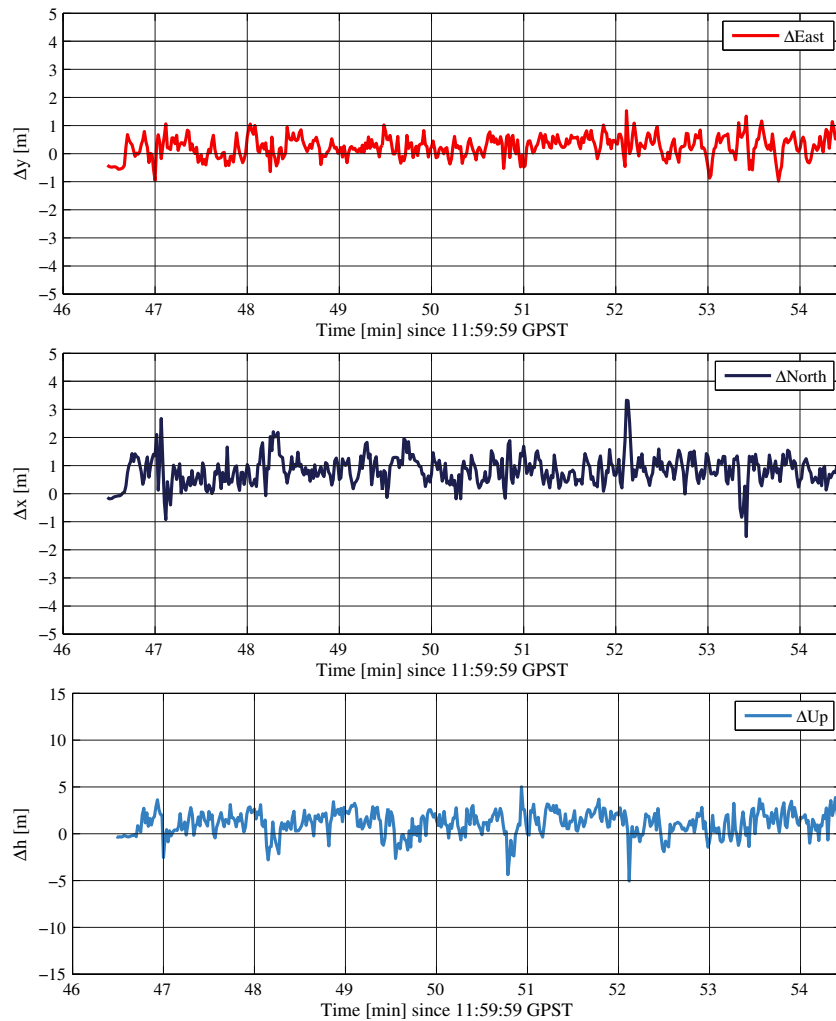


Figure 6.6: Scenario A3: Coordinate difference relative to reference

6.2 Scenario B

This measurement scenarios evaluates the positioning capability of the software package in typical urban and suburban situations. In addition, the number of measured epochs is significantly higher than in the previous scenarios.

6.2.1 Scenario B-1

In scenario B-1, the receiver's motion is moving along a street-like pattern in a local cemetery. The trajectory consists of sharp geometric structures, which is helpful to reproduce motion patterns. A ground track comparison between reference and estimated PPP positions is given in figure 6.7.

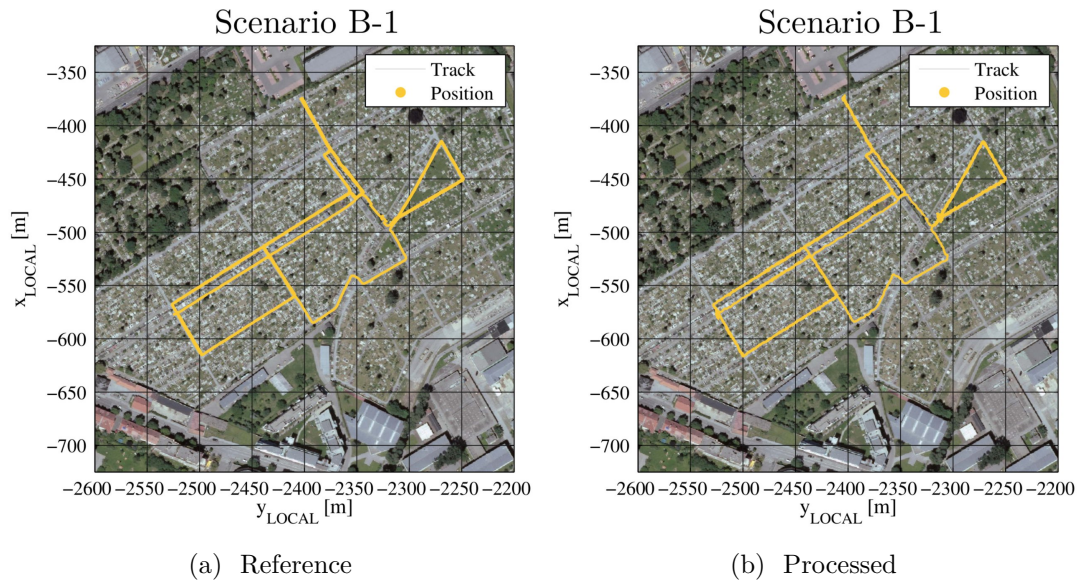


Figure 6.7: Groundtrack comparison scenario B1 (Orthophoto source: basemap.at, CC-BY3.0AT)

Figure 6.8 shows the coordinate differences in a time series. The most dominant features in the time series are at minute 13, where the east-component offset to the reference solution suddenly drops down to around -3 m and keeps at this offset until the end of this scenario. It is likely that the fix-and-hold reference solution, which is used as reference trajectory in this scenario, is the reason for this behavior. Other prominent features are at minute 33 and 70. The reason for these jumps is due to loss of lock on satellites, induced by the user (shadowing).

The overall quality of the PPP solution is still acceptable: with a RMS of

1.82 m in east-, and 0.92 m in the north component, while the 3d-displacement RMS equals 5.72 m.

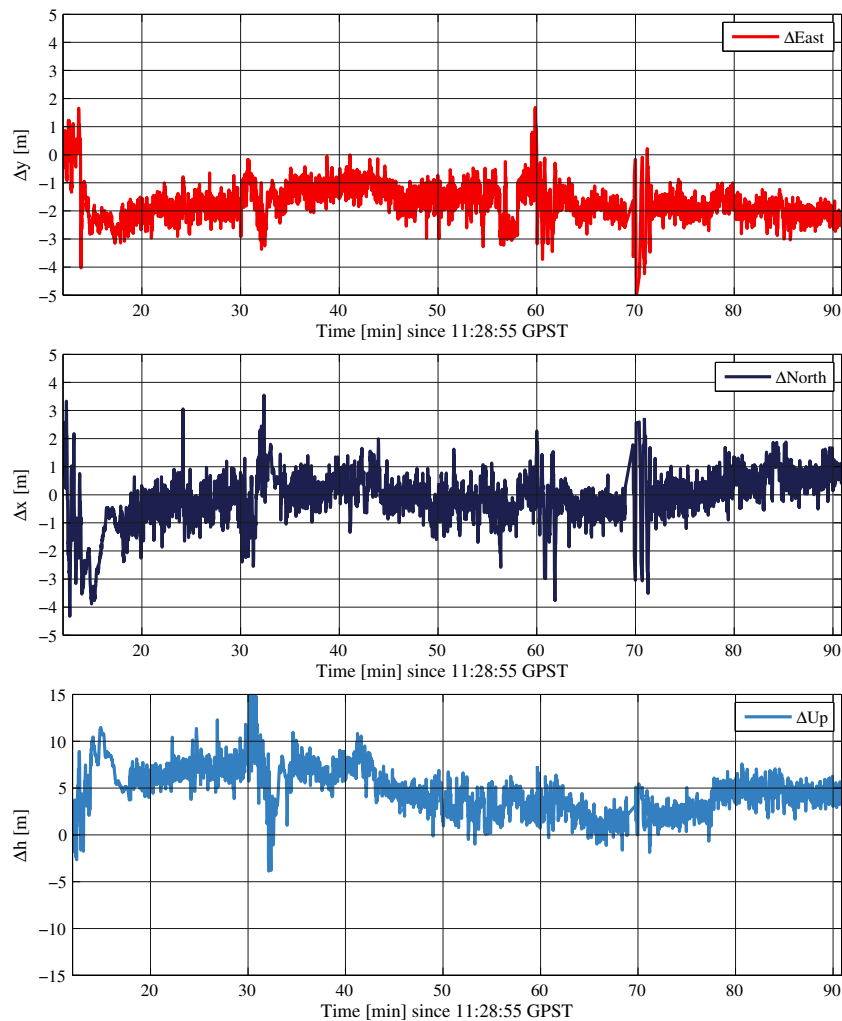


Figure 6.8: Scenario B1: Coordinate difference relative to reference

6.2.2 Scenario B-2

Measurement scenario B-2 highlights typical motion patterns of pedestrian users. The most dominant feature in this location is the building complex south

of the trajectory. This situation should test the robustness of the solution with regards to shadowing effects.

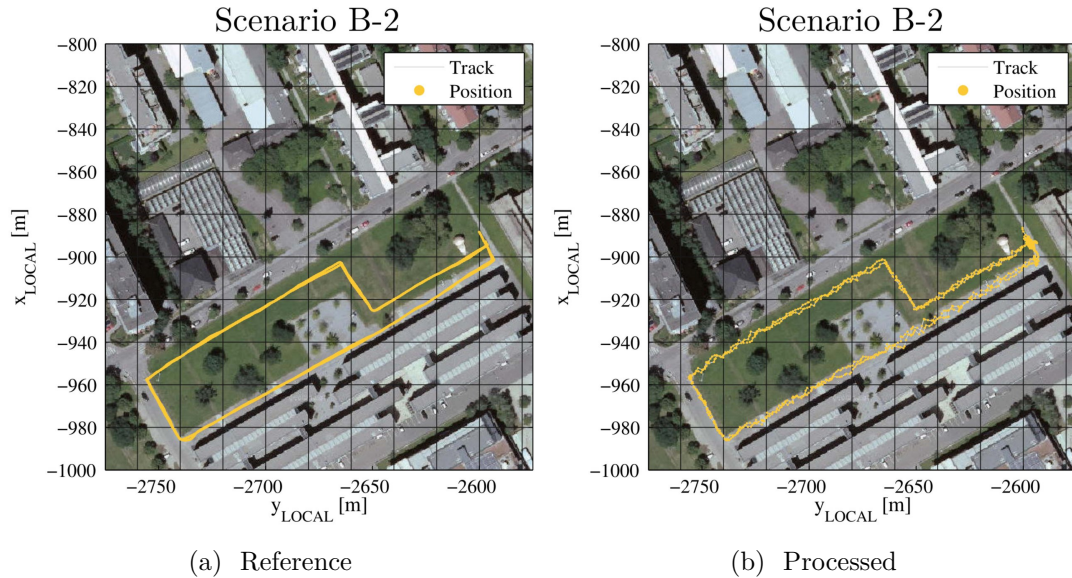


Figure 6.9: Groundtrack comparison scenario B2 (Orthophoto source: basemap.at, CC-BY3.0AT)

In this scenario, the motion situation changes between static and kinematic. The time series of the coordinate differences is shown in figure 6.10.

The positioning accuracy in the first static phase is comparable to test scenario A2. In the kinematic phases, minute 111 to 117, both east and up- coordinates are comparable to previous motion situations, but the before mentioned building structures influence the quality of the north-component, due to loss of satellites and degraded geometry. These effects are still visible in the second kinematic phase, but are compensated before the next kinematic phase starts (minute 119).

The influence of satellite loss are again visible in the second loop (minute 119 to 125). Again the north-component is severely influenced due to changes in satellite geometry.

6 Performance Evaluation

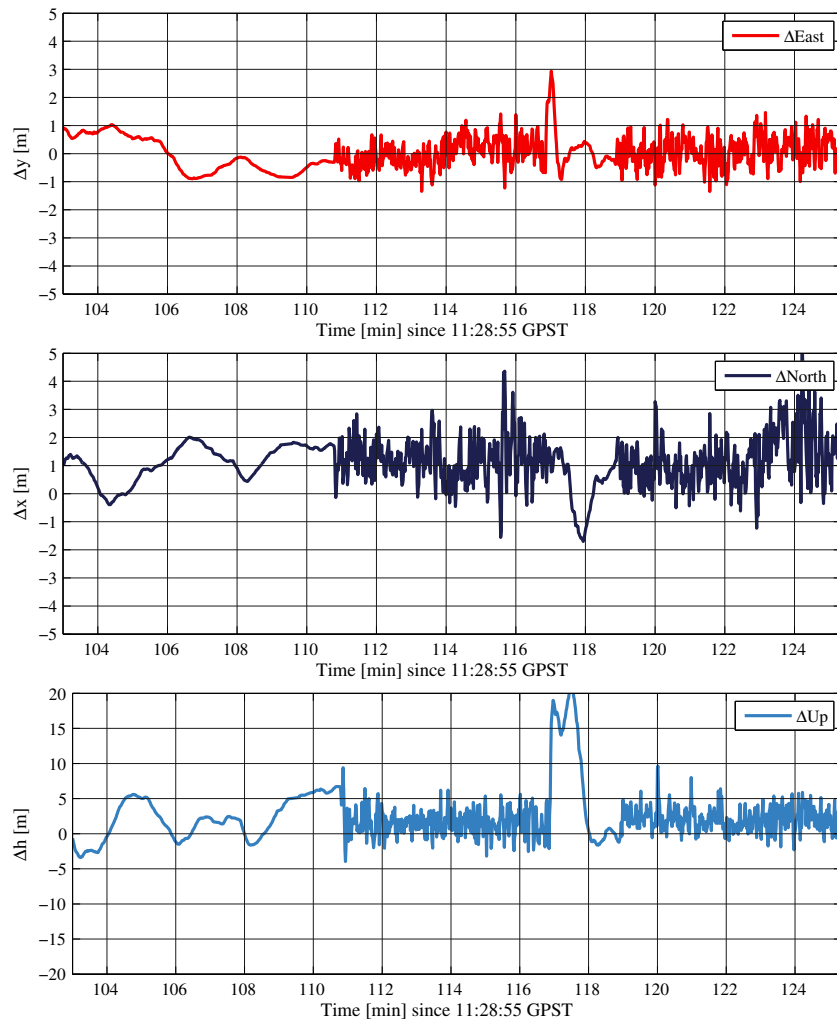


Figure 6.10: Scenario B2: Coordinate difference relative to reference

7 Outlook and Resumee

In the previous chapters, a PPP package was presented, implemented and tested, which has shown to be superior to single point positioning methods widely used in todays mobile receiver platforms, e.g. smart phones. The developed software package achieved acceptable accuracy levels, i.e. suitable for pedestrian navigation purposes.

7.1 Summary of the Results

A summary of the positioning quality of the developed software package is shown in table 7.1.

The horizontal accuracy (measured against reference) is in the low meter range and therefore suitable for most navigational use cases. The overall robustness measured against the reference is impacted by the loss of satellite visibility (e.g. loss of lock) as shown in the real-life measurement scenarios B-1 and B-2. This leads to outliers in horizontal and vertical position fixes in the range of several meters. Therefore, especially for life-critical solutions, a more refined and robust state estimation approach might be chosen, e.g. a tightly coupled Kalman filter integration of inertial measurements and GNSS observations.

Table 7.1: Quality properties of the presented solution

	Epochs [s]	RMS _{East}	RMS _{North}	RMS _{Up}	RMS _{3D}	95% Quantile _{2D}	95% Quantile _{3D}
	[s]	[m]	[m]	[m]	[m]	[m]	[m]
A1	575	0.62	0.68	3.41	3.53	1.56	4.95
A2	481	0.61	0.64	2.55	2.70	1.50	3.76
A3	479	0.45	0.97	1.60	1.92	1.65	2.97
B1	4675	1.82	0.92	5.34	5.72	3.06	8.93
B2	1307	0.58	1.37	4.38	4.63	2.52	6.92

7.2 Future Developments

Today GNSS products are being incorporated in more and more devices: ranging from intelligent homes and the "internet of things" (IoT) to mobile platforms in smartphones and professional or leisure use-cases and activities, in either the land-based, the maritime or the aeronautical regime.

While most GNSS products today rely solely on SPP solutions, there is a need for precise position and velocity estimation. The most prominent example might be the use of personal drones or even service robots, that interact with their users. In both cases the robust estimation of the object's state is highly important with respect to general and personal safety of either the public or the individual users (cf. Kouba and Héroux, 2001).

To achieve high availability, increase reliability and enable integrity monitoring in navigation systems, commercial platforms incorporate a wide range of independent sensor systems. These might consist of low-cost inertial measurement units, barometers, magnetometers and optical systems, but for perfect absolute location tracking, GNSS is still the decisive factor with regards to positioning performance.

While real-time kinematics (RTK) is still the choice for precise applications below the decimeter level, an auxiliary, continuous, high-speed data stream to transfer (virtual) base station data is not applicable in every use-case scenario. In addition, RTK over-the-air services are prone to tampering in the messaging

channel, which leaves end-users to use their own base-station, if security aspects are of concern (cf. Tippenhauer et al., 2011).

For such use-case scenarios, PPP, which in its nature does not rely on continuous external data, provided by others, is preferable. Even in scenarios, where a continuous data stream cannot be guaranteed or the amount of mobile data would be limited (e.g. cost aspect), a concurrent PPP processing stack could increase the availability of precise navigation trajectories.

This master thesis has outlined the methods and techniques used in single-frequency PPP. The software package developed incorporates features designed for single-frequency processing on low-cost and low-computational power platforms.

To advance the positioning capabilities even more, a multi-frequency receiver approach is desirable. The use of the ionosphere linear combination for phase observations would further reduce the influence of the ionosphere and therefore increase the position accuracy. In addition, the use of the Melbourne-Wübbena linear combination (cf. Melbourne, 1985 and Wübbena, 1985) is a standard tool for cycle-slip detection in multi-frequency environments, improving slip detection by enlarging the virtual wavelength of the combined signal and therefore detect jumps in the signal at lower levels.

While low-cost multi-frequency receivers are not common in typical navigational use-cases, with the development of software-based receivers using low-cost radio frequency back ends and the increase in computational power in modern multi-core processing units, even in low-cost platforms like smart phones, there is a future for low-cost multi-frequency GNSS.

Appendix

Bibliography

- Collins, John Paul (1999). ‘Assessment and Development of a Tropospheric Delay Model for Aircraft Users of the Global Positioning System’. PhD thesis (cit. on p. 29).
- Dach, Rolf et al. (2007). ‘Manual of Bernese GPS Software Version 5.0’. In: *Astronomical Institute, University of Bern* (cit. on p. 39).
- Decker, B. Louis (1986). ‘World Geodetic System 1984’. In: *Fourth International Geodetic Symposium on Satellite Positioning; The University of Texas at Austin; Austin Texas; 28 April 1986 – 2 May 1986* (cit. on p. 18).
- Demtröder, Wolfgang (2013). *Experimentalphysik 1: Mechanik und Wärme*. 6th ed. Springer Spektrum. isbn: 978-3-642-25465-9 (cit. on p. 22).
- Dominici, Pietro (1998). ‘My first fifty years in ionospheric research’. In: *Annali di Geofisica* 41.5-6, pp. 857–883 (cit. on p. 21).
- Elizei, Mohamad Mahdi Alizadeh (2013). ‘Multi-Dimensional modeling of the ionospheric parameters, using space geodetic techniques’. published in *Geowissenschaftliche Mitteilungen, Heft Nr. 93*. PhD thesis. Gußhausstraße 27-29, 1040 Vienna, Austria: Vienna University of Technology, Departments für Geodäsie und Geoinformation (cit. on p. 21).
- Galileo OS SIS ICD (2010). *European GNSS (Galileo) Open Server, Signal in Space Interface Control Document* (cit. on pp. 7, 8, 20).
- GLONASS ICD (2008). *Interface Control Document, Navigational radiosignal in bands L1, L2, ed. 5.1*, (cit. on pp. 7–9, 18, 19).

- Goad, C and L Goodman (1974). ‘Modified Hopfield Tropospheric Refraction Correction Model’. In: *Transactions-American Geophysical Union*. Vol. 55. 12. American Geophysical Union 2000 Florida Ave. NW, Washington, DC 20009, pp. 1106–1106 (cit. on p. 29).
- Gordon, Richard G (1991). ‘No-net-rotation model of current plate velocities incorporating plate motion model NUVEL-1’. In: *Geophysical research letters* 18, pp. 2039–2042 (cit. on p. 16).
- Hammer, E. (1897). *Lehrbuch der ebenen und sphärischen Trigonometrie*. 2nd ed. Zum Gebrauch beim Selbstunterricht und in Schulen besonders als Vorbereitung auf Geodäsie und sphärische Astronomie. Stuttgart: J. B. Metzlerscher Verlag (cit. on p. 27).
- Han, Chunhao, Yuanxi Yang, and Zhiwu Cai (2011). ‘BeiDou navigation satellite system and its time scales’. In: *Metrologia* 48.4, S213 (cit. on p. 20).
- Herring, T.A. (1992). ‘Modeling Atmospheric Delays in the Analysis of Space Geodetic Data’. In: *Refractions in transatmospheric signals in geodesy*. Vol. 7. 2, pp. 157–164 (cit. on p. 32).
- Hilla, Steve (2010). ‘The Extended Standard Product 3 Orbit Format (SP3-c)’. In: *IGS website: <https://igscb.jpl.nasa.gov/igscb/data/format/sp3c.txt>* (cit. on p. 53).
- Hofmann-Wellenhof, Bernhard, Klaus Legat, and Manfred Wieser (2011). *Navigation: principles of positioning and guidance*. Springer Science & Business Media (cit. on pp. 46, 47).
- Hofmann-Wellenhof, Bernhard, Herbert Lichtenegger, and Elmar Wasle (2008). *GNSS–Global Navigation Satellite Systems: GPS, GLONASS, Galileo & more*. SpringerWienNewYork. isbn: 978-3-211-73012-6 (cit. on pp. 9, 10, 22, 23, 28, 30, 35).
- Hopfield, H.S. (1969). ‘Two-quartic tropospheric refractivity profile for correcting satellite data’. In: *Journal of Geophysical research* 74.18, pp. 4487–4499 (cit. on pp. 28–30).
- Interface Control Working Group (2013). *Interface Specification - IS-GPS-200 - Navstar GPS Space Segment/Navigation User Interface*. Tech. rep. (cit. on pp. 7, 8, 19).

- Kalman, R.E. and R.S. Bucy (1961). ‘New Results in Linear Filtering and Prediction Theory’. In: *Journal of Basic Engineering*, pp. 95–108 (cit. on p. 46).
- Kouba, Jan and Pierre Héroux (2001). ‘Precise point positioning using IGS orbit and clock products’. In: *GPS solutions* 5.2, pp. 12–28 (cit. on p. 96).
- Krasner, Glenn E, Stephen T Pope, et al. (1988). ‘A description of the model-view-controller user interface paradigm in the smalltalk-80 system’. In: *Journal of object oriented programming* 1.3, pp. 26–49 (cit. on p. 61).
- Marini, John W. (1972). ‘Correction of satellite tracking data for an arbitrary tropospheric profile’. In: *Radio Science* 7.2, pp. 223–231 (cit. on p. 32).
- Melbourne, William G (1985). ‘The case for ranging in GPS-based geodetic systems’. In: *Proceedings of the first international symposium on precise positioning with the Global Positioning System*. Vol. 1519 (cit. on p. 97).
- Mueller, Ivan I. (2000). ‘The First Decade of the IERS’. In: *ASP Conference Series*. Vol. 208. Polar Motion: Historical and Scientific Problems. Department of Civil, Environmental Engineering, and Geodetic Science, The Ohio State University Columbus. OH 43210-1275, pp. 200–213 (cit. on p. 15).
- National Geospatial-Intelligence Agency (2014). *Standardization Document, World Geodetic System 1984 - its Definition and Relationships with Local Geodetic Systems*. Department of Defense (cit. on pp. 18, 19).
- Niell, AE (1996). ‘Global mapping functions for the atmosphere delay at radio wavelengths’. In: *Journal of Geophysical Research: Solid Earth (1978–2012)* 101.B2, pp. 3227–3246 (cit. on pp. 29, 32, 33).
- Petit, Gérard and Brian Luzum, eds. (2010). *IERS Conventions (2010)*. Technical Note No. 36. IERS Conventions Centre, International Earth Rotation and Reference Systems Service (IERS) (cit. on pp. 16, 35, 36).
- Remondi, Benjamin W (1984). ‘Using the global positioning system(GPS) phase observable for relative geodesy: Modeling, processing, and results[Ph. D. Thesis]’. In: (cit. on p. 31).
- Revnivykh, Sergey (2012). *GLONASS Status and Modernization, International GNSS Committee IGC-7 Beijing*, (cit. on p. 10).

- Saastamoinen, J (1973). ‘Contributions to the theory of atmospheric refraction’. In: *Bulletin Géodésique (1946-1975)* 107.1, pp. 13–34 (cit. on p. 29).
- Schaer, Stefan, Werner Gurtner, and Joachim Feltens (1998). ‘IONEX: The ionosphere map exchange format version 1’. In: *Proceedings of the IGS AC workshop, Darmstadt, Germany*. Vol. 9. 11 (cit. on pp. 54, 57).
- Seeber, Günter (2003). *Satellite Geodesy : Foundations, Methods, and Applications*. 2nd ed. de Gruyter. isbn: 3-11-017549-5 (cit. on pp. 21, 22, 27).
- Subirana, J.Sanz, J.M. Juan Zornoza, and M. Hernández-Pajares (2013). *GNSS Data Processing - Volume I: Fundamentals and Algorithms*. European Space Agency (cit. on pp. 41, 42, 44).
- Takasu, Tomoji (2013). *RTKLIB ver. 2.4.2 Manual*. http://www.rtklib.com/prog/manual_2.4.2.pdf. [Online; accessed 14-January-2017] (cit. on p. 77).
- Tippenhauer, Nils Ole et al. (2011). ‘On the requirements for successful GPS spoofing attacks’. In: *Proceedings of the 18th ACM conference on Computer and communications security*. ACM, pp. 75–86 (cit. on p. 97).
- Wübbena, G (1985). ‘Software developments for geodetic positioning with GPS using TI-4100 code and carrier measurements’. In: *Proceedings of the first international symposium on precise positioning with the global positioning system*. Vol. 19. sl]:[sn] (cit. on p. 97).